




EX LIBRIS
UNIVERSITATIS
ALBERTENSIS

The Bruce Peel
Special Collections
Library



Digitized by the Internet Archive
in 2025 with funding from
University of Alberta Library

<https://archive.org/details/0162015387135>

University of Alberta

Library Release Form

Name of Author: Jiang Chen

Title of Thesis: Microstructural Studies of Ti/Al/Ti/Au Metallization to n-AlGaIn/GaN Heterostructures

Degree: Master of Science

Year this Degree Granted: 2002

Permission is hereby granted to the University of Alberta Library to reproduce single copies of this thesis and to lend or sell such copies for private, scholarly or scientific research purposes only.

The author reserves all other publication and other rights in association with the copyright in the thesis, and except as herein before provided, neither the thesis nor any substantial portion thereof may be printed or otherwise reproduced in any material form whatever without the author's prior written permission.

University of Alberta

**Microstructural Studies of Ti/Al/Ti/Au Metallization to n-AlGaIn/GaN
Heterostructures**

by



Jiang Chen

A thesis submitted to the Faculty of Graduate Studies and Research in partial fulfillment
of the requirements for the degree of Master of Science

in

Materials Engineering

Department of Chemical and Materials Engineering

Edmonton, Alberta

Spring, 2002

University of Alberta

Faculty of Graduate Studies and Research

The undersigned certify that they have read, and recommend to the Faculty of Graduate Studies and Research for acceptance, a thesis entitled **Microstructural Studies of Ti/Al/Ti/Au Metallization to n-AlGaIn/GaN Heterostructures** submitted by **Jiang Chen** in partial fulfillment of the requirements for the degree of **Master of Science in Materials Engineering**.

ABSTRACT

To develop high quality AlGa_N/Ga_N heterostructure field effect transistors (HFETs) for use in high power, high frequency, and high temperature applications, low resistance, thermal stable ohmic contacts with good surface morphology are essential. Low contact resistances have been achieved using an Au/Ti/Al/Ti contact - a minimum value of $6.33 \times 10^{-6} \text{ } \Omega \text{cm}^2$ was attained after annealing at 700°C for 30s. Microstructural analysis using transmission electron microscopy (TEM) indicated that there is significant interaction between the metallization components and the semiconductor during annealing. The optimum electrical properties correspond to a microstructure consisting of Au₂Ti and TiAl layers as well as a thin Ti-rich layer (~10 nm thick) at the metallization/AlGa_N interface. Degradation of the contact occurred for annealing temperatures in excess of 750°C, and was accompanied by decomposition of the AlGa_N layer, as well as Au₂Ti and TiAl layers, and the formation of an Au-Ti-Al-Ga quaternary phase.

ACKNOWLEDGMENTS

Firstly, I would like to thank Dr. Douglas G. Ivey for his superior supervision and guidance during the past two and half years of my Master's degree.

I also wish to thank Dr. Al Meldrum, Mr. Greg Popowich, and Dr. Ming Chen for helping me in TEM operation.

I am grateful to the Natural Sciences and Engineering Research Council (NSERC) of Canada and the National Research Council (NRC) of Canada for providing funding for this project. I would like to thank Dr. Jennifer Bardwell, Dr. Haipeng Tang, Dr. Ying Liu, and Dr. Jim Webb of NRC for providing the GaN samples and electrical measurement.

Finally, I must thank my wife, Nonie, and my parents; without them, this work is impossible.

TABLE OF CONTENTS

1. Introduction	1
2. GaN-based Semiconductors	3
2.1 Energy band structures	4
2.2 Properties of GaN-based semiconductors	7
2.3 Applications of GaN-based semiconductors	9
3. Metal-semiconductor Contacts	11
3.1 The formation of a Schottky barrier	11
3.2 Current-transport mechanism in metal-semiconductor junctions	17
3.2.1 The regime dominated by thermionic emission	18
3.2.2 Thermionic field-emission regime	19
3.3 Resistance of an ohmic contact	20
3.4 Principles for forming ohmic contacts	21
3.5 Determination of the specific contact resistance	22
3.5.1 Transmission line model (TLM)	22
3.5.2 Cox-Strack method	24
3.5.3 Four-point method	25
3.5.4 Shockley technique	26

4. Metal-semiconductor Contacts to GaN-based Semiconductors.....	28
4.1 Ohmic contacts to n-GaN.....	29
4.1.2 Factors influencing the specific contact resistance of metal contacts.....	30
4.1.2.1 Contact metal.....	30
4.1.2.2 Doping concentration of semiconductor.....	32
4.1.2.3 Pre-metallization surface treatments.....	33
4.1.2.4 Annealing.....	34
4.1.2.5 Reactions.....	35
4.1.3 Published data on ohmic contacts to n-GaN.....	35
4.1.3.1 Al, Au/n-GaN.....	35
4.1.3.2 Al/Ti/n-GaN.....	36
4.1.3.3 Au/Ni/Al/Ti/n-GaN.....	36
4.1.3.4 Au/Ti/n-GaN.....	37
4.1.3.5 Al/Ti/n-GaN.....	37
4.1.3.6 Ag/Ti/n-GaN.....	38
4.1.3.7 Al/Ta/n-GaN.....	38
4.1.3.8 Al/Pd/n-GaN.....	39
4.1.3.9 PtIn ₂ /n-GaN.....	39
4.1.3.10 W/n-GaN.....	40
4.1.3.11 TiN/n-GaN or TiN/Ti/n-GaN.....	40
4.1.3.12 Au/Ti/Al/Ti/n-GaN.....	41
4.1.3.13 Au/Pt/Al/Ti/n-GaN.....	41

4.1.3.14 Al/Nd/n-GaN.....	42
4.1.4 Microstructure.....	42
4.2 Ohmic contacts to n-AlGaN.....	44
4.2.1 Phase equilibria.....	46
4.2.2 Published data on ohmic contacts to n-AlGaN.....	47
4.2.2.1 Al/Ti/n-AlGaN/GaN.....	48
4.2.2.2 Au/Ti/Al/Ti/n-AlGaN/GaN.....	49
4.2.2.3 Au/Ti/Al/Pd/n-AlGaN/GaN.....	49
4.2.2.4 Au/Ni/Al/Ti/n-AlGaN/GaN.....	49
4.2.2.5 Ta-based ohmic contact to n-AlGaN/GaN.....	50
4.2.2.6 NiAl/n-AlGaN/GaN.....	50
4.2.3 Microstructural analysis.....	51
5. Experimental Methods.....	53
5.1 Experimental materials.....	53
5.2 Microstructural characterization.....	54
5.2.1 TEM sample preparation.....	55
5.2.1.1 Plan view sample preparation.....	55
5.2.1.2 Cross section sample preparation.....	56
5.2.2 Phase identification.....	62
5.2.2.1 Selected area diffraction (SAD).....	62
5.2.2.2 Convergent beam electron diffraction (CBED).....	63

5.2.2.3 Energy dispersive x-ray spectroscopy (EDX).....	64
6. Results and Discussion.....	65
6.1 Electrical properties.....	65
6.2 Microstructural characterization.....	65
6.2.1 As-deposited.....	66
6.2.2 400°C annealing.....	67
6.2.3 500°C annealing.....	69
6.2.4 600°C annealing.....	72
6.2.5 700°C annealing.....	79
6.2.6 900°C annealing.....	89
7. Conclusions and Recommendations for Future Work.....	92
7.1 Conclusions.....	92
7.2 Recommendations for future work.....	94
8. Reference.....	95

LIST OF TABLES

Table 2.1	Band gap energies, electron and hole mobilities, and intrinsic electrical conductivities at room temperature (300 K) for selected semiconductor materials.....	4
Table 2.2	Properties of the Group-III nitrides (300 K).....	8
Table 4.1	The specific contact resistances for different published metallization schemes to n-GaN.....	29
Table 4.2	Contact characteristics of 17 metals to n-GaN along with their corresponding metal work functions.....	31
Table 4.3	The specific contact resistances for different published metallization schemes to n-AlGaN/GaN.....	45
Table 6.1	Electrical properties of samples annealed at 700°C for 30s.....	65
Table 6.2	Lattice parameters for Ti, Al, Au, and GaN.....	67
Table 6.3	Indexing of SAD pattern from Al-Ti layer in Fig. 6.7(b).....	71
Table 6.4	Results of semi-quantitative EDX analysis for the Au-Ti-Al layer in samples annealed at 600°C for 30s.....	73
Table 6.5	Au compositions of binary Ti-Au phases.....	74
Table 6.6	Au compositions of binary Al-Au phases.....	75
Table 6.7	Crystal structures of Au ₂ Ti and γ -Au ₂ Al binary phases.....	76
Table 6.8	Results of semi-quantitative EDX analysis for the Al-Ti layer in samples annealed at 600°C for 30s.....	76
Table 6.9	Al compositions of binary Al-Ti phases.....	77
Table 6.10	Indexing of SAD pattern from Al-Ti layer in Fig. 6.9(b).....	77
Table 6.11	Results of semi-quantitative EDX analysis for the Au-Ti phase in the plan view specimen (Fig. 6.19).....	80
Table 6.12	Indexing of SAD pattern obtained from the plan view specimen.....	81
Table 6.13	Results of semi-quantitative EDX analysis for the Al-Ti layer in samples annealed at 700°C for 30s.....	83
Table 6.14	Results of mass balance calculation.....	85

Table 6.15 Lattice parameters for possible interfacial phases.....88

LIST OF FIGURES

Figure 2.1 The various possible electron band structures in solids at 0 K. (a) The electron band structure found in metals such as copper, in which there are available electron states above and adjacent to filled states, in the same band. (b) The electron band structure of metals such as magnesium, wherein there is an overlap of filled and empty outer bands. (c) The electron band structure characteristic of insulators; the filled valence band is separated from the empty conduction band by a relatively large band gap (>2 eV). (d) The electron band structure found in the semiconductors, which is the same as for insulators except that the band gap is relatively narrow ($< 2\text{eV}$).^[14]5

Figure 2.2 E - k diagram for a direct-gap semiconductor showing three hole masses: heavy holes, light holes, and split-off holes.^[15]5

Figure 2.3 E - k diagram for an indirect-gap semiconductor showing that the minimum in the conduction band occurs at k values away from $k = 0$.^[15]6

Figure 2.4 Calculated band structure of wurtzite GaN.^[24]8

Figure 3.1 (a) Schematic illustration of the density of states for silicon. (b) Band structure plot as a function of distance, showing surface parameters.^[30]12

Figure 3.2 Formation of a barrier between a metal and a semiconductor (a) neutral and isolated, (b) electrically connected, (c) separated by a narrow gap, (d) in perfect contact.^[30] 13

Figure 3.3 Schottky barrier I - V characteristics for a circular metal film deposited on an n-type semiconductor.^[15]14

Figure 3.4 Barriers for semiconductors of different types and work functions. n-type: (a) $\phi_m > \phi_s$ (rectifying); (b) $\phi_m < \phi_s$ (ohmic). p-type: (c) $\phi_m > \phi_s$ (ohmic); (d) $\phi_m < \phi_s$ (rectifying).^[30]15

Figure 3.5 Metal-semiconductor contact with surface states.^[30]16

Figure 3.6 Schematic description of (a) thermionic emission, (b) thermionic field emission, and (c) tunneling mechanism in an n-type semiconductor.^[17]17

Figure 3.7 I - V characteristics of an ohmic contact.....20

Figure 3.8 (a) Schematic of an ohmic contact structure to an n-type semiconductor. (b) Simplified plot of doping concentration of semiconductor in (a). (c) Simplified energy band diagram of metallization/semiconductor interface region. ^[33]	21
Figure 3.9 (a) Sample configuration for TLM characterization. (b) Schematic of current flow through planar contacts. Nearly all of the current flows through one transfer length, L_T , of the contacts' front edges. (c) Plot of the measured resistance against the contact separation. ^[36]	23
Figure 3.10 Measurement of the specific contact resistance using the Cox-Strack method. The circular ohmic contact has a radius r . ^[34]	24
Figure 3.11 Measurement of the specific contact resistance by four-point probe method. ^[34]	25
Figure 3.12 Measurement of the specific contact resistance by the Shockley technique. The voltage applied to the coplanar ohmic contact is V_a . The linear voltage distribution between the contacts is extrapolated to obtain the transfer length L_T . ^[34]	26
Figure 4.1 Dependence of $S = d\phi_b/d\phi_m$ (change in barrier height over the change in metal work function) on the electronegativity difference between the components of the compound. ^[52]	30
Figure 4.2 Bright field TEM micrographs of Ti/Al (a), (b) and Ti/Al/Ni/Au (c), (d) contacts in cross section before (a), (c) and after (b), (d) annealing. ^[55]	42
Figure 4.3 Hypothetical ternary phase diagrams illustrating key tie-line configuration of three different classes. (a) Stable metal nitride class. (b) Stable metal class. (c) Stable metal aluminide class. ^[53]	46
Figure 4.4 Predicted classes at $T = 873$ K and $p_{N_2} = 1$ atm in (a) Transition metal-Al-N and (b) Transition metal-Ga-N systems. Please note the type of triangle used for e.g., Pd indicates a system belonging to the stable metal aluminide class in (a), whereas it denotes a system in the metal gallide class in (b). ^[53]	46
Figure 5.1 Schematic structure of the metallized AlGaIn/GaN HFET.....	53
Figure 5.2 Schematic of dimpling/ion milling preparation of TEM cross-section samples. (a) A 1 mm×5 mm slice was cut from wafer. (b) Sample was sandwiched with Si	

spacers. (c) A 3-mm disc was cut from sandwiched structure. (d) The final look of a sample.....	57
Figure 5.3 Schematic illustration of the specimen-mounting configuration of Tripod Polisher®	58
Figure 5.4 Schematic illustration of the specimen-mounting configuration during first side polishing. A capping layer is used to protect the specimen from the risk of delamination.....	59
Figure 5.5 Schematic showing the use of a scrap material with hardness close to that of the specimen, to alleviate the tendency for specimen cracking and chipping.....	59
Figure 5.6 Three orientations of specimen mounting during second side wedge polishing are shown. (a) Parallel mounting; (b) Perpendicular mounting; (c) Angular mounting.....	60
Figure 5.7 Schematic illustration of FIB technique.....	61
Figure 5.8 Ring diffraction patterns of aluminum diffraction standard sample. (a) Camera length $L=100$ cm. (b) Camera length $L=80$ cm.....	63
Figure 6.1 TEM bright field images of the as deposited metallization/semiconductor structure at low (a) and high (b) magnification.....	66
Figure 6.2 TEM bright field images of a sample annealed at 400°C for 30s at low (a) and high (b) magnification.....	67
Figure 6.3 SAD spot diffraction pattern (a) obtained from the third (Ti) layer from the semiconductor surface in Fig. 6.2(b), and computer-simulated spot pattern (b)...	68
Figure 6.4 SAD spot diffraction pattern (a) obtained from the fourth (Au) layer from the semiconductor layer in Fig. 6.2(b), and computer-simulated spot pattern (b)....	68
Figure 6.5 SAD spot diffraction pattern (a) obtained from GaN layer in Fig. 6.2(b), and computer-simulated spot pattern (b).....	69
Figure 6.6 TEM bright field image of metallization annealed at 500°C for 30s.....	69
Figure 6.7 EDX spectrum obtained from the outermost dark layer (a) and the bright layer below the Au layer (b) in Fig. 6.6.....	70
Figure 6.8 EDX spectrum (a) and SAD ring diffraction pattern (b) obtained from the Al-Ti layer in Fig. 6.6.....	71

Figure 6.9 TEM bright field images at low (a) and high (b) magnification of sample annealed at 600°C for 30s.....	72
Figure 6.10 EDX spectrum (a) and SAD ring diffraction pattern (b) obtained from the Au-Al-Ti layer in Fig. 6.9.....	72
Figure 6.11 Au-Ti binary phase diagram. ^[65] It shows that Au can form 6 binary phases with Ti; Ti ₃ Au, γTiAu, βTiAu, αTiAu, TiAu ₂ , and TiAu ₄	73
Figure 6.12 SAD pattern (a) from Au-rich layer in Fig. 6.9 and computer-simulated diffraction pattern of Au ₂ Ti at $[0\bar{3}1]$ zone axis.....	74
Figure 6.13 Au-Al binary phase diagram. ^[65] It shows that Au can form 7 binary phases with Al, Al ₂ Au, AlAu, γAlAu ₂ , βAlAu ₂ , αAlAu ₂ , Al ₃ Au ₈ and AlAu ₄	75
Figure 6.14 EDX spectrum (a) and SAD ring diffraction pattern (b) obtained from the Al-Ti layer in Fig. 6.9.....	76
Figure 6.15 Al-Ti binary phase diagram. ^[65]	77
Figure 6.16 SAD pattern (a) from the Al-Ti layer in Fig. 6.9 and computer-simulated diffraction pattern of Al at $[12\bar{3}]$ zone axis.....	78
Figure 6.17 EDX spectrum obtained from the contact/AlGaN interface in Fig. 6.9.....	78
Figure 6.18 TEM bright field images at low (a) and high (b) magnification of sample annealed at 700°C for 30s.....	79
Figure 6.19 (a) TEM plan view image of outer Au-rich layer in Fig. 6.18, and (b) EDX spectrum obtained from (a).....	80
Figure 6.20 SAD ring pattern obtained from several grains in plan view specimen in Fig. 6.19(a). Indexing shows that the rings match Au ₂ Ti and TiAl phases.....	80
Figure 6.21 CBED pattern (a) from one grain in plan view specimen Fig. 6.19(a) and computer-simulated diffraction pattern of Au ₂ Ti at $[\bar{3}\bar{3}1]$ zone axis.....	81
Figure 6.22 TEM bright field image (a) of a sample annealed at 700°C for 30s, which was prepared by wedge polishing method. (b) is the EDX spectrum obtained from the first layer in the image.....	82
Figure 6.23 CBED pattern (a) from one grain in the Ti-Al rich layer in Fig. 6.22(a) and computer-simulated diffraction pattern of TiAl at $[\bar{1}01]$ zone axis.....	83

Figure 6.24 Al-Au-Ti ternary phase diagram at 500°C, it shows a solubility limit for Au in TiAl to be <2 at. %^[66].....84

Figure 6.25 EDX spectrum obtained from the contact/AlGaIn interface in Fig. 6.22(a)..86

Figure 6.26 EDX spectra obtained from the AlGaIn layer (a) and GaIn layer (b) in Fig. 6.22(a)87

Figure 6.27 TEM bright field image of a sample annealed at 900°C for 30s.....89

Figure 6.28 EDX spectrum (a) and CBED pattern (b) obtained from the middle layer in Fig. 6.26.....90

Figure 6.29 EDX spectra obtained from the outermost (a) and innermost layers.....91

1. INTRODUCTION

GaN-based semiconductors have attracted increasing interest from both electrical and materials engineers/scientists since the mid-1990's. Because of their high electron mobilities, good thermal conductivities, high thermal stabilities, and large breakdown electric fields, GaN-based semiconductors are excellent candidates for electronic devices operating at high power and in high temperature environments. When alloyed with other group III elements, GaN forms a series of compounds with a direct band gap from 1.89 eV (InN)^[1] to 6.2 eV (AlN).^[2] This also makes GaN-based semiconductors excellent candidates for photonic devices operating in the spectral region from the ultraviolet to green. Several GaN-based semiconductor devices, including metal-semiconductor field-effect transistors (MESFET), high electron mobility transistors (HEMT), blue laser diodes, UV photoconductive detectors, UV photovoltaic detectors, and visible light-emitting diodes (LED), have been reported.^[3-7]

AlGaN/GaN heterostructure field effect transistors (HFET) are important devices for high power, high frequency, and high temperature applications. The quality of ohmic contacts is one of the crucial factors that limit the performance of these devices. In order to connect the active regions of semiconductor devices to the external circuit, very low resistance (reducing knee voltage and resistive heating), thermally stable (ensuring dependable high temperature performance) ohmic contacts with good surface morphology (providing good edge acuity for short-channel devices) are required.

Among several different metallization schemes^[8-13] for ohmic contacts to AlGaN/GaN HFETs, Al/Ti-based ohmic contacts, with metal layers of varying thickness and number, have become the standard contacts for n-AlGaN/GaN. Recent results have shown that the Ti/Al ratio, annealing temperature and time, surface treatments prior to metallization, and the thickness of metal layers can affect the resistance and surface morphology of contact. However, the mechanism of ohmic contact formation is still not thoroughly understood. Two possible models, i.e., a low Schottky barrier and a tunneling contact, have been proposed to explain the ohmic behavior. It is believed that the tunneling contact involves

out-diffusion of nitrogen toward the metal layers and the formation of a heavily doped semiconductor layer (by N vacancies) under the contact, providing the configuration for tunneling. Additional layers (e.g., Ni, Pt, and Au) have also been included with Ti and Al in an effort to reduce the contact resistance. But the role of any additional metal layer is still under discussion.

Very little microstructural characterization work^[8, 11] to analyze phase changes of contacts to HFET structures, which occur during annealing, has been done. This may be due in part to the difficulties of sample preparation for AlGaIn/GaN heterostructures and to the difficulties of phase identification in such fine scale microstructures.

This thesis focuses on microstructural studies of Ti/Al/Ti/Au ohmic contact to an n-AlGaIn/GaN heterostructure. The purpose of detailed microstructural studies is to correlate changes in electrical properties of the contact with phase changes that occur during annealing. With improved understanding of ohmic contact formation, optimized metallizations should be developed in the future.

The thesis is organized into seven chapters. A comprehensive literature survey is provided in Chapters 2 and 3, which describes the properties and applications of GaN-based semiconductors, and the ohmic contact formation principles. Chapter 4 is an extensive literature survey covering published experimental results on metal-semiconductor contact structures and electrical properties, with emphasis on the metal/GaN-based contact systems. Chapter 5 outlines the experimental methods utilized for fabricating the Au/Ti/Al/Ti/n-AlGaIn/GaN contact system, and the techniques employed for analyzing the microstructures of contacts. Chapter 6 contains the results and discussion of the thesis work, which includes the determination of electrical properties and microstructures of contacts annealed at different temperature, and the relationship between them. Chapter 7 is a summary of the thesis work.

2. GaN-BASED SEMICONDUCTORS

Semiconductors have electrical properties that are intermediate between the electrical conductors and insulators. Semiconductors are nonmetallic materials that have a filled valence band at 0 K and a relatively narrow energy gap. The room temperature electrical conductivity ranges between about 10^{-6} to 10^4 $(\Omega\text{-m})^{-1}$.^[14] Conductivities of semiconductors are strongly dependent on temperature. Furthermore, the electrical characteristics of these materials are extremely sensitive to the presence of minute concentrations of impurity atoms, whose concentrations may be controlled over very small spatial regions. Intrinsic semiconductors are those in which the electrical behavior is based on the electronic structure inherent to the pure material. When the electrical characteristics are dictated by impurity atoms, the semiconductor is said to be extrinsic. Classified by chemical composition, semiconductors are divided into two groups – elemental and compound semiconductors. The two major elemental semiconductors are silicon (Si) and germanium (Ge), having band gap energies of approximately 1.1 and 0.7 eV, respectively. Both are found in Group IVA of the Periodic Table and are covalently bonded. They are sometimes called diamond-type semiconductors due to their crystal structure of diamond. III-V compound semiconductors are formed between elements of Groups IIIA and VA, for example, gallium arsenide (GaAs) and indium phosphide (InP). The compounds composed of elements of Groups IIB and VIA also display semiconducting behavior, e.g., cadmium sulfide (CdS) and zinc telluride (ZnTe); these are frequently called II-VI compound semiconductors. As the two elements forming these compounds become more widely separated with respect to their relative positions in the Periodic Table (i.e., the electronegativities become more dissimilar), the atomic bonding becomes more ionic and the magnitude of the band gap energy increases – the materials tend to become more insulating. Table 2.1 gives the properties of some typical semiconductors.

Table 2.1 Band gap energies, electron and hole mobilities, and intrinsic electrical conductivities at room temperature (300 K) for selected semiconductor materials^[14]

Material	Band Gap (eV)	Electrical Conductivity ($\Omega \cdot \text{m}$) ⁻¹	Electron Mobility ($\text{cm}^2/\text{V} \cdot \text{s}$)	Hole Mobility ($\text{cm}^2/\text{V} \cdot \text{s}$)
Elemental				
Si	1.11	4×10^{-4}	1400	500
Ge	0.67	2.2	3800	1800
III-V Compounds				
GaP	2.25	—	500	20
GaAs	1.42	10^{-6}	8500	4500
InP	1.34	5×10^{-8}	4600	150
InSb	0.17	2×10^4	77000	700
II-VI Compounds				
CdS	2.40	—	300	—
ZnTe	2.26	—	300	100

2.1 Energy Band Structures

The electrical conductivity of a material is strongly dependent on the number of electrons available to participate in the conduction process. The number of electrons available for electrical conduction in a particular material is related to the arrangement of electron states or levels with respect to energy, and then the manner in which these states are occupied by electrons. In a crystalline solid the electrons are influenced by the periodic potential associated with the arrangement of atoms, and as a result electron energy bands and gaps occur in the allowed energy spectrum of electrons. Four different types of band structures are possible at 0 K corresponding to the classification of conductors, insulators and semiconductors (Fig 2.1).^[14] The difference between insulators and semiconductors lies in the magnitude of the energy gap; the band gap of an insulator is much wider than that of a semiconductor.

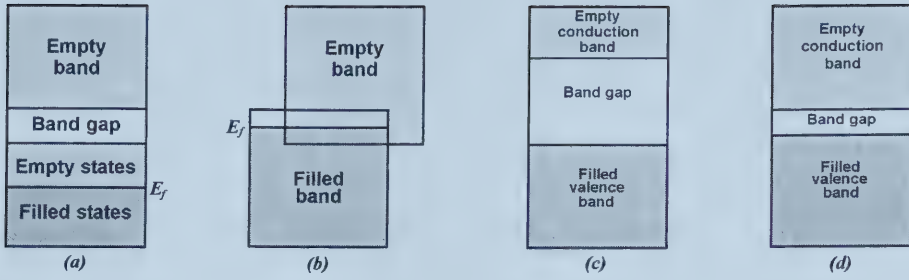


Figure 2.1 The various possible electron band structures in solids at 0 K. (a) The electron band structure found in metals such as copper, in which there are available electron states above and adjacent to filled states, in the same band. (b) The electron band structure of metals such as magnesium, wherein there is an overlap of filled and empty outer bands. (c) The electron band structure characteristic of insulators; the filled valence band is separated from the empty conduction band by a relatively large band gap (>2 eV). (d) The electron band structure found in the semiconductors, which is the same as for insulators except that the band gap is relatively narrow (<2 eV).^[14]

According to the wave behavior of electrons, the energy of a free electron has the following relationship to the momentum \mathbf{p} ,

$$E = \frac{\hbar^2 k^2}{2m^*} \quad (2-1)$$

where the wave vector \mathbf{k} represents momentum space, $\mathbf{p} = \hbar\mathbf{k}$; the effective mass m^* changes the curvature of E - \mathbf{k} diagram. For most semiconductors, the threefold valence

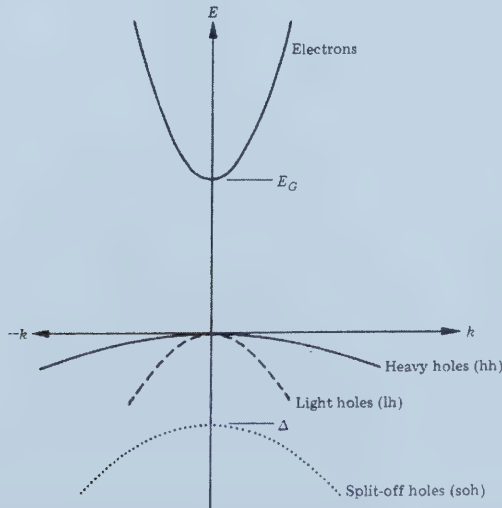


Figure 2.2 E - \mathbf{k} diagram for a direct-gap semiconductor showing three hole masses: heavy holes, light holes, and split-off holes.^[15]

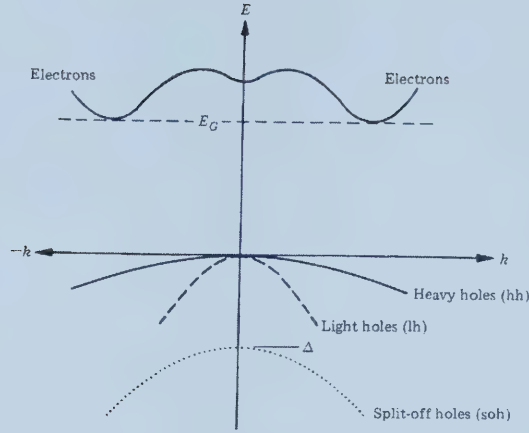


Figure 2.3 E - k diagram for an indirect-gap semiconductor showing that the minimum in the conduction band occurs at k values away from $k = 0$.^[15]

band structures are the same, consisting of heavy hole (hh) and light hole (lh) bands due to their heavy and light effective masses respectively. There is a lower band displaced in energy (split off in energy from the hh and lh bands) due to spin-orbit interactions. This is denoted the split-off hole (soh) band (see Fig. 2.2).^[15] The maxima in the valence band are located at $k = 0$. However, there are different possible situations in conduction bands. GaAs, InP, GaN, as well as other III-V compounds are referred to as direct-gap semiconductors, because the minimum in the conduction band and the maximum in the valence band are located at $k = 0$. When holes and electrons are present, the electrons can make a direct transition to a hole state without a change in momentum. In some direct-gap semiconductors, there are other minima located away from $k = 0$, e.g., GaAs has another minimum along the $\langle 111 \rangle$ direction. But if the conduction band minimum at $k = 0$ is lowest in energy, these band structures still belong to the direct gap designation. In Si as well as Ge and some of the III-V semiconductors, such as GaP and AlSb, the minimum in the conduction band is located away from $k = 0$, as shown in Fig. 2.3.^[15] The electrons at the conduction band minimum are displaced in k space from the holes at the maximum in the valence band. Electrons cannot make a direct transition to the valence band without interacting with lattice atoms in order to conserve momentum.

The band structure is very important in optical transitions within semiconductors. The mobility (μ) and effective mass (m^*) of electrons in a semiconductor strongly depend on

the band gap structure. In a direct-gap semiconductor, an electron in the conduction band can fall directly to an empty state in the valence band, emitting a photon of light with energy E_g (energy gap). The situation is not as simple for indirect-gap semiconductors. An electron in the conduction band minimum cannot make a direct transition to the valence band maximum. Both energy and momentum must be changed in the transition involving the emission of a photon. As a result, a change in k will give up a large amount of energy as heat to the lattice (phonon) rather than as an emitted photon. The effectiveness of light emission is reduced considerably. The mobility of electrons (μ) is higher and the effective mass of electrons (m^*) is lower in direct-gap semiconductors than those in indirect-gap semiconductors.

2.2 Properties of GaN-based semiconductors

GaN-based semiconductors have excellent material, optical and electrical properties. There are three common crystal structures shared by the group-III nitrides: the wurtzite (hexagonal), zincblende (cubic), and rocksalt (cubic) structures. Under ambient conditions, the thermodynamically stable structure is wurtzite for bulk AlN, GaN, and InN. Table 2.2 lists major properties of the group-III nitrides with the wurtzite structure, and Figure 2.4 shows the band structure of GaN.^[24]

Although GaN has been studied far more extensively than other group-III nitrides, there is still the need for further investigations to even approach the level of understanding of technologically important materials such as Si and GaAs. GaN is a III-V compound semiconductor with a wurtzite crystal structure having a 3.4 eV direct energy band gap at room temperature. Both the valence band maximum and the lowest conduction band minimum occur at the center of the Brillouin zone (Γ point). When alloyed with the other group-III elements, GaN forms a series of compounds with direct band gap energies ranging from 1.89 eV (InN) to 6.2 eV (AlN).

Table 2.2 Properties of the Group-III nitrides (300 K)

Properties		GaN	AlN	InN
Crystal structure		Wurtzite	Wurtzite	Wurtzite
Density (g/cm ³)		6.15 ^[16]	3.23 ^[16]	6.81 ^[16]
Dielectric Constant		10.4 ^[17]	8.5±0.2 ^[17]	15.3 ^[17]
Energy gap (eV, Γ valley)		3.39 ^[18]	6.2 ^[2]	1.89 ^[1]
Effective mass	m_e	0.22 m_0 ^[19]	0.48 m_0 ^[16]	0.11 m_0 ^[19]
	m_p	>0.8 m_0 ^[17]	—	—
Lattice constant	a (nm)	0.3189 ^[20]	0.3110 ^[20]	0.3540 ^[20]
	c (nm)	0.5189 ^[20]	0.4980 ^[20]	0.5700 ^[20]
Intrinsic mobility	μ_n (cm ² /V·s)	1000 ^[21]	135 ^[22]	3200 ^[23]
	μ_p (cm ² /V·s)	30 ^[20]	14 ^[20]	—
Saturation velocity (cm/s)		2.5×10 ⁷ ^[21]	1.4×10 ⁷ ^[22]	2.5×10 ⁷ ^[23]
Breakdown field (V/cm)		5×10 ⁶ ^[20]	—	—
Thermal conductivity (W/cm·K)		1.5 ^[20]	2.0 ^[20]	—
Melting temperature (°C)		>1700 ^[20]	3000 ^[20]	1100 ^[20]

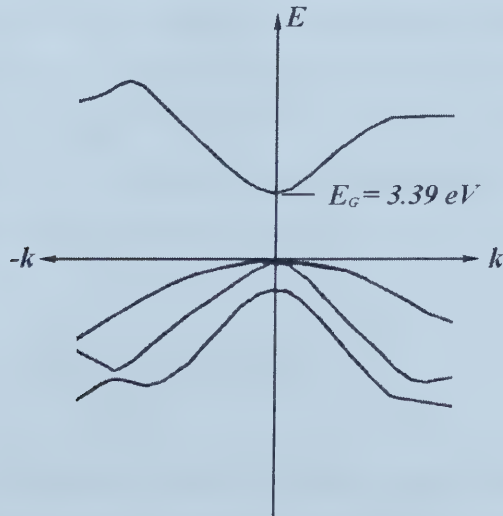


Figure 2.4 Calculated band structure of wurtzite GaN.^[24]

One of the major difficulties which has hindered GaN research is the lack of a suitable substrate material that is lattice matched and thermally compatible with GaN. GaN, AlN and InN have been grown primarily on sapphire, most commonly the (0001) orientation (C-plane), but also the $(21\bar{3}1)$, $(11\bar{2}0)$ orientations. In addition, III-V nitrides have been grown on Si, NaCl, GaP, InP, SiC, W, ZnO, MgAl₂O₄, TiO₂, and MgO.

Many important GaN-based devices involve heterostructures as the primary means of achieving improved performance. Many of the properties of alloyed semiconductors such as the energy band gap, effective masses of the electrons and holes, and the dielectric constant are dependent on the alloy composition.

The energy band gap of Al_xGa_{1-x}N may be expressed by,

$$E_g(x) = xE_g(\text{AlN}) + (1-x)E_g(\text{GaN}) - bx(1-x)^{[17]} \quad (2-2)$$

where $E_g(\text{GaN}) = 3.4$ eV, $E_g(\text{AlN}) = 6.20$ eV, x is the AlN molar fraction, and b is the bowing parameter, which accounts for the nonlinear dependence of the fundamental band gap on the alloy composition.

Until recently the resistivity of unintentionally doped AlGa_xN was believed to increase so rapidly with increasing AlN mole fraction that AlGa_xN became almost insulating for AlN mole fractions exceeding 20%. As the AlN mole fraction increased from 0 to 30%, the n-type carrier concentration dropped from 10^{20} to 10^{17} cm⁻³, and the mobility increased from 10 to 30 cm²/V.s. An increase in the native-defect ionization energies with increasing AlN may possibly be responsible for this variation.

2.3 Applications of GaN-based semiconductors

The band structure of a given semiconductor is pivotal in determining its potential utility. When alloyed with other group-III elements, wurtzite GaN forms a continuous alloy system whose direct band gaps range from 1.89 eV for InN, to 3.4 eV for GaN, and to 6.2 eV for AlN. For all practical purposes, the III-V nitrides could potentially be fabricated

into optical devices which are active at wavelengths ranging from green to ultraviolet. By using nitride emitters as pumps, all primary and mixed colors can be obtained. Nitride-based green and blue light emitting diodes (LED) with efficiency, brightness, and longevity that are well in excess of those required for outdoor applications are already commercially available. Other applications of blue LEDs are under development. Potentially, further improvement in LEDs would expand the applications to lighting with large energy savings as LEDs are more efficient than incandescent bulbs. Injection laser diodes (LD) operating at short wavelengths have been coveted for years for digital data reading and storage applications. Semiconductor nitrides have the band gaps required to reach these short wavelengths. The storage density of the digital versatile disk (DVD) is predicted to go up from today's 1 Gb to about 40 Gb per compact disk when blue lasers are used. Semiconductor nitrides are also prime candidates for ultraviolet (UV) photodetectors which have many potential applications in such areas as solar astronomy, missile-plume detection and combustion-process monitoring.

Large carrier velocities, large total carrier concentrations available in two-dimensional systems, large band discontinuities in AlGa_N/Ga_N heterostructure systems, and a tolerance to high junction temperatures form the basis for nitride high-power electronic devices with applications requiring low cost, small space and power efficiency. Using Ga_N-based semiconductors, electronic devices employed at high power and at high temperatures, as well as high frequency environments have been fabricated, such as metal-semiconductor field-effect transistors (MESFET), high electron mobility transistors (HEMT), and heterojunction bipolar transistors (HBT).

At present, interest in the Ga_N system for the fabrication of high power, high frequency electronic devices is focused on AlGa_N/Ga_N heterostructure field effect transistor (HFET) structures, as these show the greatest potential for commercialization in the short term, and some impressive characteristics have already been reported.^[13, 25-29]

3. METAL-SEMICONDUCTOR CONTACTS

To connect the active regions of the semiconductors to external circuits, metal contacts to semiconductors are necessary. It is imperative that a semiconductor device be connected to the outside world with no adverse change to its current-voltage characteristics and no additional voltage drop. This can be accomplished only through low-resistance ohmic contacts on the semiconductor. An ideal contact is one where, when combined with the semiconductor, there are no barriers to the carrier flow in either the positive or negative directions. Additional requirements for ohmic contacts are that contacts must be stable both thermally and chemically. The need for stability cannot be overstated in devices intended for high-power and high-temperature operation, either by design or necessity, when the junction temperatures could be high. Finally flat surface morphology is also required to ensure good edge acuity for short-channel devices.

According to their current-voltage (I-V) characteristics, metal-semiconductor contacts can be divided into two classifications. Contacts with rectifying characteristics are called Schottky barriers or rectifying contacts, and contacts with linear characteristics are called ohmic contacts or nonrectifying contacts.

3.1 The formation of a Schottky barrier

The work function ϕ_m of a metal is the amount of energy required to raise an electron from the Fermi level to a state of rest outside the surface of the metal (the so-called vacuum level). The work function ϕ_s of a semiconductor is the difference in energy between the Fermi level and the vacuum level and is composed of bulk and surface contributions. If the bands are flat (i.e., there is no electric field inside the semiconductor), the work function can be represented in the following equation

$$\phi_s = \chi_s + \xi \quad (3-1)$$

where χ_s is the electron affinity, which is the difference in energy between an electron at rest outside the surface and an electron at the bottom of the conduction band just inside

the surface; ξ is the energy difference between the Fermi level and the bottom of the conduction band. The ionization energy I is defined by the relationship

$$I = \chi_s + E_g \quad (3-2)$$

where E_g is the energy gap of semiconductor. The ionization energy is the minimum energy needed to remove an electron from the valence band. Fig. 3.1^[30] schematically shows the band structure of silicon.

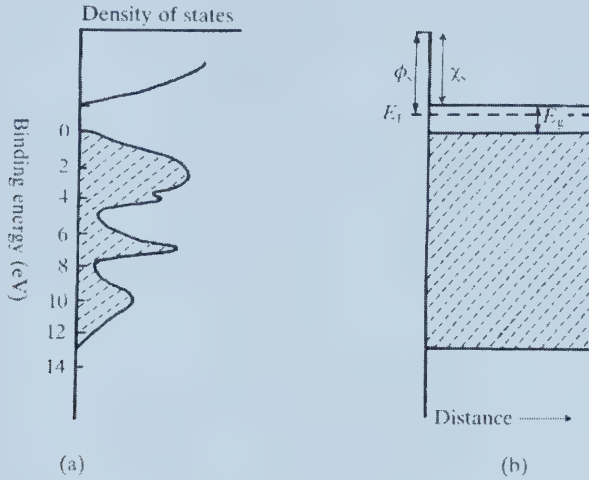


Figure 3.1 (a) Schematic illustration of the density of states for silicon. (b) Band structure plot as a function of distance, showing surface parameters.^[30]

Fig. 3.2^[30] shows how a Schottky barrier forms. A Schottky barrier may form when a metal comes into contact with a semiconductor, assuming that the metal and semiconductor are both electrically neutral and separated from each other. The energy band diagram is shown in Fig. 3.2(a) for an n-type semiconductor with a work function less than that of the metal, and where no surface states are present. If the metal and semiconductor are connected electrically by a wire, electrons pass from the semiconductor into the metal and the two Fermi levels are forced into coincidence as shown in Fig. 3.2(b). The energies of electrons at rest outside the surfaces of the two solids are no longer the same, and there is an electric field in the gap directed from right to left. There must be a negative charge on the surface of the metal balanced by positive charge in the semiconductor. Since the semiconductor is n-type, the positive charge will be provided by conduction electrons receding from the surface, leaving uncompensated

positive donor ions in a region depleted of electrons. Because the donor concentration is many orders of magnitude less than the concentration of electrons in the metal, the uncompensated donors occupy a layer of appreciable thickness w , comparable to the width of depletion region in a p-n junction, and the bands in the semiconductor are bent upwards as shown in Fig. 3.2(b). The difference V_i between the electrostatic potentials outside the surfaces of the metal and semiconductor is given by $V_i = \delta \epsilon_i$, where δ is their separation and ϵ_i the field in the gap. If the metal and semiconductor approach each other, V_i must tend to zero if ϵ_i is to remain finite (Fig. 3.2(c)) and, when they finally touch (Fig.

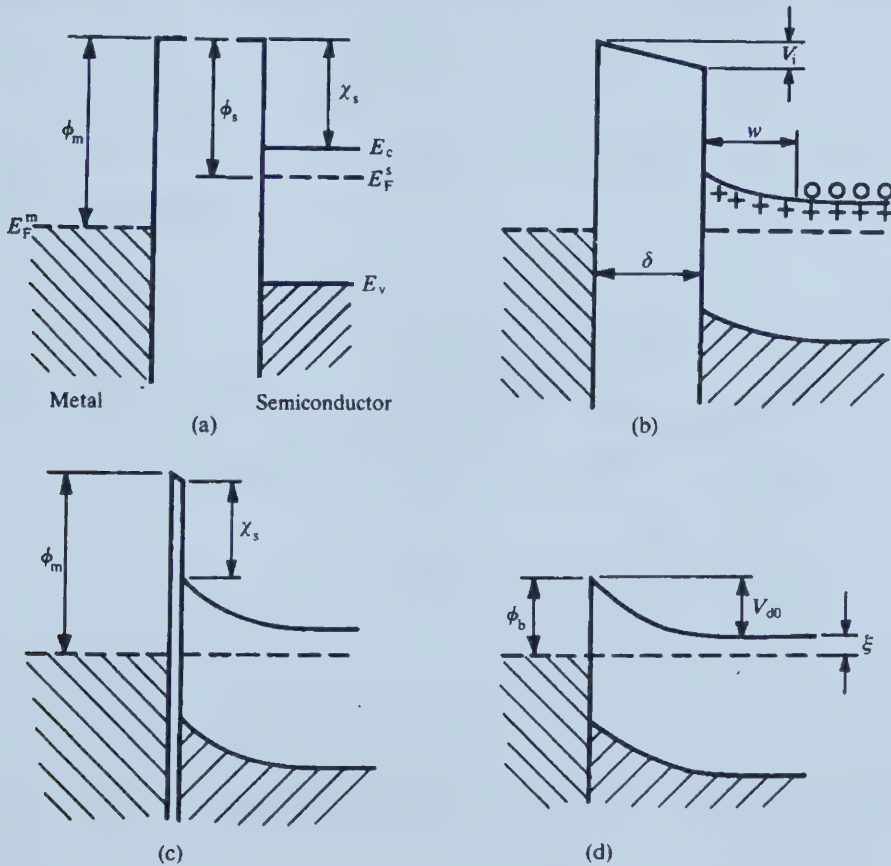


Figure 3.2 Formation of a barrier between a metal and a semiconductor (a) neutral and isolated, (b) electrically connected, (c) separated by a narrow gap, (d) in perfect contact.^[30]

3.2(d)), the barrier due to the vacuum disappears altogether and an ideal metal-semiconductor contact is left. It is clear from the fact that V_i tends to zero that the height of the Schottky barrier ϕ_b measured relative to the Fermi level is given by

$$\phi_b = \phi_m - \chi_s \quad (3-3)$$

The barrier for electrons in the semiconductor relative to the metal is V_{d0} , the diffusion potential or the band bending in the semiconductor at equilibrium,

$$V_{d0} = \phi_m - \phi_s = \phi_b - \xi \quad (3-4)$$

In most practical metal-semiconductor contacts, the ideal situation shown in Fig. 3.2(d) is never reached because there is usually a thin insulating layer of oxide, about 1-2 nm thick, on the surface of the semiconductor. Such an insulating film is often referred to as an interfacial layer. A practical contact is therefore more like that shown in Fig. 3.2(c); however, the barrier presented to electrons by the oxide layer is usually so narrow that electrons can tunnel through it quite easily, and Fig. 3.2(c) is almost indistinguishable from Fig. 3.2(d) as far as the conduction electrons are concerned. Fig. 3.3 shows Schottky barrier I-V characteristics.^[15]

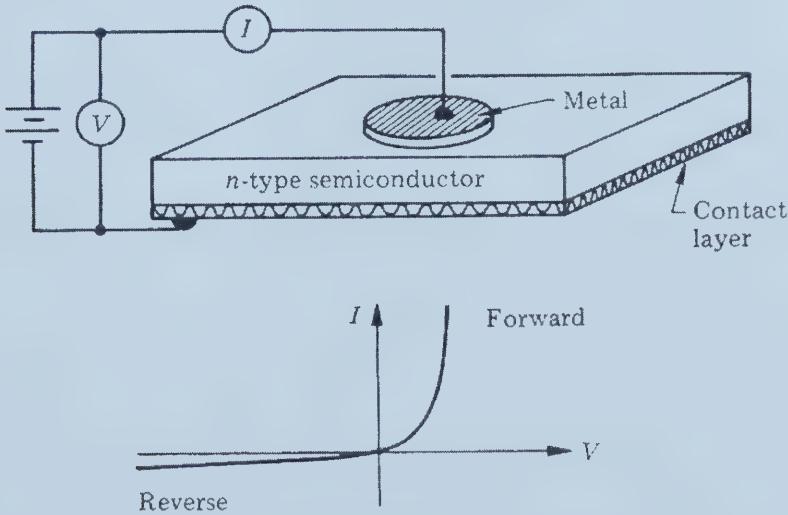


Figure 3.3 Schottky barrier I - V characteristics for a circular metal film deposited on an n-type semiconductor.^[15]

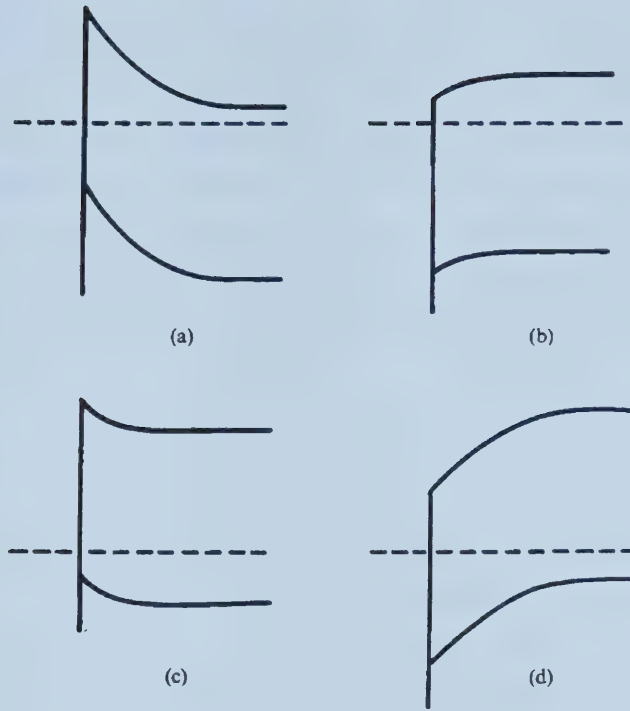


Figure 3.4 Barriers for semiconductors of different types and work functions. n-type: (a) $\phi_m > \phi_s$ (rectifying); (b) $\phi_m < \phi_s$ (ohmic). p-type: (c) $\phi_m > \phi_s$ (ohmic); (d) $\phi_m < \phi_s$ (rectifying).^[30]

The contact discussed above behaves as a rectifier. If a similar contact is developed for the case when $\phi_s > \phi_m$, there will be a band diagram of the form shown in Fig. 3.4(b). Clearly, if such a contact is under forward bias, the electrons encounter no barrier. If it is biased so that electrons flow in the reverse direction, the comparatively high concentration of electrons flows in the region where the semiconductor bands are bent downwards (usually referred to as an accumulation region), and behaves like a cathode which is easily capable of providing a copious supply of electrons. The current is then determined by the bulk resistance of the semiconductor. Such a contact is termed as an ohmic contact. This type of contact has sufficiently low resistance for the current to be determined by the resistance of the bulk semiconductor rather than by the properties of the contact.

In a p-type semiconductor for which ϕ_m exceeds ϕ_s , we obtain the band diagram shown in Fig. 3.4(c), which also represents an ohmic contact. The case of a p-type semiconductor for which ϕ_s exceeds ϕ_m is shown in Fig. 3.4(d). Bearing in mind that holes have difficulty in going underneath a barrier, one sees that Fig. 3.4(d) is the p-type analogue of Fig. 3.4(a) and gives rise to rectification. Fig. 3.4(b) and (c) are very uncommon in practice, and the majority of metal-semiconductor combination form rectifying or 'blocking' contacts (Schottky contacts). For a given semiconductor and for any metal, the sum of the barrier height on n-type and p-type substrates is equal to the energy band gap or:

$$\phi_{bn} + \phi_{bp} = E_g \quad (3-5)$$

In practical metal-semiconductor contacts, the disruption of the crystal lattice at the

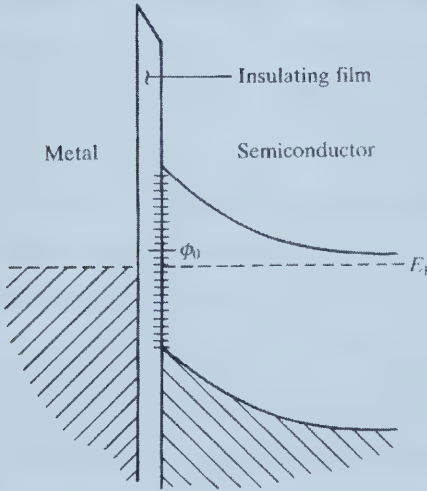


Figure 3.5 Metal-semiconductor contact with surface states.^[30]

interface produces a large number of energy states called interface or surface states, located within the forbidden gap. The interface states are usually continuously distributed in energy and are characterized by a neutral level ϕ_0 (see Fig. (3.5))^[30]. The states below ϕ_0 are positively charged when empty; the states above ϕ_0 are negatively charged when occupied. If ϕ_0 is aligned with the Fermi level, the net charge of the surface is zero.

Whenever $\phi_0 > E_F$, the net charge of the interface states is positive, or donorlike, so that fewer ionized donors are needed in the depletion layer to reach equilibrium. As a result, the diffusion potential V_{d0} is effectively reduced, and according to Eq. (3-4), the Schottky barrier height ϕ_b is also reduced. Similarly, if $\phi_0 < E_F$, there is a negative charge in the interface states and ϕ_b is increased to bring E_F closer to ϕ_0 again. Thus, the change in interface states has a negative feedback effect which tends to keep E_F close to ϕ_0 . If the

density of surface states becomes very large, the deviation of ϕ_0 from E_F will be very small and $\phi_0 \approx E_F$. It is usual to measure ϕ_0 from the top of the valence band, in which case the barrier height will be given by

$$\phi_b = E_g - \phi_0 \quad (3-6)$$

In this case, the Schottky barrier height is almost independent of the choice of metal. The barrier height is said to be ‘pinned’ by the high density of surface states.

3.2 Current-transport mechanisms in metal-semiconductor junctions

In cases when defects are not involved, there are three mechanisms (Fig. 3.6)^[30, 31] that govern the current flow in a metal-semiconductor system.

- (1) Thermionic Emission (TE) – For moderately doped semiconductors, $N_d \leq 10^{17} \text{ cm}^{-3}$, the depletion region is relatively wide. It is nearly impossible to tunnel through the barrier unless aided by defects. If the barrier is small, the electrons (in an n-type semiconductor) can surmount the top of it by thermionic emission (Fig. 3.6(a)). For low-doped or high-barrier semiconductors, on the other hand, the vast majority of electrons would be unable to cross in either direction into the semiconductor; and ohmic behavior is not observed.
- (2) Thermionic-Field Emission (TFE) – For intermediately doped semiconductors, $10^{17} < N_d \leq 10^{18} \text{ cm}^{-3}$, the depletion region is not sufficiently thin to allow direct tunneling of carriers that are more or less in equilibrium. But, if the carriers gain a little energy, they may be able to tunnel. Consequently, both thermionic emission and tunneling take place (Fig. 3.6(b)).

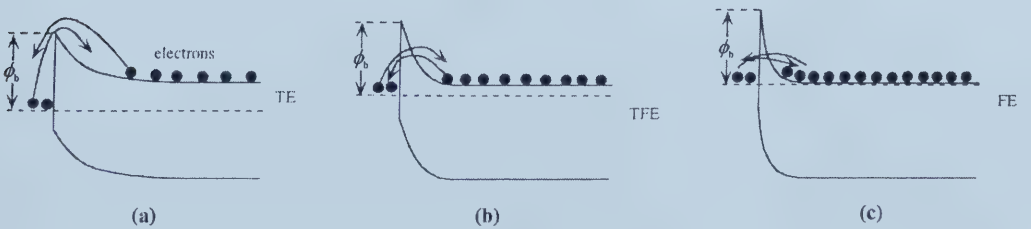


Figure 3.6 Schematic description of (a) thermionic emission, (b) thermionic field emission, and (c) tunneling mechanism in an n-type semiconductor.^[17]

(3) Field Emission (FE) – For heavily doped semiconductors, $N_d \geq 10^{18} \text{ cm}^{-3}$, the depletion region is narrow, and direct electron tunneling from the metal to the semiconductor is allowed (Fig. 3.6(c)). In the absence of a good match between the metal and the semiconductor work functions, which is generally the case, this is the best approach to pursue for ohmic contacts.

3.2.1 The regime dominated by thermionic emission

The traditional current-voltage expression representing thermionic emission is given by

$$J_{TE} = J_{TE0} \left[\exp\left(\frac{qV}{kT}\right) - 1 \right] \quad (3-7)$$

with the saturation value of the current density $J_{TE0} = A^* T^2 \exp\left[\frac{-q(\phi_b - \Delta\phi)}{kT}\right]$. A^* is the effective Richardson constant, ϕ_b is the barrier height, and $\Delta\phi$ is the image-force barrier lowering. The Richardson constant $A^* = \frac{4\pi m^* q k^2}{h^3} = 1.2 \times 10^6 (m^*/m) \text{ A m}^{-2} \text{ K}^{-2}$.

Equation (3-7) is a representation of the carrier flux from the semiconductor to the metal, with the barrier being voltage dependent, and that from the metal to the semiconductor with the barrier fixed at ϕ_b . Since there exists parasitic resistance in the circuit such as semiconductor resistance, the thermionic-emission current expression is modified as

$$J_{TE} = J_{TE0} \left[\exp\left(\frac{q(V - IR_s)}{kT}\right) - 1 \right] \quad (3-8)$$

3.2.2 Thermionic field-emission regime

In thermionic field-emission, the tunneling component of the current including the effect of the series resistance can be written as^[32]

$$J_{TEF} = J_{TEF0} \left[\exp \left(\frac{q(V - IR_s)}{E_0} \right) - 1 \right] \quad (3-9)$$

where the saturation value is given by

$$J_{TEF0} = \frac{A^* T [\pi q E_{00} (\phi_b - V - \eta)]^{1/2}}{k \cosh(E_{00}/kT)} \exp \left[-\frac{q\eta}{kT} - \frac{q(\phi_b - \eta)}{E_0} \right], \text{ with } E_0 = E_{00} \coth \left(\frac{E_{00}}{kT} \right) \text{ and}$$

$$E_{00} = \frac{qh}{2} \sqrt{\frac{N_D}{\epsilon_s m^*}}. E_0 \text{ is a parameter dependent on the barrier transparency, and } \eta \text{ is the}$$

Fermi level with respect to the conduction-band edge in an n-type semiconductor and with respect to the valence-band edge in a p-type semiconductor.

3.2.3 Direct tunneling regime

At low temperatures and high doping concentrations, direct tunneling dominates the current. The current flow in tunneling regime can be approximated by

$$J_T = \exp \left(\frac{-q\phi_b}{E_{00}} \right) \quad (3-10)$$

This expression clearly indicates that the lower the barrier and the higher the doping level, which increases E_{00} , the higher the current. This explicitly implies that the resistance is low. The key is then to find a metal with a small barrier which calls for a metal with a work function equal to or smaller than that of the semiconductor for the n-type case. For the p-type case, the same reasoning implies that the work function of the metal needs to be equal to or larger than that of the semiconductor, which is very hard to do for large-bandgap semiconductors. Additionally, the situation is exacerbated by the large hole mass which tends to decrease the E_{00} term, thus to increase the resistance. In

fact, the low hole concentration combined with a large hole effective mass precludes direct tunneling in p-type GaN.

3.3 Resistance of an ohmic contact

A metal-semiconductor contact is called an ohmic contact if its contact resistance is negligible compared to the bulk or spreading resistance of the semiconductor – the contact is thus not affecting the current/voltage (I/V) characteristics of the device. Fig. 3.7 shows I-V characteristic of an ohmic contact. Ideally, ohmic contacts do not contribute to the voltage drop across the device and do not alter the current-voltage relationship. Additionally, the contact must remain intact and robust regardless of the environment, and the contact characteristics must not change with storage and dynamic

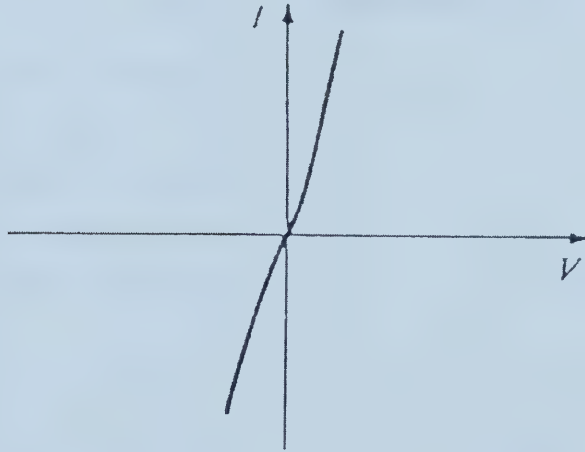


Figure 3.7 I-V characteristic of an ohmic contact.

operations.

The electrical properties of ohmic contacts are defined by a specific contact resistance, r_c ,^[17]

$$r_c = \left(\frac{\partial V}{\partial J} \right)_{V=0} \quad (\Omega \text{ cm}^2) \quad (3-11)$$

For a homogeneous contact of area A with a uniform current density, the contact resistance R_c is simply:

$$R_c = \frac{r_c}{A} \text{ } (\Omega) \quad (3.12)$$

The measured resistance R will be approximately equal to R_c for most sample geometries when $r_c \geq 10^{-2} \text{ } \Omega \text{ cm}^2$. For lower values of r_c , the spreading resistance of the semiconductor and the series resistance of the connecting wires and semiconductor substrate must be taken into account. Specific contact resistances of $< 10^{-4} \text{ } \Omega \text{ cm}^2$ are required for ohmic behavior, although values in the 10^{-6} to $10^{-7} \text{ } \Omega \text{ cm}^2$ range are most desirable.

The contact resistivity can be related to the sheet resistance by the relationship^[9] $\rho_c = \sqrt{r_c \cdot R_s}$, where ρ_c ($\Omega \text{ cm}$) is the contact resistivity, R_s ($\Omega/$) is the sheet resistance of the semiconductor beneath the contact, and r_c ($\Omega \text{ cm}^2$) is the specific contact resistance at the metal semiconductor interface.

3.4 Principles for forming ohmic contacts

There are three major methods for forming low resistance ohmic contacts:

- (1) A metal with a work function less than the work function of an n-type semiconductor, or greater than the

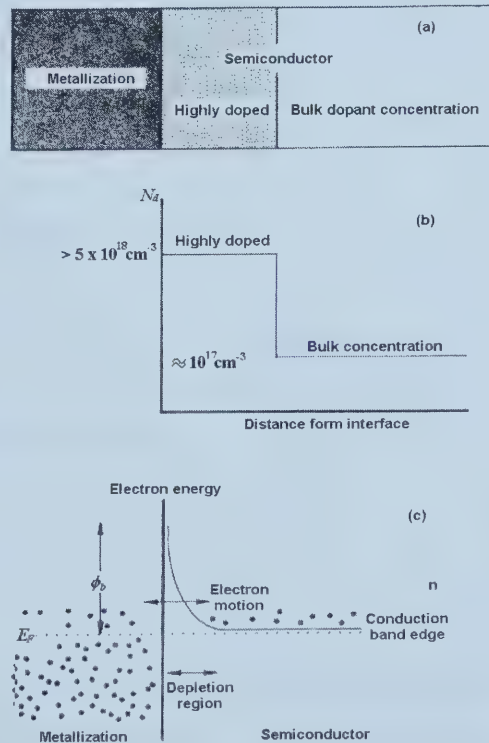


Figure 3.8 (a) Schematic of an ohmic contact structure to an n-type semiconductor. (b) Simplified plot of doping concentration of semiconductor in (a). (c) Simplified energy band diagram of metallization/semiconductor interface region.^[33]

work function of a p-type semiconductor, can form an ohmic contact to the semiconductor.

- (2) A semiconductor with an extremely narrow band gap, which is lattice matched to the employed semiconductor, can be epitaxially grown on the semiconductor device. This semiconductor should have high electron and hole mobilities and surface states pinned in the bandgap. Therefore, it forms an ohmic contact with almost every metal that is deposited onto it.
- (3) The most common commercialized method involves the formation of a very heavily doped ($> 5 \times 10^{18} \text{ cm}^{-3}$) thin layer of semiconductor material on the semiconductor surface, immediately adjacent to the metal (Fig. 3.8).^[33] The depletion region produced at the interface between the metal and the semiconductor is then so thin that field emission or tunneling of charge carriers may take place, giving a contact with very low resistance at zero bias.

3.5 Determination of the specific contact resistance

Four methods can be used to measure the specific contact resistance r_c for III-V semiconductors: (1) Transmission line model (TLM); (2) Cox and Strack technique; (3) Four-point method; (4) Schockley extrapolation technique.

3.5.1 Transmission line model (TLM)

The transmission line model (TLM) is the most widely used method for determining the specific contact resistance of ohmic contacts to semiconductor. The technique requires the formation of contacts with controlled geometry and evaluates the difference in resistance between equally sized pairs of contacts separated by different distances (l_1, l_2, \dots , see Fig. 3.9).^[36] The total resistance is given by $R_T = 2R_c + l \frac{R_s}{W}$, where the first terms represents twice the contact effective resistance R_c , which is the contribution from

the contact itself, while the second term is due to the semiconductor. The term R_s denotes the sheet resistance of the semiconductor layer. So the total resistance has a linear relationship to the separation distance of contacts. From Fig. 3.9(c), the effective contact resistance R_c can be determined,

$$2R_c = \frac{R_2 l_1 - R_1 l_2}{l_1 - l_2} \quad (3-13)$$

where R_1 and R_2 are the resistances measured between contacts spaced l_1 and l_2 apart,

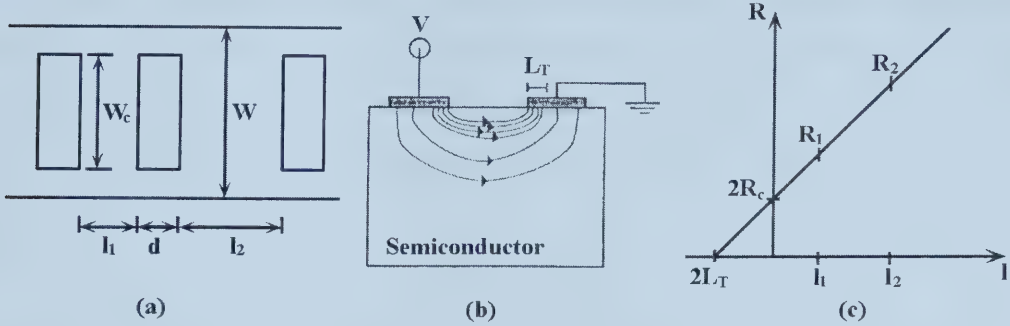


Figure 3.9 (a) Sample configuration for TLM characterization. (b) Schematic of current flow through planar contacts. Nearly all of the current flows through one transfer length, L_T , of the contacts' front edges. (c) Plot of the measured resistance against the contact separation.^[36]

respectively. In a planar contact configuration, nearly all of the current enters the semiconductor through a small area at the edge of the contact.^[35] The transfer length L_T is the length of this area as indicated in Fig. 3.9(b). This quantity is estimated by plotting the resistance of two pairs of contacts against the distance separating the individual contacts within each pair. The line connecting the points R_1 and R_2 crosses the resistance axis at the $2R_c$ point and intersects the distance axis at the $-2L_T$ point (see Fig. 3.9(c)). The specific contact resistance is calculated from the effective contact resistance R_c , the contact width W_c , and the transfer length L_T ,

$$r_c = R_c W_c L_T \quad (3-14)$$

The TLM technique relies on the assumption that the semiconductor material under the contact has not been doped differently than the bulk material, and the accuracy of the method depends on the ability to control the separation between the contacts. This

technique has been extended to transmission lines of circular geometries and to arbitrary shapes. The TLM technique is not accurate for specific contact resistance near and below $10^{-7} \Omega \text{ cm}^{-2}$.

3.5.2 Cox-Strack method

Fig. 3.10 shows the structure utilized in the Cox-Strack method, where the resistance of a circular contact of radius r on an n-type film of resistivity ρ and thickness t is to be determined. The current flow pattern is axial, through the layer to the heavily doped substrate. This structure requires metallization of both the back and the front surfaces of

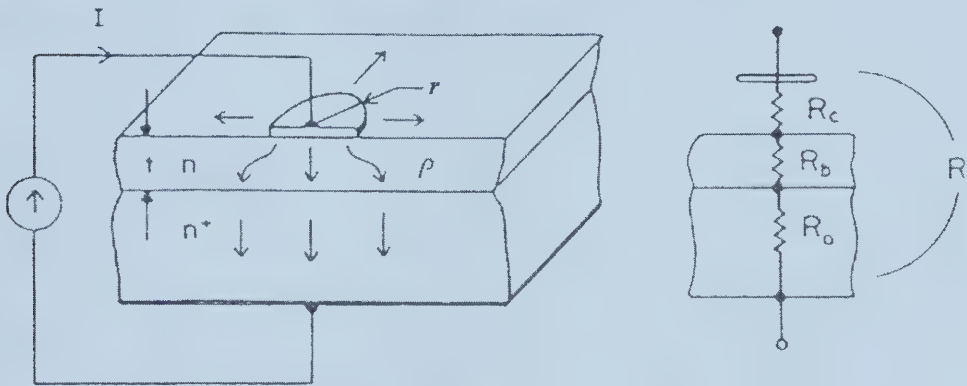


Figure 3.10 Measurement of the specific contact resistance using the Cox-Strack method. The circular ohmic contact has a radius r .^[34]

the semiconductor wafer, and can be used for either p- or n-type materials and for epitaxial or bulk layers. The total contact resistance R is composed of the contact resistance R_c , the spreading resistance R_b , and the semiconductor bulk resistance R_o . The specific contact resistance of the circular contact is

$$r_c = \pi a^2 \left[R - \frac{\rho}{a} F\left(\frac{a}{t}\right) - R_o \right] \quad (3-15)$$

where F is a function of the ratio a/t and was determined experimentally by Cox and Strack to be

$$F\left(\frac{a}{t}\right) \approx \frac{1}{\pi} \arctan\left(\frac{2t}{a}\right) \quad (3-16)$$

In practice, if the resistance of an array of contacts with different areas is measured, the spreading resistance is calculated for each contact using $R_b = \frac{\rho}{a} F\left(\frac{a}{t}\right)$, and a plot of $R - R_b$ vs. $1/a^2$ is made. A straight line fitted to the data points yields the values of r_c and R_0 (r_c/π is the slope of the straight line and R_0 is the intercept of the $R - R_b$ axis). The minimum value of r_c can be accurately determined. Two factors limit the accuracy of this technique: i) the accuracy in measurement of the contact radius r , and ii) the error in taking the difference between the two almost equal quantities R and R_b . For an n-type GaAs epitaxial layer with $r \geq 5 \mu\text{m}$, it is possible to measure r_c values down to approximately $1 \times 10^{-6} \Omega \text{ cm}^2$ with an error of about 25%.

3.5.3 Four-point method

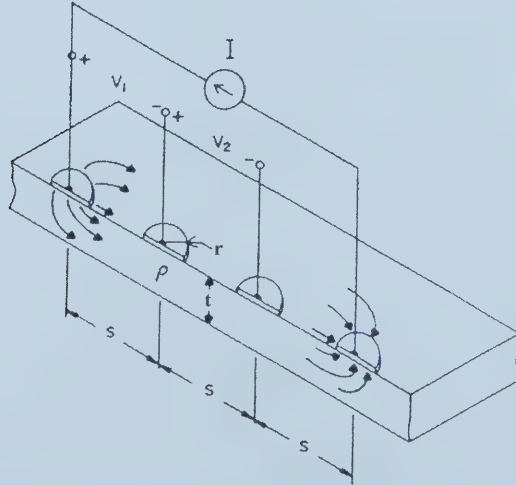


Figure 3.11 Measurement of the specific contact resistance by four-point probe method.^[34]

The four-point method requires metallization of only one surface of the wafer (see Fig. 3.11). Assuming that the resistance of the semiconductor film between contacts is the same everywhere, the specific contact resistance is given by

$$r_c = \pi r^2 \left[\frac{V_1}{I} - \frac{V_2}{I} \frac{\ln(3s/2r - 0.5)}{2 \ln 2} - R_b \right] \quad (3-17)$$

where r is the radius of contact, s is the separation between two contacts, I is the current flow through the system, V_1 , V_2 are the measured voltages, and R_b is the spreading contact resistance. If the thickness of semiconductor film $t \ll s$, $r \ll s$, and $\rho r^2 \ll r_c t$, the contribution of R_b can be ignored.

3.5.4 Shockley technique

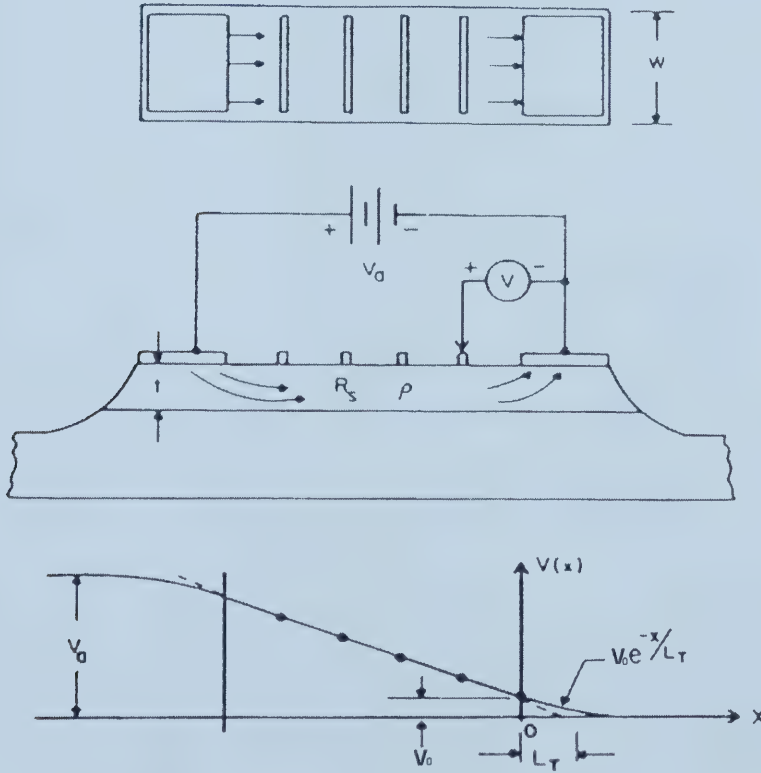


Figure 3.12 Measurement of the specific contact resistance by the Shockley technique. The voltage applied to the coplanar ohmic contact is V_a . The linear voltage distribution between the contacts is extrapolated to obtain the transfer length L_T .^[34]

Using the Shockley technique, the specific contact resistance can be expressed by

$$r_c = R_s L_T \quad (3-18)$$

where R_s is the sheet resistance of the semiconductor and L_T is the transfer length. As shown in Fig. 3.12, the technique includes measurement of the voltage drop $V_{(x)}$ along the surface of the semiconductor film between two planar ohmic contacts. The transfer length L_T can be determined by the extrapolated voltage V_0 , $V_x = V_0 \exp(-x / L_T)$. The minimum value of r_c that can be accurately measured using the Shockley technique is limited by the error in determination of L_T .

4. METAL-SEMICONDUCTOR CONTACTS TO GaN-BASED SEMICONDUCTORS

It is relatively difficult to form ohmic contacts to GaN-based semiconductors due to their wide band gap (3.39 eV). Because of the important role of ohmic contacts, as indicated initially by Foresi and Moustakas^[36], many papers have been published on the formation of ohmic contacts to GaN-based semiconductors. Most of the publications in this field report the experimental results for particular contact systems, i.e., the formation techniques and the contact properties; as well as, a limited amount of microstructural analysis work. The microstructures of metal/GaN-based semiconductor contacts are entirely dependent on the metallurgical system of choice and the contact process conditions. The contact morphology contains various intermetallic compounds composed of metals and Ga or N (from semiconductor), and those compounds exhibit various geometrical shapes and distributions because of structural incompatibility. Moreover, each phase has different carrier-conduction properties. Therefore, the carrier-transport nature of contacts is solely determined by the chosen metallization scheme and the interfacial microstructure. The specific contact resistance may be reduced by several orders of magnitude simply by optimizing the thermal processing conditions to achieve a low contact resistance microstructure. Because of the complexities of the reactions between metals and GaN-based semiconductors, and the lack of necessary information such as ternary and quaternary phase diagrams, thermodynamic data (heat of formation, free energy change of formation, etc.), kinetic data (diffusivity, reaction rates), and crystal structures, although significant amounts of experimental work have been done, at present, the fabrication of contacts is still more of an art than a science. There is still a long way to go in achieving contacts that give optimum device performance. This chapter presents a comprehensive literature review of the published results with emphasis on ohmic contacts to n-type GaN-based semiconductors.

4.1 Ohmic contacts to n-GaN

Table 4.1 The specific contact resistances for different published metallization schemes to n-GaN.

r_c (Ω cm ²)	Metallization (nm)	Doping (cm ⁻³)	Annealing	Other	Source
1.6×10^{-3}	Au	3×10^{18}	10 min at 575°C	reducing gas	[36]
1.2×10^{-4}	Al	3×10^{18}	10 min at 575°C	reducing gas	[36]
8×10^{-6}	Ti/Al (20/100)	$\sim 10^{17}$	30 s at 900°C	N ₂	[37]
8.9×10^{-8}	Ti/Al/Ni/Au (15/220/40/50)	4×10^{17}	30 s at 900°C	N ₂	[38]
3.6×10^{-8}	Ti/Au (3/300)	4×10^{20}	No annealing	Si-implantation	[39]
4×10^{-6}	Ti/Al (35/115)	7×10^{17}	15 s at 600°C	Ar	[40]
6×10^{-5}	Pd/Al (25/125)	7×10^{17}	30 s at 600°C	IAr	[40]
8×10^{-6}	Al (150)	7×10^{17}	8 min. at 600°C	Ar/4% H ₂	[41]
6.5×10^{-5}	Ti/Ag (15/150)	1.7×10^{19}	No annealing	Si-implantation	[42]
5×10^{-6}	Ta/Al (35/115)	7×10^{17}	15 s at 600°C	Ar	[43]
1.2×10^{-5}	Pd/Al (25/100)	2.8×10^{17}	30 s at 650°C	N ₂	[44]
$< 1 \times 10^{-3}$	PtIn ₂ (150)	5×10^{17}	60 s at 800°C	Ar	[45]
8.0×10^{-5}	W (50)	1.5×10^{19}	60 s at 1000°C	N ₂	[46]
1.2×10^{-6}	Ti/Au (25/190)	1.2×10^{18}	900°C		[47]
4×10^{-6}	Ti (150)	7×10^{17}	60 s at 800°C	N ₂	[48]
4×10^{-6}	Ti (150)	7×10^{17}	60 s at 900°C	Ar	[48]
4×10^{-5}	TiN (200)	7×10^{17}	60 s at 800°C	Ar	[48]
6×10^{-6}	Ti/TiN (5/200)	7×10^{17}	60 s at 800°C	Ar	[48]
6.0×10^{-7}	Ti/Al/Ti/Au (30/100/30/30)	1.4×10^{20}	30 s at 750°C		[49]
1.16×10^{-8}	Ti/Al	1×10^{19}	60 min at 500°C	N ₂	[50]
8.4×10^{-5}	Ti/Al/Pt/Au (30/100/40/200)		20 s at 650°C	N ₂	[51]

Table 4.1 lists specific contact resistances for different metallization schemes to n-GaN. Since 1993, when Foresi and Moustakas^[36] made the first ohmic contact ($r_c = 1.2 \times 10^{-4} \Omega$ cm²) to n-GaN using Al annealed in a reducing environment at 575°C for 10 min, researchers have made remarkable progress. Large amounts of various metals have been utilized to form ohmic contacts to n-GaN. Fan, *et al.*^[38] obtained a specific contact resistance as low as $8.9 \times 10^{-8} \Omega$ cm² using a Ti/Al/Ni/Au multilayer metallization. The lowest specific contact resistance achieved so far, with a value of $1.16 \times 10^{-8} \Omega$ cm², has been produced with an annealed Ti/Al metallization by Lee *et al.*^[50] However, the

mechanisms of the ohmic behavior of the different metallization schemes are still under discussion. Most of the authors deem that two models, either a low Schottky barrier or a tunneling contact, can be used to explain ohmic behavior of metal contacts to n-GaN.

4.1.2 Factors influencing the specific contact resistance of metal contacts

Generally, there are five factors that influence the specific contact resistance of metal contacts to GaN-based semiconductors.

4.1.2.1 Contact metal

According to the Schottky-Mott theory ($\phi_b = \phi_m - \chi_s$), the simplest considerations of Schottky barrier formation between metals and semiconductors rely on the difference in work functions of the two materials to predict the barrier height. For most important semiconductors, such as Si and GaAs, because of the existence of surface states that pin the Fermi level at the interface, the barrier height does not depend on the work function difference. But for GaN-based semiconductors, the situation is different. For

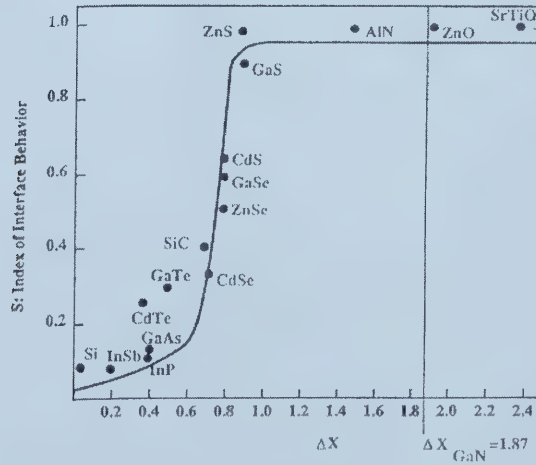


Fig. 4.1 Dependence of $S = d\phi_b/d\phi_m$ (change in barrier height over the change in metal work function) on the electronegativity difference between the components of the compound.^[52]

semiconductors with a large electronegativity difference, the bunching of surface states near the band edges, where they have less effect on the surface Fermi level position, results in the direct dependence of the barrier height on the work function difference between metals and semiconductors.^[35] Kurtin *et al*^[52] correlated the dependence of the barrier height on the work function difference to the ionicity of the semiconductor as shown in Fig. 4.1. In this figure, the vertical axis is a parameter S which is defined as the change in barrier height over the change in metal work function ($d\phi_b/d\phi_m$) and the horizontal axis is the electronegativity difference between the components of a compound which is a measure of the compound's ionicity. The electronegativity difference for GaN is 1.87 eV.^[36] This puts GaN above the knee of the curve implying that Schottky barriers on GaN should have barrier heights which depend directly on the work function difference between the metal and GaN, and it significantly simplifies the metallization schemes of GaN-based semiconductors. The electron affinity of GaN (χ_{GaN}) has been measured to be 4.2 eV.^[53] Therefore, any metal with a work function equal to or lower than this value should form essentially ohmic contacts to n-type GaN and any metal with a work function higher should form a rectifying contact to n-type GaN.

Table 4.2 Contact characteristics of 17 metals to n-GaN along with their corresponding metal work functions^[53]

Metal	Metal work function (eV)	Current-Voltage behavior
Sc	3.5	Ohmic
Hf	3.9	Ohmic
Zr	4.05	Ohmic
Al	4.28	Ohmic
V	4.3	Ohmic
Nb	4.3	Slightly rectifying
Ti	4.33	Slightly rectifying
Cr	4.5	Slightly rectifying
W	4.55	Slightly rectifying
Mo	4.6	Slightly rectifying
Ag	4.26	Schottky
Cu	4.65	Schottky
Co	5	Schottky
Au	5.1	Schottky
Pd	5.12	Schottky
Ni	5.15	Schottky
Pt	5.65	Schottky

Schmitz *et al*^[53] formed contacts consisting of various single layer metals to the same epitaxial grown n-GaN and measured the current-voltage (I-V) characteristics for these metal-semiconductor systems. Table 4.2 lists contact characteristics of 17 metals to n-type GaN, along with their corresponding work functions. Their results showed that the contact characteristics depends on the metal work function, the contacts go from being ohmic to Schottky as ϕ_m becomes larger. This correlation between the barrier height and metal work function is significantly stronger than for GaAs and other III-V semiconductors. They also found that the surface state density of GaN was approximated to be very similar to CdS and almost a factor of ten less than GaAs. According to Table 4.2, Sc, Hf, Zr, Al, and V showed a highly linear nature in terms of I-V characteristics, suggesting their potential use in forming high quality ohmic contacts. An exception to this trend was observed for Ag, which exhibited stronger rectifying behavior than Nb, Ti, Cr, W, and Mo even though its ϕ_m is lower than each of these five metals. The reason for this discrepancy is unclear, however, uncertainties in the crystallinity of the deposited Ag, which has a strong effect on ϕ_m , may be one plausible explanation.

4.1.2.2 Doping concentration of semiconductor

After studying Table 4.1, it can be found that even with optimization of contact composition and annealing times and temperatures, the lowest specific contact resistances (r_c) have been obtained only on the most heavily doped semiconductor surfaces. The higher the doping concentration, the higher the charge carrier concentration in the semiconductors. When a contact is fabricated to a heavily doped semiconductor, the tunneling process will dominate the current transport. According to Eq. 3-10, in the tunneling process, the specific contact resistance strongly depends on the doping concentration.

4.1.2.3 Pre-metallization surface treatments

It is now well established that the Schottky barrier heights increase monotonically with metal work functions, as might be expected from the highly ionic nature of GaN. However, the surface treatment prior to metallization is also a critical parameter. The Schottky-Mott model also indicates that the cleanliness of the interface plays an important role in its electrical behavior – particularly in the minimization or elimination of any insulating layers at the interface. Common metallization schemes include the following surface treatments: wet chemical etching, reactive ion etching (RIE), Si implantation, and pre-annealing.

- (1) Wet chemical etching includes putting the semiconductors into acidic and basic solutions and rinsing with deionized (DI) water, in a step by step manner. The surface contamination of semiconductor is decreased, thereby increasing metallization quality.
- (2) Reactive ion etching utilizes reactive gas ions to sputter the semiconductor surface. The results of Mieteale *et al.*^[54] showed that chemically assisted ion beam etching (CAIBE) is strongly responsible for the changing of the performance of metal contacts on group III nitrides. They found that etching parameters, such as the ion energies and the composition of the etching gases, influence the specific contact resistance of the final contact, especially the composition of the etching gases. They proposed that CAIBE and sputter etching with Ar or ArCl₂ leave the surface more highly n doped, whereas sputter etching with N₂ gas partially saturates the N vacancies as an intrinsic doping source and therefore results in a more rectifying character and a higher contact resistance. They even suggest two competing processes in the case of sputtering of the GaN surface by Ar⁺ ions: on the one hand the spatial enhancement of N vacancies leads to higher n doping near the surface and therefore lowers the contact resistance; on the other hand the implantation of Ar⁺ ions results in an increasing sheet resistance beneath the contact area owing to lattice damage. Ruvimov *et al.*^[55] summarized several possible explanations for the

reduction of contact resistance by RIE. Firstly, RIE provides a method to clean the surface and remove any oxide layer. Secondly, it increases the GaN surface roughness due to the preferential etching of dislocated material and, hence, increases the contact area. Thirdly, RIE causes radiation damage near the GaN surface and, hence, increases the point defect density in the thin GaN region near the surface. As a result, diffusion of metals into GaN is more rapid, even during the metal deposition. Thus, the formation of a good contact is expected even before annealing. Indeed, atom diffusion is enhanced along dislocation cores so that dislocations might be considered as pipes for metal migration.

- (3) Si-implantation can increase the doping concentration of n-GaN, and increase the charge carriers in the semiconductor. As a result, it can improve the tunneling process in current transport.
- (4) Liu *et al*^[56] reported that the pre-annealing of n-GaN in an N₂ ambient at elevated temperature (i. e., 850°C) increases the electron concentration in the layers, and that this annealing step may improve the contact resistance. Maffei *et al* also found that the annealing could cause an upward band bending, prior to metallization.^[57]

4.1.2.4 Annealing

Generally, in order to obtain the optimal electrical properties, annealing after metal deposition is necessary. Precise control of annealing parameters (e.g., temperature, time, and environment) is critical for obtaining the lowest specific contact. The possible optimal conditions are within 15 to 30 s at 600 to 900°C, using rapid thermal annealing (RTA) in N₂ or Ar ambient.

4.1.2.5 Reactions

Upon annealing, there will be reactions between contact metals, as well as contact metal and semiconductor. These reactions may either be beneficial forming ohmic contacts or degrade the ohmic contact. Only the reactions whose products have good electrical and mechanical properties are desired. The parameters, which influence reactions, include contact metals (metal selection and metal layer thickness) and annealing setting (e.g., time, temperature, pressure, and environment). Investigation of binary, ternary, even quaternary phase diagrams are required.

4.1.3 Published data on ohmic contacts to n-GaN

Many attempts have been made to form ohmic contacts to n-GaN; Ti/Al-based ohmic contacts have become the standard metallization scheme to n-GaN due to their relatively good ohmic, thermal, and morphological behavior.

4.1.3.1 Al, Au/n-GaN

Foresi and Moustakas^[36] carried out the first contact investigation on GaN. Al and Au were deposited on the n-type GaN ($N_D = 10^{18} \sim 10^{20} \text{ cm}^{-3}$) surface. Current-voltage characterization showed that the as-deposited aluminum contacts were ohmic while the as-deposited gold contacts were rectifying. The results were attributed to the barrier height of the metal used. After annealing, the specific contact resistance of the aluminum contacts increased by about 50% because of the formation of an interfacial AlN layer during the annealing process. The ohmic formation of the gold contacts after annealing at 575°C for 10 minutes in a reducing ambient was attributed to the Au diffusion in GaN. The lowest specific contact resistances of ohmic aluminum and gold contacts were found to be $10^{-3} \sim 10^{-4} \Omega \text{ cm}^2$.

4.1.3.2 Al/Ti/n-GaN

Lin *et al.*^[37] deposited an Al/Ti (100/20 nm) bilayer on MBE grown n-GaN ($N_D = \sim 10^{17} \text{ cm}^{-3}$). After rapid thermally annealing for 30 s at 900°C in a N₂ atmosphere, the lowest value for the specific contact resistance ($8 \times 10^{-6} \Omega \text{ cm}^{-2}$) was obtained. A layer of face-centered-tetragonal TiAl phase was identified by XRD and AES analysis. Based on Lin's study, Ti/Al-based metallizations started to attract researchers' interests.

4.1.3.3 Au/Ni/Al/Ti/n-GaN

A very low resistance ($8.9 \times 10^{-8} \Omega \text{ cm}^2$) multilayer ohmic contact to n-GaN was obtained by Fan *et al.*^[38] A multilayer Ti/Al/Ni/Au (15/220/40/50 nm) metallization was deposited on n-GaN ($N_D = 4 \times 10^{17} \text{ cm}^{-3}$) preceded by a RIE. Contacts were rapidly thermal annealed for 30 s at 900°C in a N₂ atmosphere. The proposed current transport mechanism is tunneling. RIE processing did help to form ohmic contacts by removing the surface oxide layer on the semiconductor. The results excluded the other possible advantages of RIE, e.g., preferential sputtering of N (thus generating N vacancies with donor characteristics) and formation a donor-like layer in the ion-damaged region. XRD and Auger electron spectroscopy (AES) analysis indicated the formation of face-centered tetragonal TiAl and an Au-Ni phase in contact with GaN after annealing. It was found that a thicker Al layer would prevent outdiffusion of Ga from the metal-semiconductor interface to the top Au layer. Together with Ti, Al also prevented the interdiffusion of excess Ni and possibly Au from the top layer to the metal-semiconductor interface. The main advantage of this metallization scheme was that the Au-Ni alloy formed over the TiAl layer was very robust. The oxidation of aluminum and the tendency of aluminum to ball up even at very high temperature were prevented. Therefore, this led to good ohmic behavior and morphology, as well as good thermal stability.

4.1.3.4 Au/Ti/n-GaN

Burm *et al.*^[39] implanted Si in MBE deposited GaN at a doping density of about $4 \times 10^{20} \text{ cm}^{-3}$ to decrease the contact resistance of the contact, followed by an activation anneal at 1150°C for 30 s. The overlying Ti/Au (3/300 nm) metals were evaporated on the doped n-GaN surface. No annealing was performed after metallization. The measured minimum specific contact resistance was $3.6 \times 10^{-8} \Omega \text{ cm}^2$. The main drawback of this method is that high temperature activation anneal, which may decompose GaN.

Smith *et al.*^[47] also reported Au/Ti (25/190 nm) ohmic contacts to n-GaN ($1.2 \times 10^{18} \text{ cm}^{-3}$). After annealing at 900°C , the lowest specific contact resistance of $1.2 \times 10^{-6} \Omega \text{ cm}^2$ was reached. It was found that a layer of TiN formed after annealing. The current transport mechanism of the ohmic contact was attributed to tunneling. The presence of the Au overlayer on top of a thin Ti layer improved the adhesion of the Ti to the GaN surface during the annealing process, as well as provided a lower series resistance in the contact circuit as a whole.

4.1.3.5 Al/Ti/n-GaN

Luther *et al.*^[40] deposited Ti/Al (35/115 nm) on a n-GaN layer ($7 \times 10^{17} \text{ cm}^{-3}$) followed by annealing in Ar at 600°C for 15 s. A specific contact resistance of $4 \times 10^{-6} \Omega \text{ cm}^2$ was obtained. Using high-resolution transmission electron microscopy (HRTEM), a thin pseudomorphic AlN layer (2-3 nm) was observed at the metal/GaN interface. The interfacial layer had a *c*-plane (002) lattice spacing of $0.248 \pm 0.003 \text{ nm}$ and an *a*-plane (100) spacing matching that of GaN (0.276 nm), and the identification of this layer as AlN was consistent with chemical analysis by energy dispersive x-ray spectroscopy (EDX). Moreover, the formation of this interfacial AlN layer coincided with the onset of ohmic behavior and therefore may be responsible. The authors also reported Al ohmic contacts ($8 \times 10^{-6} \Omega \text{ cm}^2$) on n-GaN ($7 \times 10^{17} \text{ cm}^{-3}$) annealed in forming gas (Ar/4% H_2) at

600°C.^[41] The ohmic contact formation was attributed to reduction of the native oxide on GaN by aluminum and the low work function of the aluminum metal.

To the best of our knowledge, the lowest specific contact resistance for ohmic contact to n-GaN was obtained by Lee's group.^[50] They used Al/Ti to n-GaN ($1 \times 10^{19} \text{ cm}^{-3}$). The lowest specific contact resistance was $1.16 \times 10^{-8} \Omega \text{ cm}^2$ and was achieved with furnace annealing at 500°C for 60 min. Auger electron spectroscopy depth profiles revealed that Al diffused into the Ti layer and came into contact with the GaN surface. It was considered that the low specific contact resistance was realized due to Al contact to the GaN layer with a smooth surface morphology.

4.1.3.6 Ag/Ti/n-GaN

A bilayer Ti/Ag (15/150 nm) ohmic contact ($6.5 \times 10^{-5} \Omega \text{ cm}^2$) for highly doped n-GaN ($2 \times 10^{19} \text{ cm}^{-3}$) was reported by Guo *et al.*^[42] The GaN semiconductor was doped with Si and etched using RIE before metal deposition. No annealing was performed after metal deposition. The authors considered that the ohmic contact formation was due to the high doping concentration in the semiconductor and the low work function of Ti. A thick Ag layer was utilized to alter the effective contact resistance value of the high resistivity Ti layer.

4.1.3.7 Al/Ta/n-GaN

Luther *et al.*^[43] also developed a Ta/Al metallization for n-GaN. Ta/Al (35/115 nm) contacts to n-GaN became ohmic after annealing for 3 min at 500°C or for 15 s at 600°C. A minimum specific contact resistance of $5 \times 10^{-6} \Omega \text{ cm}^2$ was measured after contacts were repatterned with an Al layer to reduce the effect of a high metal sheet resistance. AES depth profiles revealed that ohmic contacts only formed after intermixing of the Ta and Al layers.

4.1.3.8 Al/Pd/n-GaN

Metallization schemes involving of Pd have been investigated extensively for low resistance ohmic contacts on materials such as GaAs and InP. It is known that Pd easily penetrates native surface oxides and allows subsequent metals such as Ge to diffuse into the semiconductor without spiking. In addition, the formation of ohmic contacts is found to occur at lower annealing temperatures with Pd as an interlayer between the semiconductor and subsequent metal layers. Ping *et al.*^[44] investigated ohmic contact formation to n-GaN ($2.8 \times 10^{17} \text{ cm}^{-3}$) using Pd/Al metallizations (25/100 nm). A minimum specific contact resistance of $1.2 \times 10^{-5} \Omega \text{ cm}^2$ was obtained upon annealing at 650°C for 30 s in N₂ ambient.

Luther *et al.*^[40] also made Pd/Al ohmic contacts to compare with Ti/Al contacts. After annealing at 600°C for 15 s in Ar, Pd/Al (25/125 nm) contacts reached their lowest specific contact resistance of $6 \times 10^{-5} \Omega \text{ cm}^2$. AlN was found at the metal-GaN interface after annealing and ohmic contact formation was attributed to its presence.

4.1.3.9 PtIn₂/n-GaN

Ingerly *et al.*^[45] deposited 150 nm PtIn₂ films onto n-GaN $5 \times 10^{17} \text{ cm}^{-3}$ using DC magnetron sputtering from a single alloy target. After annealing for 60 s at 800°C in Ar, a specific contact resistance less than $1 \times 10^{-3} \Omega \text{ cm}^2$ was obtained. The results of both Auger electron spectrometry (AES) depth profiles and x-ray diffraction (XRD) suggested the formation of (In_xGa_{1-x})N through a solid-state reaction at the contact interface. The formation of (In_xGa_{1-x})N was expected based on the estimated phase diagram information, and the authors proposed that the low barrier phase (In_xGa_{1-x})N was responsible for the contact's ohmic behavior.

4.1.3.10 W/n-GaN

W (50 nm) was found to produce low specific contact resistance ($\sim 8.0 \times 10^{-5} \Omega \text{ cm}^2$) ohmic contacts to n-GaN ($1.5 \times 10^{19} \text{ cm}^{-3}$) with limited reaction between the metal and semiconductor, up to 1000°C .^[46] The formation of $\beta\text{-W}_2\text{N}$ and W-N interfacial phases were deemed responsible for the electrical integrity observed at these annealing temperatures. No Ga out-diffusion was observed on the surface of thin W contacts even after 1000°C , 1 min anneals.

4.1.3.11 TiN/n-GaN or TiN/Ti/n-GaN

Smith *et al.*^[47] and Luther *et al.*^[48] both tried to deposit TiN layers onto the n-GaN surface directly. Luther *et al.* obtained a specific contact resistance as low as $4 \times 10^{-5} \Omega \text{ cm}^2$ for n-GaN with a doping concentration of $7 \times 10^{17} \text{ cm}^{-3}$, after annealing at 400°C for 1 min. For comparison purposes, they also investigated Ti and Ti/TiN metallization schemes. It was found that Ti (150 nm) contacts annealed in N_2 became ohmic after 1 min at 700°C and reached a minimum specific contact resistance of $4 \times 10^{-6} \Omega \text{ cm}^2$ after 1 min at 800°C . The same Ti contacts annealed in Ar required 20-25 min at 700°C to become ohmic and also reached a minimum specific contact resistance of $4 \times 10^{-6} \Omega \text{ cm}^2$ after 1 min at 900°C . Ti/TiN (5/200 nm) contacts became ohmic ($6 \times 10^{-6} \Omega \text{ cm}^2$) after being annealed for 1 min at 700°C , similar to Ti contacts annealed in N_2 . Depth profiles of Ti and Ti/TiN contacts showed that the presence of TiN at the metal-GaN interface was a necessary condition for ohmic contact formation. The above results revealed that Ti contacts annealed in N_2 became ohmic more rapidly than Ti contacts annealed in Ar owing to the supply of nitrogen from the gas environment which allowed a thick layer of TiN to form at the contact-GaN interface in a shorter time. Deposited TiN contacts became ohmic after being annealed at a much lower temperature than was needed for Ti contacts. However, TiN contacts did not reach as low a specific contact resistance as the reacted Ti contacts. By putting a thin reactive Ti layer next to the GaN in the Ti/TiN

contact scheme, the contacts became ohmic very quickly and reached as low a specific contact resistance as the Ti contacts, displaying similar characteristics to Ti contacts annealed in nitrogen. Lower specific contact resistance was the result of the reaction between Ti and the GaN layer. However, reaction with the GaN alone did not result in ohmic behavior; formation of a low work function phase, TiN ($\phi_m = 3.74$ eV) in this case, was also one of the crucial factors. One advantage of the Ti/TiN contact structure was that the amount of reaction with the GaN could be controlled through the Ti layer thickness.

4.1.3.12 Au/Ti/Al/Ti/n-GaN

Wang *et al.*^[49] developed successful Ti/Al/Ti/Au metallization schemes to n-GaN. Multilayer Ti/Al/Ti/Au (30/100/30/30 nm) was deposited on the n-GaN ($1.40 \times 10^{20} \text{ cm}^{-3}$). Contacts with a specific contact resistance as low as $6.0 \times 10^{-7} \Omega \text{ cm}^2$ were obtained after annealing the sample for 30 s at 750°C in a rapid thermal annealer. The Ti placed on top of the traditional Ti/Al contact appeared to have the advantage of tying up the excess Al; therefore it did not form a mottled contact. Some of the additional Ti-Al intermetallic alloys that formed also had beneficial effects. The Ti-Au layer formed a robust upper portion of the composite, which enabled the contacts to have high-temperature applications.

4.1.3.13 Au/Pt/Al/Ti/n-GaN

Zhao *et al.*^[51] achieved successful ohmic contacts ($8.4 \times 10^{-5} \Omega \text{ cm}^2$) by annealing Ti/Al/Pt/Au (30/100/40/200 nm) at 650°C for 20 s in N_2 to n-GaN. The Ti/Al/Pt/Au contacts showed better thermal stability than Al contacts.

4.1.3.14 Al/Nd/n-GaN

After annealing at 600°C for 30 s using RTA, an ohmic contact ($8 \times 10^{-6} \Omega \text{ cm}^2$) with Nd/Al was obtained to n-GaN ($1 \times 10^{18} \text{ cm}^{-3}$) by Lee *et al.*^[58] It was found that the reduced specific contact resistance was the result of the incorporation of nitrogen with Nd. However, the penetration of Al atoms deteriorated the ohmic behavior due to oxidation of the Al.

4.1.4 Microstructure

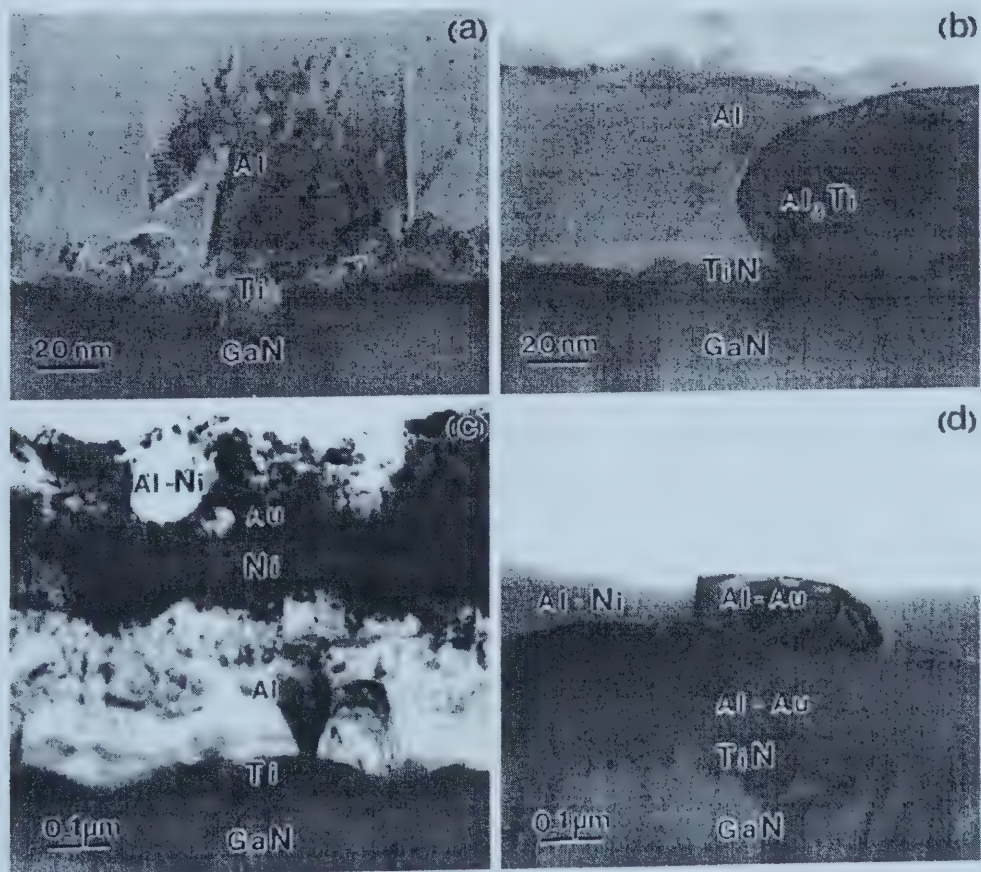


Fig. 4.2 Bright field TEM micrographs of Ti/Al (a), (b) and Ti/Al/Ni/Au (c), (d) contacts in cross section before (a), (c) and after (b), (d) annealing.^[55]

A limited number of researchers have performed microstructural analysis of ohmic contacts to n-GaN.

Ruvimov *et al.*^[55] did microstructural analysis of Ti/Al (20/100 nm) and Ti/Al/Ni/Au (15/220/40/50 nm) ohmic contacts for n-GaN. Figure 4.1 shows typical cross-sectional TEM images of Ti/Al ((a) and (b)) and Ti/Al/Ni/Au ((c) and (d)) contacts before ((a) and (c)) and after ((b) and (d)) thermal annealing. The surfaces of all specimens were very rough due to the RIE prior to metal deposition. The authors found that all of the as-deposited Ti layers were textured polycrystalline materials with *c*-planes of the metal grains mostly parallel to the *c*-plane of GaN. While no significant interdiffusion was detected by EDX between the Ti and Al in the as-deposited samples, the formation of an Al-Ni alloy was observed even before thermal annealing. Annealing did not change the surface morphology of the GaN significantly, but led to metal interdiffusion and alloying. The thickness of the metal composite layer decreased after annealing due to interdiffusion and formation of alloys with higher densities than that of pure Al. In Ti/Al contacts, annealing caused formation of a polycrystalline Al₃Ti phase with the *c*-plane almost parallel to that of GaN. In Ti/Al/Ni/Au contacts, the top layer consisted mostly of an Al-Ni phase with some grains of an Al-Au phase. The middle layer consisted mostly of an Al-Au phase with some Al-Ni grains. The bottom layer contained mostly Al-Ti and Ti-N phases. Other species were also present in the layer. EDX analysis of the GaN interface indicated the presence of 61.5 at. % Ti, 26.2 at. % Al, 6.8 at. % Ga, 3.8 at. % Au, and 1.6 at. % Ni.

HRTEM analysis (not shown here) showed a thin textured polycrystalline interfacial layer of cubic TiN on the GaN surface in both metallizations after annealing. A thin TiN layer was detected by electron diffraction at the Ti-GaN interface even for the as-deposited sample. The thickness of this TiN layer increased to 5 nm after annealing of the Ti/Al contact and to 10-15 nm for the Ti/Al/Ni/Au contact. The orientation relationship between the TiN layer and the GaN was determined from electron diffraction patterns as: $\{111\}_{\text{TiN}}//\{00.1\}_{\text{GaN}}$, $[110]_{\text{TiN}}//[11.0]_{\text{GaN}}$, and $[112]_{\text{TiN}}/[10.0]_{\text{GaN}}$. The TiN grains were often in a twinned orientation. The mismatch in the lattice parameters of TiN and GaN is

about 5.6-6.0%. The interface between the TiN grains and the GaN was quite abrupt, but the GaN region near the interface contained many structural defects. The authors believed these were possibly N vacancies.

Smith *et al.*^[47] investigated Ti, TiN, and Ti/Au ohmic contacts using TEM. The single Ti layer contact samples debonded easily at the metal-GaN interface during the cross-section TEM sample preparation procedure as a result of poor adhesion. HRTEM images showed a sharp interface of polycrystalline, fine-grained Ti with the GaN surface at the as-deposited Ti/GaN interface. After annealing at 900°C, Ti transformed into TiN. The TiN (111) plane was parallel to the GaN (0002) basal plane. In Ti/Au contacts, the Ti layer had almost completely transformed to TiN, after annealing at 900°C. The majority of the TiN was at approximately the same orientation, with the TiN (111) plane parallel to the GaN (0002) plane. Small regions of unreacted polycrystalline Ti adjacent to the bottom of the Au layer suggested that the transformation of Ti to TiN began at the Ti/GaN interface and progressed outward. Single TiN layer contacts also showed preferred orientation as $(111)_{\text{TiN}} // (0002)_{\text{GaN}}$ before and after annealing.

Contrary to the above results, Luther *et al.*^[40] reported a thin AlN interfacial layer rather than TiN. A thin (2-3 nm) layer of AlN was observed by HRTEM at the interfaces of Ti/Al and Pd/Al contacts annealed at 600°C for 15 and 30 s. The measured *c*-plane lattice spacing of the interfacial layer was 0.248 ± 0.003 nm and the *a*-plane spacing was the same as that of GaN (0.276 nm). The *a* planes extended up from the GaN through the interfacial layer, indicating that the AlN layer was pseudomorphic and under tensile strain.

4.2 Ohmic contacts to n-AlGaN

AlGaIn/GaN heterostructure field effect transistor (HFET) structures have shown the greatest potential for commercialization in the short term. Like n-GaN, formation of ohmic contacts to n-AlGaIn is also a crucial issue to improve the performance of the

devices. Because a higher Al composition leads to a higher density of sheet charge in the conducting channel, there is a trend to increase Al composition of the AlGa_N layer in the device structure.^[59] However, it is generally more difficult to produce good ohmic contacts to the channel through an AlGa_N layer.

The electron affinity of Al_xGa_{1-x}N, $\chi_{Al_xGa_{1-x}N}$, decreases from 4.2 eV (χ_{GaN}) to 2.05 eV (χ_{AlN}) as x increases from 0 to 1. The constraint for forming an ohmic contact to n-type AlGa_N, $\phi_m \leq \chi_{Al_xGa_{1-x}N}$, thus demands the contact material to have an increasingly lower electronic work function as the Al content increases. Similarly, as the Al fraction increases in AlGa_N, so does the anticipated Schottky barrier height for a given metal contact.^[53] The ohmic behavior of the contact seems to be extremely sensitive to the Al fraction of AlGa_N layer. As the aluminum fraction increases, the electronic properties of the existing contacts change due to an increasing band gap and decreasing electron affinity of AlGa_N. The higher band gap in AlGa_N compared with Ga_N can also lead to a lower doping efficiency of N vacancies in AlGa_N.^[11] Moreover, the presence of Al in AlGa_N increases the complexity of reaction during annealing. Therefore, new metallization schemes may have to be developed to accomplish good contact formation to AlGa_N.

Table 4.3 gives the specific contact resistances for different metallization schemes to n-AlGa_N/Ga_N HFET structures.

Table 4.3 The specific contact resistances for different published metallization schemes to n-AlGa_N/Ga_N ($n_s\mu$ is the sheet charge-mobility product)

r_c (Ω cm ²)	Metallization (nm)	Doping (cm ⁻³)	Annealing	Other	Source
3.20×10^{-6}	Ti/Al (30/71)	$n_s\mu = 0.82 \times 10^{16}$ (V s) ⁻¹	20 s at 950°C in N ₂	Preannealing, RIE	[56]
5.6×10^{-6}	Ti/Al (150/20)	$\sim 6.2 \times 10^{20}$	80 s at 950°C	Si-implantation	[9]
3.44×10^{-6}	Ti/Al/Ti/Au (20/100/45/50)	7×10^{19}	60 s at 800°C		[13]
5.95×10^{-7}	Pd/Al/Ti/Au (20/100/45/55)	7×10^{19}	60 s at 800°C		[13]
7.7×10^{-6}	Ti/Al/Ni/Au (20/200/40/40)	$n_s\mu = 3 \times 10^{16}$ (V s) ⁻¹	30 s at 830°C		[59]
2.8×10^{-6}	Ti/Al/Ni/Au (50/40/220/15)		60 s at 700°C	In Ar	[8]
5×10^{-7}	Ta/Ti/Al (50/50/50)		40 s at 950°C	In forming gas	[12]
2.1×10^{-5}	NiAl (120)	2.4×10^{18}	5 min. at 850°C	Ar	[60]

4.2.1 Phase equilibria

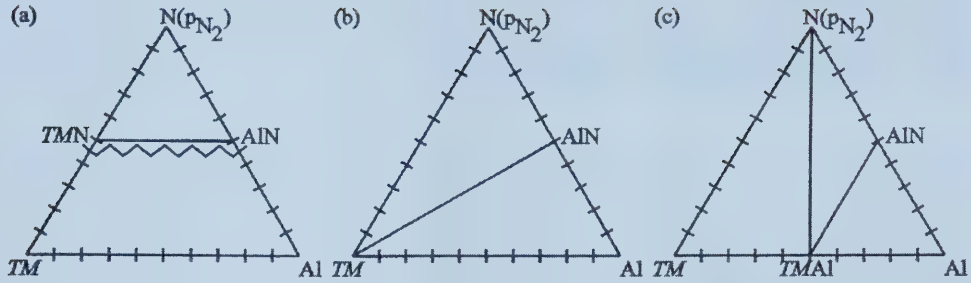


Figure 4.3 Hypothetical ternary phase diagrams illustrating key tie-line configuration of three different classes. (a) Stable metal nitride class. (b) Stable metal class. (c) Stable metal aluminide class.^[53]

In most metallization schemes, annealing is necessary to produce ohmic behavior. During annealing processes, reactions between metallization metals, as well as metal and semiconductor generally occur. Therefore, controlled metallurgical reactions are often necessary to achieve low resistance contacts. An understanding of the relevant phase equilibria in the metal-semiconductor systems and the thermodynamic driving forces for interdiffusion is important and can dramatically decrease the number of experiments that must be carried out.

Schweitz and Mohney^[53] studied phase equilibria in transition metal Al-Ga-N systems and thermal stability of contacts to AlGa_{0.5}N. There are 3 classifications in transition metal-Al-N systems (see Fig. 4.3). Fig. 4.3(a) shows the stable metal nitride class in which a tie-line exists from AlN to a transition metal nitride. Thus, the transition metal nitride is stable on AlN at the given conditions, whereas the pure transition metal in contact with AlN and N₂ at this condition will react with the N₂ gas to ultimately form the stable transition metal nitride. In the stable metal class (see Fig. 4.3(b)), there is a tie-line between the transition metal and AlN. This implies that the transition metal, AlN and N₂ are in equilibrium at the given condition, i.e., the transition metal is stable on AlN. Fig. 4.3(c) defines the stable metal aluminide class. The tie-lines from a transition metal

aluminide to AlN and N₂ show that in this class the transition metal aluminide is in equilibrium with AlN and N₂ at the specific nitrogen partial pressure.

To select candidates for stable contacts to AlGa_{1-x}N_x, phases that are predicted to be stable on both GaN and AlN are identified. It was found that a number of phases are stable on both GaN and AlN at 873 K and 1 atm nitrogen pressure and are thus estimated to be stable on AlGa_{1-x}N_x. These phases are elemental Re and nitrides of Sc, Ti, V, Cr, Y, Zr, Mo, La, and Hf (see Fig. 4.4).

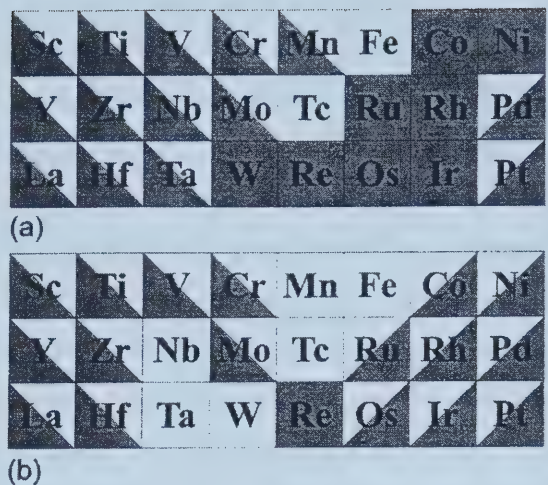


Figure 4.4 Predicted classes at $T = 873\text{ K}$ and $p_{N_2} = 1\text{ atm}$ in (a) Transition metal-Al-N and (b) Transition metal-Ga-N systems. Please note the type of triangle used for e.g., Pd indicates a system belonging to the stable metal aluminide class in (a), whereas it denotes a system in the metal gallide class in (b).^[53]

From the above results, we can see that the low electronic work functions of the equilibrium nitrides (e.g., TiN (2.92 eV), ZrN (2.92 eV), and VN (3.56 eV)) may make it possible to form ohmic contacts to n-AlGa_{1-x}N_x with a high Al fraction. If a pure metal is utilized, some reaction may have to take place between the metal and semiconductor before a very low contact resistance is achieved.

4.2.2 Published data on ohmic contacts to n-AlGa_{1-x}N_x/GaN

Similar to n-GaN, Ti/Al-based ohmic contacts have become the standard metallization schemes for n-AlGa_{1-x}N_x/GaN HFET structures.

4.2.2.1 Al/Ti/n-AlGaIn/GaN

Liu *et al.*^[56] developed Ti/Al ohmic contacts for n-Al_{0.15}GaN_{0.85}/GaN. The sheet charge-mobility product ($n_s\mu$) of AlGaIn/GaN layers was $0.82 \times 10^{16} \text{ (V s)}^{-1}$. After RIE and pre-deposition cleaning, 30 nm Ti and then 71 nm Al were deposited onto the HFET samples. The thickness ratio of Ti to Al was such that the top Al layer would be consumed by reacting with Ti to form a Al₃Ti layer at low temperatures ($\sim 250^\circ\text{C}$) with excess remaining Ti in contact with the nitride layer. The layer structure was expected to be Al₃Ti/Ti/AlGaIn after annealing. In order to obtain ohmic behavior, the samples were annealed in N₂ at 600-950°C. The lowest specific contact resistance was $3.2 \times 10^{-6} \Omega \text{ cm}^2$ for samples annealed at 950°C in N₂. It was found that ohmic contact formation was related to the low work function of the Ti contacting layer and the formation of a TiN phase at the Ti/nitride interface. The Ti/Al bilayer contact scheme is superior to the Ti only contact due to a surface Al₃Ti layer in the bilayer contact, which might reduce the oxidation problem when annealed in N₂ at high temperature. Preannealing the HFET samples at 850°C prior to metal deposition for 1 h in N₂ appeared to improve the ohmic contact, but the mechanism was unknown.

Qiao *et al.*^[9] developed the so-called “advancing” Al/Ti metallizations to n-Al_{0.22}Ga_{0.78}N/GaN. An Al(20 nm)/Ti(150 nm) bilayer structure was deposited on the n-AlGaIn/GaN layer with direct Si implantation (a peak concentration of about $6.2 \times 10^{20} \text{ cm}^{-3}$). The best specific contact resistance of $5.6 \times 10^{-6} \Omega \text{ cm}^2$ was achieved after annealing at 950°C for 80 s. The authors believed that with the thicker Ti layer consuming nearly all the top AlGaIn layers, the charge carriers could easily access the GaN layer underneath. The drastic decrease in contact resistance R_c was due to the reduction in sheet resistance R_s caused by the Si implantation and the reduction in the specific contact resistance r_c caused by the advancing metallization scheme. The authors proposed that Al and Ti reacted to form Ti₃Al (not Al₃Ti as in the conventional scheme), leaving 85 nm of Ti in excess to fully react with the AlGaIn layer to form AlTi₂N.

4.2.2.2 Au/Ti/Al/Ti/n-AlGaN/GaN

Chu *et al.*^[13] developed Ti/Al/Ti/Au ohmic contacts for high speed high power Al_{0.3}Ga_{0.7}N/GaN HFETs. Ti/Al/Ti/Au (20/100/45/55 nm) multilayers were deposited on the HFET surface. 800°C was chosen instead of the usual annealing temperature of 900°C in order to minimize any surface damage induced during annealing. The minimum specific contact resistance was $3.44 \times 10^{-6} \Omega \text{ cm}^2$.

4.2.2.3 Au/Ti/Al/Pd/n-AlGaN/GaN

Chu *et al.*^[13] also developed Pd/Al/Ti/Au ohmic contacts. The same metallization process was utilized except that Pd (20 nm) was substituted for the first Ti layer. Although a lower specific contact resistance of $5.95 \times 10^{-7} \Omega \text{ cm}^2$ was obtained after annealing at 800°C, the adhesion of contact metals to the nitride surface was unacceptable.

4.2.2.4 Au/Ni/Al/Ti/n-AlGaN/GaN

In developing high-transconductance, self-aligned Al_{0.35}Ga_{0.65}N/GaN modulation-doped field-effect transistors (MODFET), Chen *et al.* utilized a Ti/Al/Ni/Au (20/200/40/40 nm) metallization scheme for ohmic contacts. After annealing at 830°C for 30 s, a specific contact resistance as low as $7.7 \times 10^{-6} \Omega \text{ cm}^2$ was obtained.

Bright *et al.*^[8] developed the same metallization scheme with different layer thicknesses. The lowest specific contact resistance was $2.8 \times 10^{-6} \Omega \text{ cm}^2$ for Al_{0.24}Ga_{0.76}N/GaN after the samples were annealed at 700°C for 60 s in flowing Ar.

4.2.2.5 Ta-based ohmic contact to n-AlGaIn/GaN

One drawback of the Ti/Al “advancing” scheme is that a capping layer is required for ohmic contact annealing since Ti is too reactive and is easily oxidized when annealing is performed in pure N₂ or even in forming gas. In addition, the atomic number of Al and Ti are too low to yield efficient backscattered electron emission for e-beam lithographic alignment purposes. Qiao *et al.*^[12] studied Ta-based interface ohmic contacts to n-Al_{0.24}Ga_{0.76}N/GaN HFET. A multilayer Ta/Ti/Al (50/50/50 nm) metallization was deposited on the HFET surface. After annealing at 950°C for 40 s, the lowest specific contact resistance was $5 \times 10^{-7} \Omega \text{ cm}^2$. HREM imaging showed that a layer of TaN had formed at the metal-nitride interface.

4.2.2.6 NiAl/n-AlGaIn/GaN

The intermetallic compound NiAl (50:50 at. %) is an excellent candidate for high temperature use, as it is stable to extremely high temperatures due to its melting point of 1638°C and its oxidation resistance. Binary and ternary phase diagram information indicates that the Ni-Al-Ga-N system meets the criteria for participating in an exchange reaction. During this exchange reaction, one element in the metal phase exchanges with another element in the semiconductor without the formation of new phases. In the case of NiAl on GaN and AlGaIn, there should be an exchange of Al (from the metal) for Ga (from the semiconductor). The kinetic model of this reaction predicts that the Ga will diffuse throughout the metal film and an Al_xGa_{1-x}N interface should be formed. It is proposed that the formation of this interface will behave in the same manner as the interface (TiN, Al or AlTi₂N) produced by the annealed Ti/Al contacts, resulting in a highly n-type doped interface and a low resistance ohmic contact. A 120 nm NiAl (50:50 at. %) film was deposited on n-Al_{0.12}Ga_{0.88}N ($2.4 \times 10^{18} \text{ cm}^{-3}$) and n-Al_{0.18}Ga_{0.82}N ($2.7 \times 10^{18} \text{ cm}^{-3}$) by radio frequency sputter deposition from a single compound target.^[60] After annealing at 900°C for 5 min, specific contact resistances of $2.1 \times 10^{-5} \Omega \text{ cm}^2$ and $4.7 \times 10^{-5} \Omega \text{ cm}^2$ were obtained, respectively. The Ni/Al contacts seemed to be less

affected than the more commonly used Ti/Al contacts by increasing the atomic percent of Al in the n-AlGa_N. Additionally, long-term thermal annealing at 600°C for 100 h showed that the NiAl contact had good thermal stability.

4.2.3 Microstructural analysis

Only a few researchers have done microstructural analysis for ohmic contacts to n-AlGa_N/Ga_N HFET.^[8, 11] Ruvimov *et al.*^[11] investigated Ti/Al (71/30 nm) ohmic contacts to an AlGa_N/Ga_N HFET structure after annealing at 950°C for 80 min. The contact layer contains two sublayers. EDX analysis showed that the composition of the top sublayer is close to Al₃Ti, while the interfacial layer is rich in Ti (with Ti/Al~2). The lattice parameters of the Ti-rich layer evaluated from electron diffraction pattern and a HRTEM image ($a = 0.296 \pm 0.01$ nm, $c = 1.43 \pm 0.03$ nm) were close to the hexagonal AlTi₂N phase ($a = 0.299$ nm, $c = 1.361$ nm). The orientation relationship between the AlTi₂N phase and the AlGa_N phase was found to be: $(0001)_{\text{AlTi}_2\text{N}} // (0001)_{\text{AlGa}_N}$, $(11\bar{2}0)_{\text{AlTi}_2\text{N}} // (11\bar{2}0)_{\text{AlGa}_N}$. Based on their observations, the authors suggested the following scenario for solid state reactions in Al/Ti contacts to AlGa_N during annealing. The reaction first started between Al and Ti at rather low temperatures (in the range of 250-300°C) with the formation presumably of the Al₃Ti phase as expected according to the binary Al-Ti phase diagram. If Al₃Ti is the only and final product, formation of an Al₃Ti layer from individual Al and Ti layers requires the Al/Ti thickness ratio to be equal to 2.82, taking into account the densities of Ti and Al metals. The reaction of Ti with AlGa_N, which started probably above 400°C, resulted, first, in the dissolution of the native oxide from the AlGa_N surface and, then, in the outdiffusion of N and the formation of the Ti-Al-N interfacial phase. Decomposition of AlGa_N that occurred at higher temperatures (above 850°C) led to the formation of the AlTi₂N phase at the interface. Partial decomposition of the AlGa_N resulted in the outdiffusion of Ga and, sometimes, in the formation of small pockets at the interface, especially at higher temperatures and longer annealing time. Those pockets and

the interface roughness, associated with them, may have been responsible for the increase in contact resistance.

Bright *et al.*^[8] performed microstructural analysis for Au/Ni/Al/Ti (50/40/220/15 nm) ohmic contacts to AlGaIn/GaN annealed in Ar for 60 s at temperatures in the range 550-900°C. It was found that accompanying the lowest specific contact resistance, which occurred after annealing at 700°C, a three layer structure with Ti, Au and Ni rich layers formed. The Au had apparently diffused through the Ni layer, so that the Ni and Au layers had effectively swapped places. The top layer appeared to be NiAl and the thick middle layer Al₂Au. The near-interface Ti-rich layer seemed to result from the complete consumption of the Ti to form an intermetallic, and diffraction patterns from this phase were consistent with TiAl. However, energy-filtered TEM (EFTEM) showed that this layer had a high Au content. The AlGaIn had not been significantly consumed, and the thin interfacial layer at the metal/AlGaIn boundary was clearly visible. Both α -AlN and TiN were identified in the interfacial layer by HRTEM. Au was also detectable in this interfacial layer. The authors assumed that penetration of Au to the AlGaIn interface was not detrimental to the contact, and may have been helpful.

5. EXPERIMENTAL METHODS

5.1 Experimental materials

The samples studied were fabricated at the Institute for Microstructural Sciences, National Research Council (NRC).

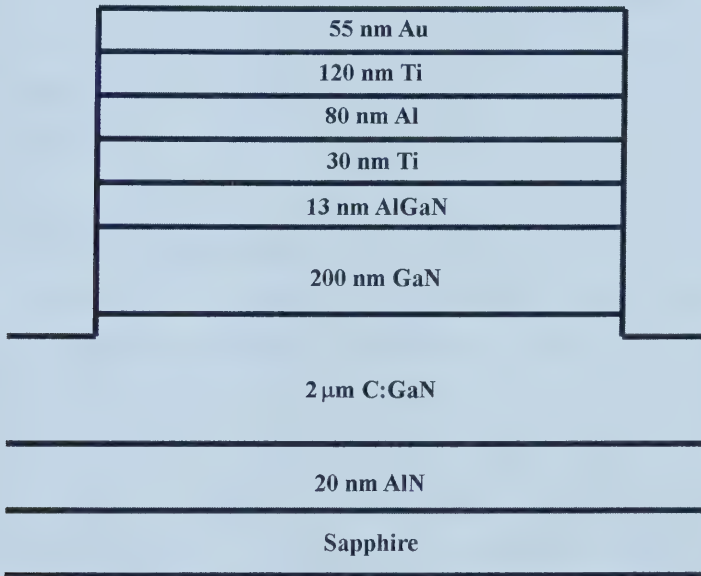


Figure 5.1 Schematic structure of the metallized AlGaIn/GaN HFET.

The thin film growth process utilized a molecular-beam epitaxy/magnetron sputter epitaxy (MBE/MSE) dual-mode system.^[61] The layer structure of the HFET grown is illustrated in Fig. 5.1. Two-inch sapphire wafers were back coated with molybdenum to facilitate radiation heating as indium-free substrate mounting was employed. The sapphire substrate was degreased in chloroform for 15 min, dipped in HF:H₂O (1:10) for 1 min, and rinsed in deionized (DI) water for 10 min before being dried and loaded into the growth system. Nitridation of the sapphire surface was performed at 1000°C and 100 sccm (standard centimeter cube per minute) ammonia. The growth sequence was as

follows. First, a 20-nm AlN nucleation layer was deposited at 880°C by MSE under 40 sccm Ar and 15 sccm ammonia. Then, a 2- μm -thick, C-doped GaN layer was grown at 910°C by MBE using 50 sccm ammonia and a 950 V anode voltage with a methane flow of 1 sccm. This was followed by 200 nm of undoped GaN and 13 nm of AlGaIn using the same growth parameters of temperature and ammonia flow rate. The growth rate for the C-doped GaN was 1 $\mu\text{m}/\text{h}$. X-ray diffraction measurements showed that the AlGaIn had an Al mole fraction of about 0.2, i.e., $\text{Al}_{0.2}\text{Ga}_{0.8}\text{N}$. The central one-third was doped with Si (δ -doping). The doping density was unknown, but it was likely high. Delta doping is so named because its density-vs.-depth characteristic is reminiscent of the Dirac δ function (impulse function). The dopant is concentrated in a very thin layer (preferably, a single atomic layer). Before metallization, samples were cleaned with soap, DI water, acetone, methylethylketone, acetone, isopropyl alcohol and DI water, dipped in $\text{H}_2\text{SO}_4:\text{HNO}_3:\text{H}_2\text{O}$ (1:1:1), rinsed in DI water again, and then blown dry. After that, the samples were descummed and given a dip in 1:10 $\text{NH}_4\text{OH}:\text{H}_2\text{O}$ for 30 s with a final rinse in DI water. Samples for TEM analysis were metallized with a blanket multi-layer structure of Ti (30 nm)/Al (80 nm)/Ti (120 nm)/Au (55 nm). The metals were all deposited in the same e-beam evaporation system without breaking vacuum. After metallization, the samples were rapid thermal annealed (RTA) over a range of temperatures, from 400 to 900°C in flowing argon. The target temperature was maintained for 30 s in each case. Transmission line model was utilized to measure the specific contact resistance. The contact resistance decreased significantly as the annealing temperature was increased until 700°C. The specific contact resistance at this temperature was $6.33 \times 10^{-6} \Omega\text{cm}^2$. Further increases in the annealing temperature caused an increase in the contact resistance.

The Ti (30 nm)/Al (80 nm)/Ti (120 nm)/Au (55 nm) multi-layer metallization was selected because of its reported low contact resistance.^[13] Al/Ti metallizations are standard contacts for n-type GaN-based semiconductors. Titanium and aluminum have relatively low work functions, so that they could form ohmic contacts to n-GaN theoretically. However, oxidation of the contact surface results in a higher sheet resistance in the contact. An Au capping layer is utilized to protect the Al/Ti layer from

the oxygen environment. However, Au inward diffusion towards the semiconductor may cause increase in contact resistance. Therefore, a second thicker Ti layer is utilized as the diffusion barrier layer between Au and the Al/Ti layers in order to minimize metal interdiffusion.

5.2 Microstructural characterization

All samples were examined in a JEOL 2010 TEM equipped with a Noran ultra thin window (UTW) energy dispersive x-ray (EDX) detector. Phase identification was achieved by indexing selected area diffraction (SAD) and convergent beam electron diffraction (CBED) patterns, together with semi-quantitative x-ray microanalysis.

5.2.1 TEM sample preparation

Both cross-section and plan view sections were prepared for TEM analysis. Sample preparation is a crucial step of TEM analysis; it may encompass 70% of the TEM time. Successful TEM analysis depends on a good sample preparation method. Generally, the TEM analysis starts with the development of a good and stable sample preparation technique based on both the type of material and the desired information. There are three major problems in preparing GaN-based samples. First of all, sapphire, which is a common substrate material for GaN, is difficult to thin mechanically when thinned below 20 μm due to its high hardness and its mechanical instability. Sapphire has a tendency to crack and chip at thickness below 20 μm . Secondly, since sapphire is very hard, polishing/dimpling times are quite long as are sputtering times. Thirdly, and perhaps more importantly, the three materials, metals, GaN and sapphire, have very different sputtering rates, making it difficult to obtain electron transparent areas of all three regions. However, the key point of ohmic contact formation is the interfaces between various materials. Therefore, it is necessary to develop a method, which can produce TEM samples with both metal and semiconductor electron transparent areas. And this method must be stable, reproducible, and efficient. Several techniques were tried. The

majority of the cross sections were prepared using a dimpling/ion milling process or a modified wedge polishing procedure.^[62] Selected samples were also prepared using focused ion beam (FIB) techniques. Plan view specimens were prepared by polishing and dimpling from the sapphire side followed by single sided ion milling to perforation.

5.2.1.1 Plan view sample preparation

The procedure for plan view specimen preparation included the following steps:

1. 3-mm discs were cut from wafers using an ultrasonic cutter.
2. Discs were glued onto copper slot grids with the metallized surface facing the grid, in order to provide some mechanical strength.
3. Discs were polished from the sapphire side down to a thickness of about 150 μm with progressively finer grit (200, 400, and 600) SiC abrasive paper.
4. The discs were dimpled from the sapphire side to perforation in the center.
5. Final thinning was done by ion milling in a Gatan Duo Mill 600CTMP. Only one Ar^+ ion gun (the upper gun) was used to sputter the sample. Initially, sputtering was done for 30 min at a voltage of 4.5 kV and a current of 0.5 mA, with a tilt angle of 14° . Final sputtering was done for 15 min at 4.0 kV and 0.5 mA, with a tilt angle of 12° .

5.2.1.2 Cross section sample preparation

The majority of the cross sections were prepared using a dimpling/ion milling process or a modified wedge polishing procedure. Selected samples were also prepared using focused ion beam (FIB) techniques.

The dimpling/ion milling process is a standard TEM sample preparation technique. It is described as follows and illustrated in Fig. 5.2.

1. The samples to be examined were cut into 1 mm×5 mm slices. Some Si slices were also cut to the same dimension to be used as filler materials (see Fig. 5.2(a)).

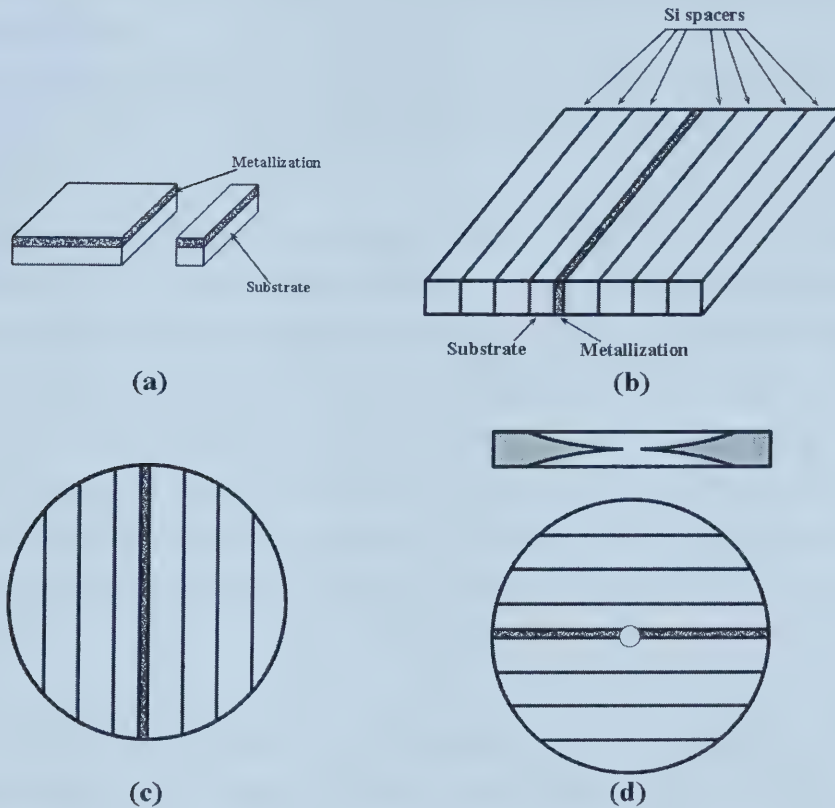


Figure 5.2 Schematic of dimpling/ion milling preparation of TEM cross-section samples. (a) A 1 mm×5 mm slice was cut from wafer. (b) Sample was sandwiched with Si spacers. (c) A 3-mm disc was cut from sandwiched structure. (d) The final look of a sample.

2. One slice of a sample was sandwiched with seven Si slices using a silver-loaded epoxy. Three Si slices were glued on one side of the sample and four Si slices on the other side (see Fig. 5.2(b)).
3. The structure was squeezed gently, to produce thin, bubble free glue layers, using a small vice. Then samples were cured in furnace at 120°C for 15 min.
4. After curing, both sides were polished with progressively finer grit (200, 400, 600) SiC abrasive paper down to a thickness of about 150 μm .
5. A 3-mm disc was cut from the structure using a Gatan ultrasonic disc cutter (see Fig. 5.2(c)).

6. One side of the disc was dimpled to about half the sample thickness, by means of a Gatan Dimple Grinder, with 2-4 μm diamond paste. This side of the disc was then polished with a felt polishing wheel and 1 μm diamond paste to produce a highly reflective surface.
7. The opposite side of the disc was dimpled and polished until either a tiny hole appeared or the Si close to the middle of the Si portion of the disc became optically transparent.
8. Final thinning was done by ion milling in a Gatan Duo Mill 600CTMP. Mounted on a cold stage with a small amount of vacuum grease, the sample was kept cold with liquid nitrogen under a base pressure of $<10^{-6}$ torr. Two Ar^+ guns were employed to sputter the sample. Initially, sputtering was done at a voltage of 5.0 kV and a current of 0.5 mA until the hole extended to the metal layer, with a tilt angle of 15° . Final sputtering was done for 30 min at 4.0 kV and 0.5 mA, with a tilt angle of 10° . The sample was rotated during the sputtering in order to obtain a relative large, thin and flat electron transparent area. Fig. 5.2 (d) shows the final look of the cross-section sample.

The most important advantage of the dimpling/ion milling technique is stability. If operated carefully, a TEM sample with relative large electron transparent areas can be obtained easily. However, this method is very time-consuming. Generally, to prepare a sample requires at least 2-3 days.

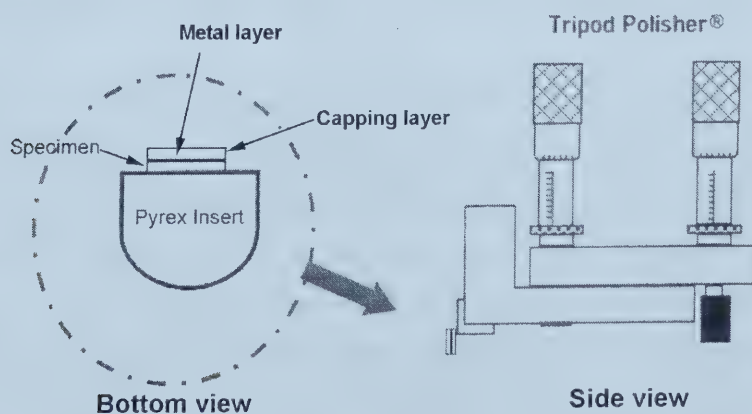


Figure 5.3 Schematic illustration of the specimen-mounting configuration of the Tripod Polisher®.

The procedure of the modified wedge polishing method is described in the following.^[62]
The procedure is modified from that described by Benedict *et al.*^[63]

1. A sample was cut into 2-mm² pieces prior to mounting onto a Pyrex insert of the Tripod Polisher[®] (Fig. 5.3). Before mounting, the specimen was covered with another piece of material with a similar hardness to the specimen. The capping layer protected the specimen from the risk of film delamination during polishing. Acetone soluble, low melting point glycol pthalate wax was used to glue the capping layer to the specimen. The specimen was then mounted onto the edge of the Pyrex insert, using the same wax (Fig. 5.4). If the area of interest for TEM was non-site specific (for this case), multiple specimens could be mounted onto the Pyrex insert to increase specimen throughput.

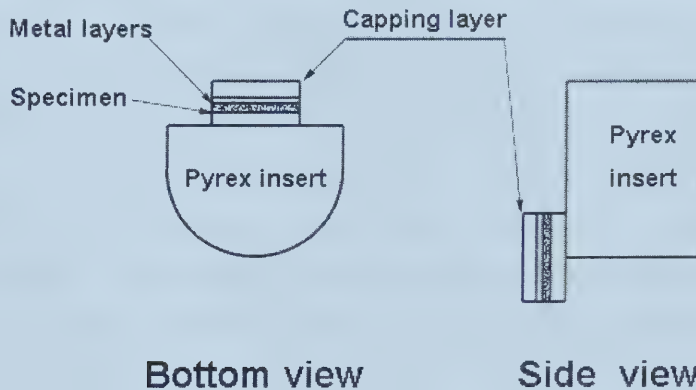


Figure 5.4 Schematic illustration of the specimen-mounting configuration during first side polishing. A capping layer is used to protect the specimen from the risk of delamination.

2. After specimen mounting, the polisher was placed on lapping films and the specimens were wet polished using progressively finer grit diamond lapping films (30, 15, 6, 3, 1 and 0.5 μm , respectively) for coarse polishing. A final polishing using a 0.05- μm colloidal silica solution (CS1) was done on a felt polishing cloth to remove any scratches from the polished surface. After first side polishing, the thickness of specimen was less than 1.5 mm. During second side polishing, the specimen will easily fall off from the Pyrex insert if it is too long. The specimen was removed from the Pyrex insert, and cleaned using acetone.

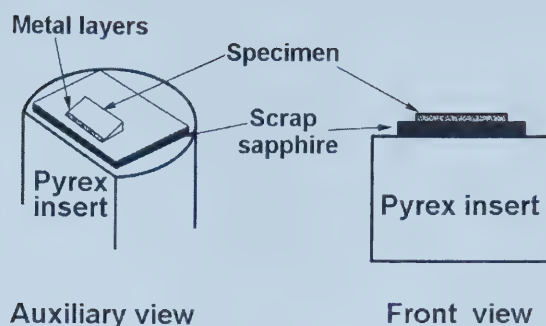


Figure 5.5 Schematic showing the use of a scrap material with hardness close to that of the specimen, to alleviate the tendency for specimen cracking and chipping.

3. For second side polishing, a piece of material with hardness close to that of the specimen, sapphire in this case, was mounted onto the Pyrex insert using epoxy (Fig. 5.5). This piece of material acted as a new substrate onto which the metallized GaN/sapphire was mounted. This alleviated the tendency for the specimen to crack and chip as a result of the large hardness difference between the specimen and the Pyrex insert. The wedge angle was set at about 0.4° . Once the wedge angle was properly set, the surface of the new substrate was cleaned completely, using acetone and ethanol. It is very important to remove any contamination or particles from the mounting surface. The polished surface was attached to the polisher using a small amount of super glueTM. The area containing the metal layers was positioned towards the flattened surface of the Pyrex insert. Enough super glue was used to surround the edges of the specimen to provide some mechanical stability during processing and to protect the specimen from the risk of film delamination.

There are three possible specimen-mounting configurations: parallel mounting, perpendicular mounting, and angular mounting (Fig 5.6). Each orientation has its advantages and shortcomings. Parallel mounting can provide the largest thin area for TEM analysis, but it has the highest risk of polishing away the metal layers. Perpendicular mounting can be used for multiple specimens, increasing specimen throughput and essentially eliminating the risk of polishing metal layers away. However, only very small thin areas of the metal/semiconductor interface are

produced. Angular mounting is essentially a compromise between the first 2 techniques.

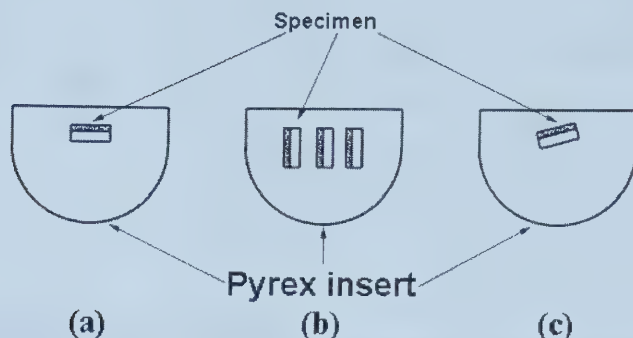


Figure 5.6 Three orientations of specimen mounting during second side wedge polishing are shown. (a) Parallel mounting; (b) Perpendicular mounting; (c) Angular mounting.

After curing of the super glue, the specimens were wet polished to the desired thickness using the same diamond lapping films (and in the same order) as described for first side polishing. During the last three polishing steps (3, 1 and 0.5 μm), the specimen was checked frequently to ensure that it was polished thin enough and the metal layers had not peeled away from the GaN. Since the GaN/sapphire specimen is optically transparent, it is difficult to determine whether the specimen is polished sufficiently. Consequently, the specimen was checked periodically using an optical microscope. A final polishing, as described for first side polishing, was used to remove any scratches from the specimen surface.

4. After final polishing, the specimen was removed from the Pyrex insert and mounted onto a 2×1 mm slotted TEM grid using epoxy. The specimen, was sputtered, from one side only, to improve electron transparency. Initially, sputtering was done for 30 min at a voltage of 4.5 kV and a current of 0.5 mA, with a tilt angle of 12°. Final sputtering was done for 15 min at 4.0 kV and 0.5 mA, with a tilt angle of 10°.

The advantage of the modified wedge polishing procedure is that it is relatively fast, only 4 hours were needed to prepare a sample. However, the reproducibility of this procedure

was relatively low. It is very difficult to control the procedure to obtain a successful TEM cross-section sample.

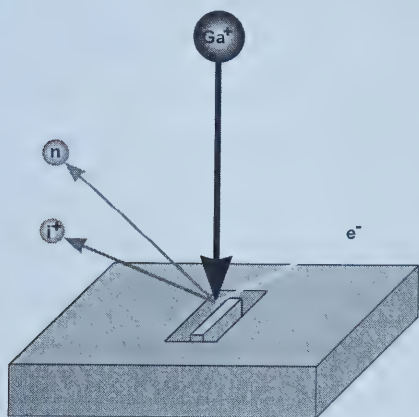


Figure 5.7 Schematic illustration of FIB technique.

Several cross-section samples were also produced, using the focused ion beam technique, by Fibics Incorporated. Focused ion beam milling is the most advanced method for TEM specimen preparation. FIB TEM specimens manufactured by the "Lift-Out" method provide a relatively rapid means of preparing an electron transparent cross-section from a specific site of interest. A bulk sample is inserted into the FIB chamber and a specimen can be

produced directly from the sample's surface at any desired location (see Fig. 5.7). Two trenches are milled using a Ga ion beam on either side of the site of interest. The area in the middle is thinned until it is electron transparent, and then the cross-section is cut free by the focused ion beam. The specimen is then "lifted out" by the use of an electrostatic probe. FIB has the decided advantage of being able to prepare samples with large uniformly thin electron transparent regions as well as being very site specific. Its obvious limitation for many researchers relates to cost, both initial capital expense and operating expenses.

5.2.2 Phase identification

Due to the complexity of the contact metallurgy, phase identification was achieved by indexing selected area diffraction (SAD) and convergent beam electron diffraction (CBED) patterns, together with semi-quantitative x-ray microanalysis. Diffract v1.5b

software, provided by Virtual Laboratories, was used for simulating the diffraction patterns. The procedure for phase identification is described as follows:

1. EDX spectra were obtained from each TEM sample. Several EDX spectra were taken from a given phase. Multiple SAD and CBED (in some cases) patterns were obtained from each phase.
2. Qualitative analysis of EDX spectra showed the elements presented in each phase. Semi-quantitative EDX analysis was utilized to calculate the concentration of each element in the phase. The number of possible phases was narrowed down using available binary and ternary phase diagram.
3. SAD and CBED patterns were indexed manually. Phases were identified by comparing calculations with Joint Committee of Powder Diffraction Standard (JCPDS) data. Diffract v1.5b software was utilized for simulating the diffraction patterns and for confirmation of calculations.
4. Several SAD and CBED patterns from each phase were indexed using the method described in Step 3, in order to verify the results.

5.2.2.1 Selected area diffraction (SAD)

Electron diffraction is a powerful technique to study the microstructure of materials. When the electron beam penetrates the thin foil, a pattern, either ordered spots, rings, or a dim background, will form at the back focal plane of the objective lens. This pattern contains direct crystallographic information about small areas of the specimen. A single crystal diffraction pattern consists of a simple array of bright spots; each spot represents a set of lattice planes with the same d-spacing. A polycrystalline ring diffraction pattern is formed by a large number of small discrete grains, each with exactly the same atomic array, but at different orientations to one another.

Spot and ring SAD patterns were observed with the JOEL 2010 TEM. An aluminum diffraction standard was used to calculate the camera constant.

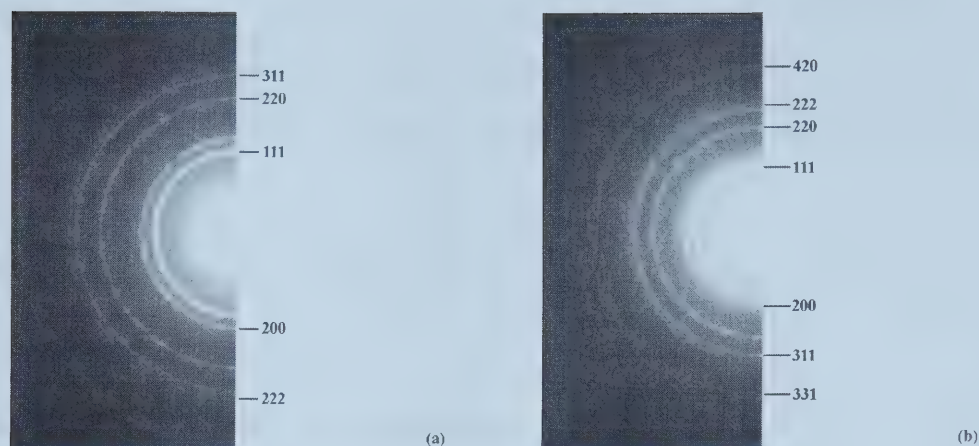


Figure 5.8 Ring diffraction patterns of aluminum diffraction standard sample. (a) Camera length $L=100$ cm. (b) Camera length $L=80$ cm.

Fig. 5.8 shows ring diffraction patterns obtained from aluminum diffraction standard samples. According to these two ring patterns, when the camera length of TEM $L=100$ cm, the camera constant $L\lambda=24.54$ cm-nm; when $L=80$ cm, $L\lambda=1.939$ cm-nm.

5.2.2.2 Convergent beam electron diffraction (CBED)

Although SAD can give useful information about specimen, it has two limitations:^[63]

- The minimum selectable area is limited to regions $\sim 0.2 \mu\text{m}$ in size.
- SAD patterns contain only rather imprecise two-dimensional crystallographic information.

To overcome the above limitations, a convergent beam of electrons is used to limit the region of the specimen, which contributes to the diffraction patterns. In addition to the improved spatial resolution, CBED can provide a wealth of new information not available in SAD, such as specimen thickness, unit cell, precise lattice parameters, crystal system and true 3D crystal symmetry. The major advantage of CBED over all other diffraction techniques is that most of the information is generated from minuscule regions

beyond the reach of other diffraction methods. There are two potential drawbacks of CBED:

- Local contamination that can cause localized stresses.
- The convergent beam may heat or damage the region of the specimen during examination.

CBED patterns were also obtained on the JEOL 2010 TEM.

5.2.2.3 Energy dispersive x-ray spectroscopy (EDX)

When the electron beam strikes a TEM specimen, x-rays are generated from interaction between specimen atoms and the electrons. An x-ray spectrum can be obtained based on x-ray energy. A particular element will emit characteristic x-rays; therefore, the chemical composition of specimen can be determined from the energy dispersive x-ray spectrum.

According to the Cliff-Lorimer ratio technique, quantitative microanalysis of TEM specimen can be done using the following simple equation:

$$\frac{C_A}{C_B} = k_{AB} \frac{I_A}{I_B} \quad (5-1)$$

where C_A and C_B are the weight percents of each element in a binary system AB ; k_{AB} is often termed the Cliff-Lorimer factor and varies according to the TEM system and the accelerating voltage; I_A and I_B are the x-ray counts for each element in the spectrum, respectively.

EDX spectra were obtained using a Noran ultra thin window (UTW) energy dispersive x-ray (EDX) detector mounted on the JOEL 2010 TEM. Peak integration and background subtraction of EDX spectra in semi-quantitative microanalysis were achieved using DTSA v2.0.1 software. Background subtraction was achieved by selecting windows, of the energy width, on either side of the peak of interest. Care was taken to ensure no overlap with any other characteristic peaks. The Cliff-Lorimer “ k ” factors were

determined using a standardless approach. This approach was only able to provide approximate compositions; however, phase identification was still possible when this information was combined with the electron diffraction analysis.

6. RESULTS AND DISCUSSION

6.1 Electrical properties

Table 6.1 lists some electrical properties measured from samples, which were annealed at 700°C for 30s.

Table 6.1 Electrical properties of samples annealed at 700°C for 30s

$R_s (\Omega/)$	$r_c (\Omega \text{ cm}^2)$	$\rho_c (\Omega \text{ cm})$
4.42×10^2	2.24×10^{-5}	0.9961
4.51×10^2	1.52×10^{-5}	0.8274
4.56×10^2	1.26×10^{-5}	0.7593
4.43×10^2	1.17×10^{-5}	0.7194
4.64×10^2	9.39×10^{-6}	0.6599
4.99×10^2	7.19×10^{-6}	0.5987
5.58×10^2	6.33×10^{-6}	0.5943

The top four values of the table are for devices in the center of the 2" wafer, the bottom three for devices at the edge of the 2" wafer. It can be seen that there is a significant change in the contact resistance between the center and the edge of the wafer. The lowest value of the specific contact resistance was $6.33 \times 10^{-6} \Omega \text{ cm}^2$. The specific contact resistances of samples annealed at lower temperature were much higher. Annealing at 750°C caused an increase in the contact resistance, thus 700°C was believed to be the optimal temperature.

6.2 Microstructural characterization

Both cross-section and plan view TEM samples were analyzed for the as-deposited sample and samples annealed at 400°C, 500°C, 600°C, 700°C, and 900°C, respectively. SAD, CBED, and EDX techniques were used for phase identification.

6.2.1 As-deposited

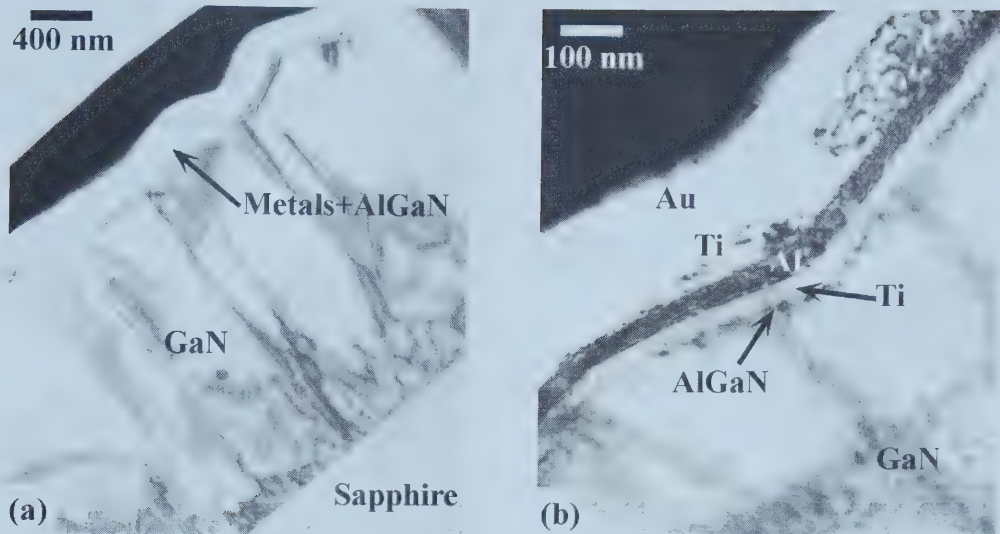


Figure 6.1 TEM bright field images of the as deposited metallization/semiconductor structure at low (a) and high (b) magnification.

The specific contact resistance of the as-deposited sample is too high to satisfy the device requirements. A low magnification image, taken from a FIB section, of the as deposited specimen is shown in Figure 6.1(a). The sapphire substrate, GaN, AlGaIn and the metal layers are visible in the image. The outermost layer (appears dark in the image) is tungsten which was deposited during FIB specimen preparation. The individual metal layers are not distinguishable at low magnification, but the total thickness of the layers corresponds to that reported in the experimental section. The AlGaIn layer thickness was measured, from a higher magnification image (see Fig. 6.1(b)), and was found to be close to the intended 13 nm. EDX spectra and SAD ring patterns (not shown here) indicated that the metal layers were Ti, Al, Ti, and Au, respectively. The measured layer thicknesses were close to the intended values, of 30 nm, 80 nm, 120 nm, and 55 nm for Ti, Al, Ti and Au, respectively. The roughness of the GaN surface is clearly apparent and is of the order of the thickness of the metallization. SAD patterns (not shown) showed that the GaN was [0001] oriented, i.e., the [0001] direction was perpendicular to the GaN surface. The dark streaks in the GaN, perpendicular to the sapphire surface, are misfit

dislocations, which arise because of lattice mismatch between GaN and the AlN buffer layer.

6.2.2 400°C annealing

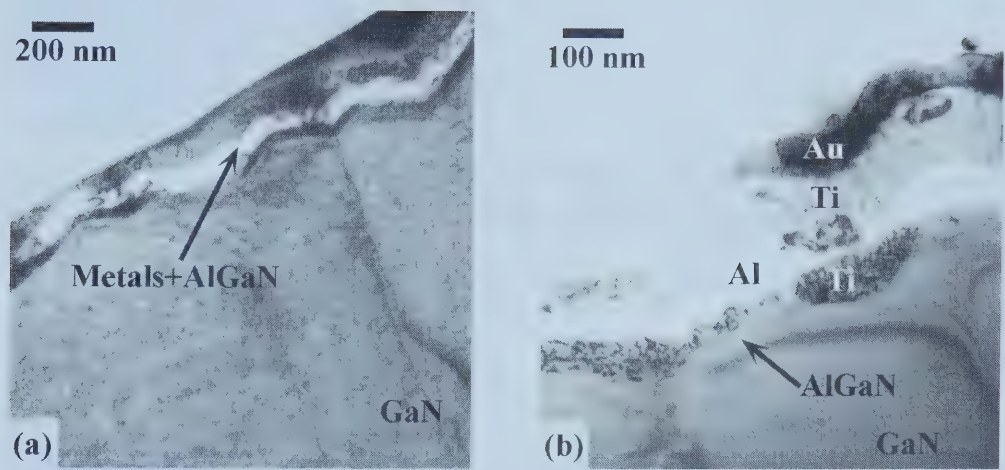


Figure 6.2 TEM bright field images of a sample annealed at 400°C for 30s at low (a) and high (b) magnification.

Table 6.2 Lattice parameters for Ti, Al, Au, and GaN

Phase	Crystal structure	Lattice parameter					
		a (nm)	b (nm)	c (nm)	α	β	γ
Ti	hcp	0.2950	0.2950	0.4686	90°	90°	120°
Al	fcc	0.4049	0.4049	0.4049	90°	90°	90°
Au	fcc	0.4079	0.4079	0.4079	90°	90°	90°
GaN	Wurzite	0.3186	0.3186	0.5178	90°	90°	120°

Bright field images from samples annealed at 400°C for 30s are shown in Fig. 6.2. A low magnification image obtained from a FIB prepared sample is shown in Fig. 6.2(a). Four layers can be seen clearly. Fig. 6.2(b) is a high magnification bright field image, which was obtained from a wedge polished sample. Four distinct layers are visible. EDX analysis showed that these correspond to the original deposited layers of Ti, Al, Ti, Al and Au respectively. It was also found that the grain size of each phase was enlarged due

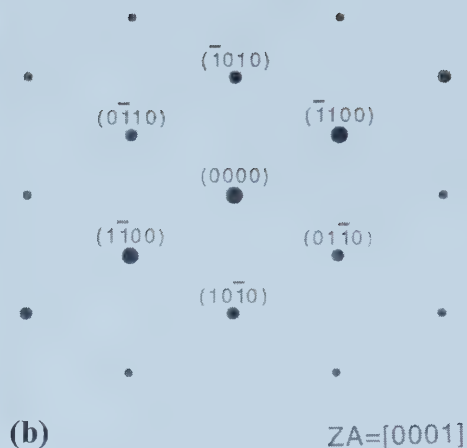
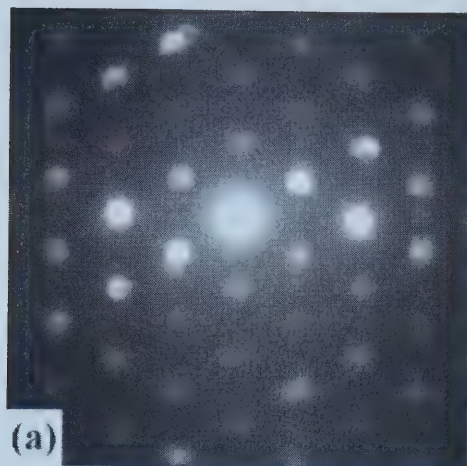


Figure 6.3 SAD spot diffraction pattern (a) obtained from the third (Ti) layer from the semiconductor surface in Fig. 6.2(b), and computer-simulated spot pattern (b).

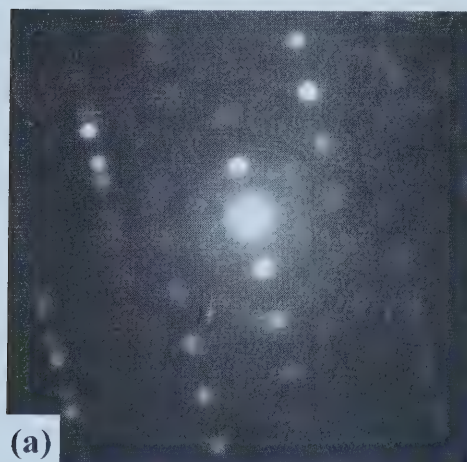


Figure 6.4 SAD spot diffraction pattern (a) obtained from the fourth (Au) layer from the semiconductor layer in Fig. 6.2(b), and computer-simulated spot pattern (b).

to the annealing. Therefore, SAD spot patterns were obtained rather than ring patterns. Table 6.2 lists the lattice parameters for Ti, Al, Au, and GaN. Fig. 6.3(a) shows an SAD diffraction pattern of the third layer from the semiconductor in Fig. 6.2(b); it matched very well with titanium (Fig. 3(b) shows the computer simulated diffraction pattern). Similarly, SAD diffraction patterns from the second (not shown) and fourth (see Fig. 6.4) layers matched with aluminum and gold, respectively. SAD patterns obtained from the GaN layer were used as a calibration standard in order to minimize the systematic error (see Fig. 6.5). A diffraction pattern was not obtained from the innermost layer due to its thin nature. Thickness measurements close to the original as deposited thickness, i.e., 30,

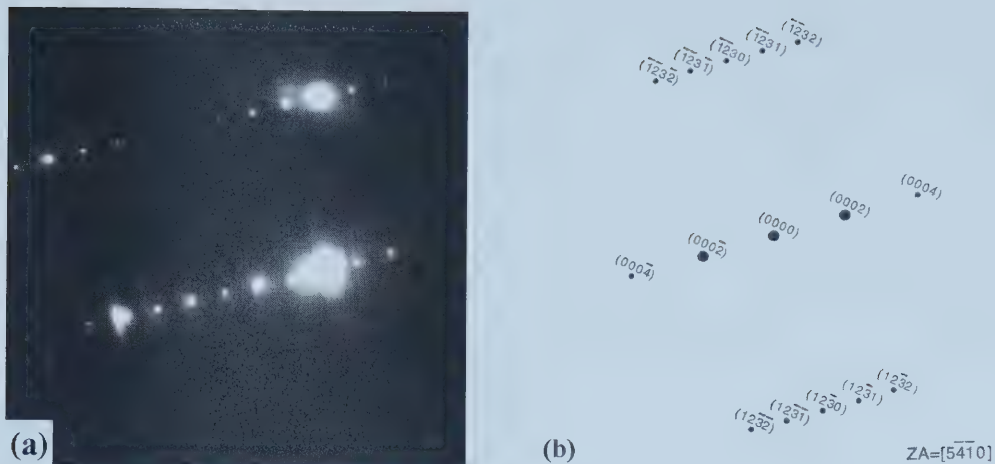


Figure 6.5 SAD spot diffraction pattern (a) obtained from GaN layer in Fig. 6.2(b), and computer-simulated spot pattern (b).

80, 120, and 55 nm, respectively, were obtained. The interfaces between the different metal layers are relatively sharp indicating that no significant interdiffusion has occurred. However, Fig. 6.2(b) shows that some interdiffusion occurred at the interfaces between different metal layers, especially for the two Ti/Al interfaces.

6.2.3 500°C annealing

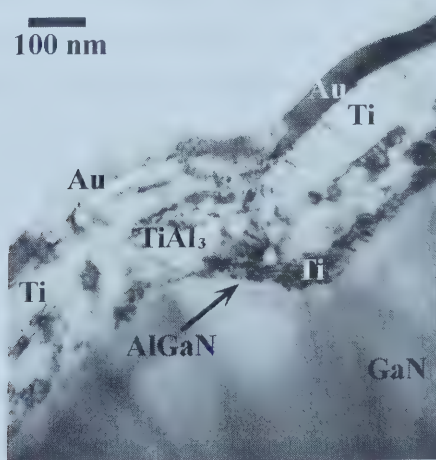


Figure 6.6 TEM bright field image of metallization annealed at 500°C for 30s.

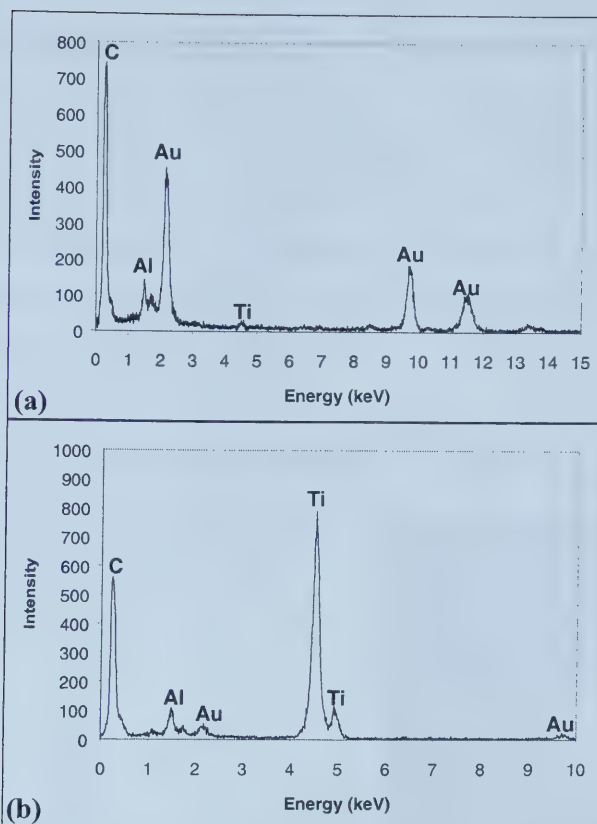
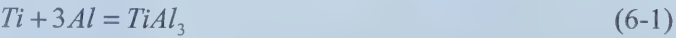


Figure 6.7 EDX spectrum obtained from the outermost dark layer (a) and the bright layer below the Au layer (b) in Fig. 6.6.

The first sign of significant reaction are apparent in samples annealed at 500°C (see Fig. 6.6). The structure of the contact started to change. Measurement from TEM images showed that the thickness of the outermost dark layer still matched the original thickness of Au layer. An EDX spectrum that was obtained from the outermost dark layer shows predominantly Au peaks with a small amount of Al and Ti (Fig. 6.7(a)). The results indicate that the outermost Au layer remained intact with the same morphology; but Al has penetrated the as-deposited second Ti layer and reached Au layer. The EDX spectrum shows that the layer below the Au layer was still Ti with small amount of Al in it (Fig. 6.7(b)), but the thickness measurements show that it had shrunk to around 100 nm. The inner titanium layer (EDX spectrum was not shown here) was no longer continuous. The C peaks in the EDX spectra were due to the electron beam contamination during analysis.

Most of the changes occurred in aluminum layer. EDX analysis showed that aluminum reacted with some of the Ti to form an Al-rich, Al-Ti layer (Fig. 6.8(a)), which was identified through semi-quantitative x-ray analysis and electron diffraction patterns (Fig. 6.8(b)) as $TiAl_3$ (Table 6.3). The following reaction shows that the formation of $TiAl_3$ corresponds to the consumption of approximately 30 nm of the total 150 nm of Ti, assuming consumption of the original 80 nm Al. Apparently, the Al layer has not been consumed completely at 500°C annealing.



$TiAl_3$ formation occurred at both Ti/Al interfaces.

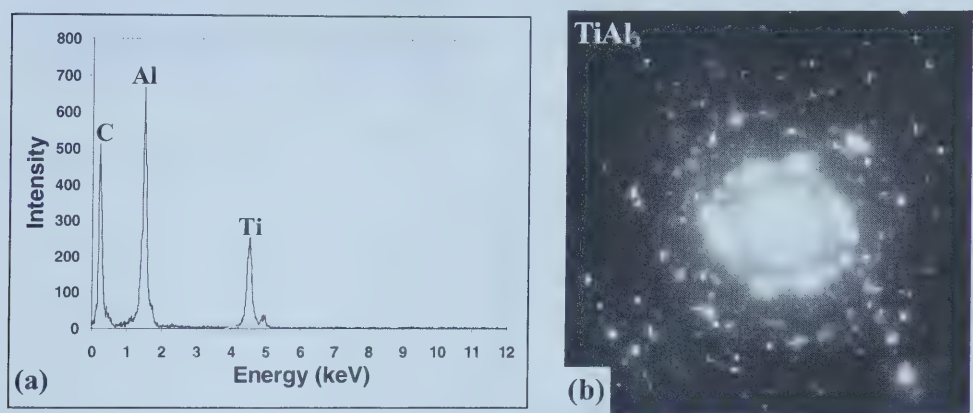


Figure 6.8 EDX spectrum (a) and SAD ring diffraction pattern (b) obtained from the Al-Ti layer in Fig. 6.6.

Table 6.3 Indexing of SAD pattern from Al-Ti layer in Fig. 6.7(b)

Experimental d (nm)	$TiAl_3$ ^[70]		
	d (nm)	h k l	Intensity
0.4316	0.4230	0 0 8	20
0.3936	0.3860	1 0 1	10
0.3237	0.3370	1 0 5	10
0.2695	0.2742	1 1 0	20
0.2400	0.2409	1 0 11	10
0.2343	0.2301	1 1 8	100
0.2050	0.2116	0 0 16	80
0.1984	0.1939	2 0 0	80
0.1597	0.1618	1 0 19	10
0.1447	0.1430	2 0 16	60
0.1177	0.1178	3 1 8	60

6.2.4 600°C annealing

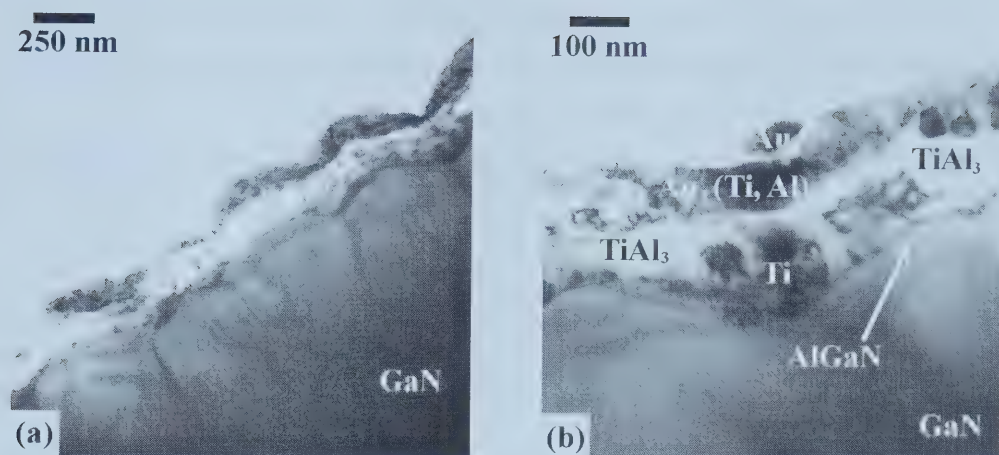


Figure 6.9 TEM bright field images at low (a) and high (b) magnification of sample annealed at 600°C for 30s.

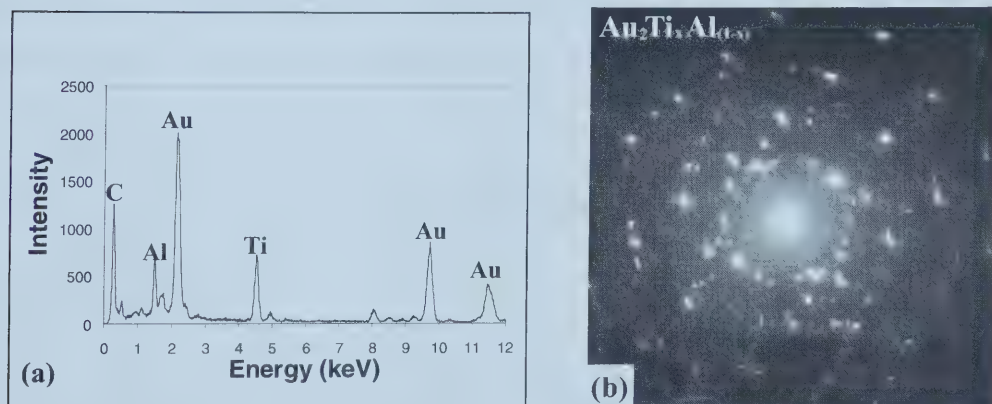


Figure 6.10 EDX spectrum (a) and SAD ring diffraction pattern (b) obtained from the Au-Al-Ti layer in Fig. 6.9.

Further reaction involving the Au layer and some of the remaining Ti and Al occurred on annealing at 600°C (Fig. 6.9). Visual inspection of the contact surface showed a color change from gold to gray, providing additional evidence of Au reaction. Three layers can be seen in the low magnification BF image (Fig. 6.9(a)) instead of the original four-layer structure. A high magnification BF image reveals more details of the structure (Fig. 6.9(b)).

Much of the outermost Au layer has been consumed, with isolated patches still visible. EDX analysis (Fig. 6.10(a)) shows that the outer continuous layer is Au-rich containing Al as well as Ti. Table 6.4 shows results from semi-quantitative EDX analysis.

Table 6.4 Results of semi-quantitative EDX analysis for the Au-Ti-Al layer in samples annealed at 600°C for 30s

Grain	Peak	Intensity	Concentration (wt. %)
1	Au	7137	70
	Ti	5516	16
	Al	3977.5	13
2	Au	14679	74
	Ti	9449	14
	Al	6999	12

The calculated Cliff-Lorimer factors, k_{AuTi} , k_{AlTi} , and k_{AuAl} , were obtained from reference [64]. The results show that the concentration of Au, Ti, and Al, in this alloy layer is about 70-74 wt. %, 14-16 wt. %, and 12-13 wt. %, respectively. There are two known Au-Al-Ti ternary phases, $AlAuTi$ and $AlAu_2Ti$, however, diffraction patterns (e.g., Fig. 6.10(b)) obtained from the layer did not match either of these phases.

Au-Ti

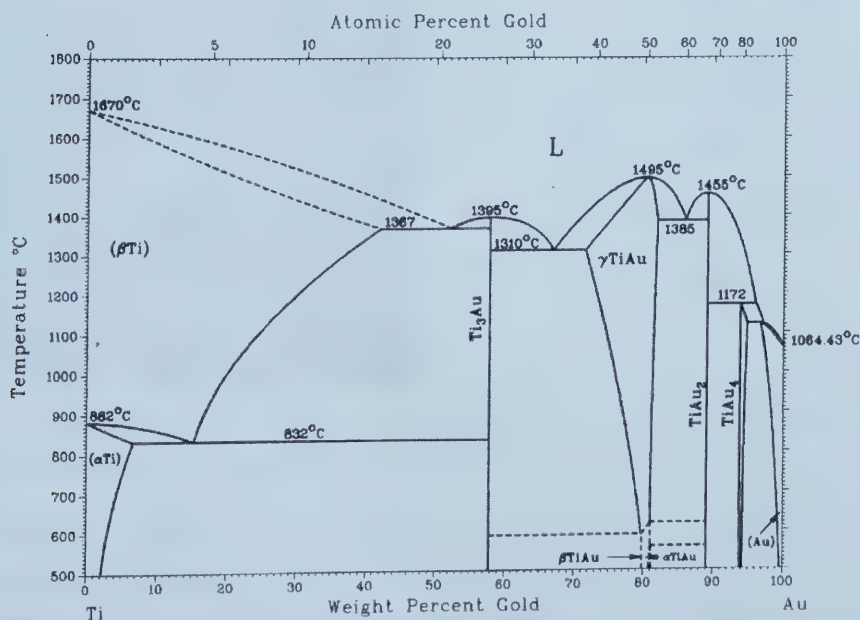


Figure 6.11 Au-Ti binary phase diagram.^[65] It shows that Au can form 6 binary phases with Ti; Ti_3Au , $\gamma TiAu$, $\beta TiAu$, $\alpha TiAu$, $TiAu_2$, and $TiAu_4$.

The Au-Ti binary phase diagram (Fig. 6.11) shows that Au can form 6 binary phases with Ti, AuTi₃, AuTi, Au₂Ti, and Au₄Ti. Table 6.5 lists the Au compositions (weight percent) of these six binary phases.

Table 6.5 Au compositions of binary Ti-Au phases

Phase	Composition (wt. % Au)	Pearson symbol	Space group
AuTi ₃	58	<i>cP</i> 8	<i>Pm</i> $\bar{3}n$
γ AuTi	72-82	<i>cP</i> 2	<i>Pm</i> $\bar{3}m$
β AuTi	80-80.4	<i>oP</i> 4	<i>Pmma</i>
α AuTi	80.4	<i>tP</i> 4	<i>P4/nmm</i>
Au ₂ Ti	89.2	<i>tI</i> 6	<i>I4/mmm</i>
Au ₄ Ti	94-95	<i>tI</i> 10	<i>I/4m</i>

The spots in the diffraction pattern in Fig. 6.10, taken from one of the grains of the Au-rich layer, matched with the Au_2Ti phase (Fig. 6.12). The rings matched the TiAl_3 phase, which is formed between the Au-rich, and Ti layers, and will be explained later. If the Au-rich layer is indeed Au_2Ti , how does one explain the presence of Al? According to the Au-Al binary phase diagram (Fig. 6.13), gold can also form Au_2Al (Table 6.6). More noteworthy, $\gamma\text{-Au}_2\text{Al}$ (which is stable above 569°C) is isostructural with Au_2Ti . Both

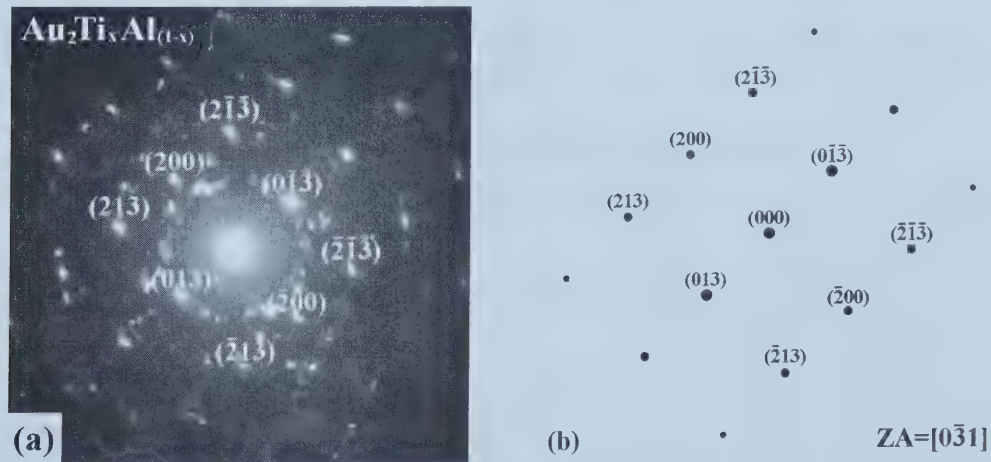


Figure 6.12 SAD pattern (a) from Au-rich layer in Fig. 6.9 and computer-simulated diffraction pattern of Au_2Ti at $[0\bar{3}1]$ zone axis.

phases have a tetragonal structure (Pearson symbol $tI4$ and Space group $I4/mmm$) with similar lattice parameters (Table 6.7). Also considering the errors involved in semi-quantitative EDX analysis, the Au concentration 72 wt. % is not far from 89.2 wt. %,.

which is the Au concentration in Au_2Ti . It is therefore quite conceivable that a pseudobinary phase has formed – $\text{Au}_2(\text{Al}_x\text{Ti}_{1-x})$ – with Ti and Al being mutually soluble.

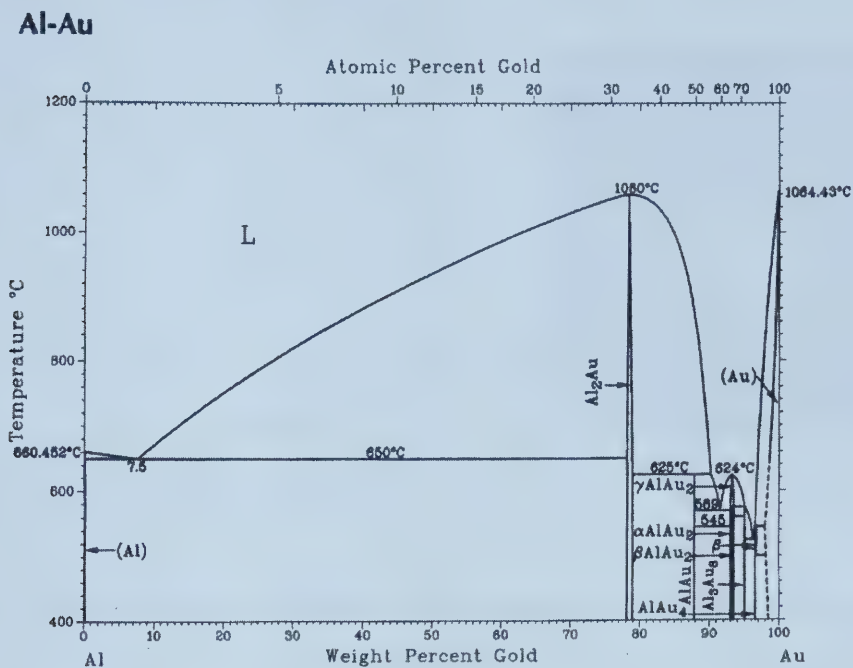


Figure 6.13 Au-Al binary phase diagram.^[65] It shows that Au can form 7 binary phases with Al, Al_2Au , AlAu , γAlAu_2 , βAlAu_2 , αAlAu_2 , Al_3Au_8 and AlAu_4 .

Table 6.6 Au compositions of binary Al-Au phases

Phase	Composition (wt. % Au)	Pearson symbol	Space group
Al_2Au	78-79	<i>cF12</i>	<i>Fm</i> $\bar{3}m$
AlAu	88	<i>mP28</i>	<i>P2</i> ₁ / <i>m</i>
γAlAu_2	93-93.6	<i>tI6</i>	<i>I4/mmm</i>
βAlAu_2	93.2-93.4	<i>oP32</i>	<i>Pnmm</i>
αAlAu_2	93.5-93.6	<i>oP12</i>	<i>Pnma</i>
Al_3Au_8	95.1	<i>hR132</i>	<i>R</i> $\bar{3}c$
AlAu_4	96.7	<i>cP20</i>	<i>P2</i> ₁ <i>3</i>

Table 6.7 Crystal structures of Au_2Ti and $\gamma\text{-Au}_2\text{Al}$ binary phases

Phase	Structure	Lattice parameters (nm)	
Au_2Ti	Tetragonal (I4/mmm)	$a = 0.3429$	$c = 0.8538$
$\gamma\text{-Au}_2\text{Al}$	Tetragonal (I4/mmm)	$a = 0.3349$	$c = 0.8893$

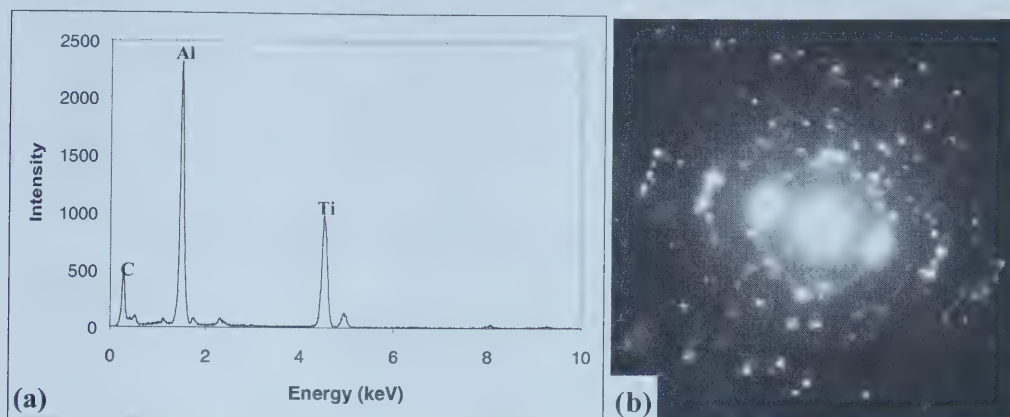


Figure 6.14 EDX spectrum (a) and SAD ring diffraction pattern (b) obtained from the Al-Ti layer in Fig. 6.9.

Table 6.8 Results of semi-quantitative EDX analysis for the Al-Ti layer in samples annealed at 600° for 30s

Grain	Peak	Intensity	Concentration (wt. %)
1	Al	23521.5	66
	Ti	13467.5	34
2	Al	28468	57
	Ti	24518	43

Additional TiAl_3 has formed beneath the $\text{Au}_2(\text{Ti}_x\text{Al}_{1-x})$ layer, consuming more titanium and aluminum. Fig. 6.14 shows an EDX spectrum and SAD pattern obtained from the intermediate layer in Fig. 6.9. The results of semi-quantitative EDX analysis (Table 6.8), which were obtained from two different grains in this layer, give an Al concentration in the range of 57-66 wt. %. The Al-Ti binary phase diagram (see Fig. 6.15)^[65] shows that at 63 wt. % Al, there is an intermetallic phase, TiAl_3 (Table 6.9). TiAl_3 has a tetragonal structure, with lattice parameters $a=0.3854$ nm and $b=0.8584$ nm. The SAD pattern (in Fig. 6.14(b)) matched reasonably well with TiAl_3 (Table 6.10).

Table 6.9 Al compositions of binary Al-Ti phases

Phase	Composition (wt. % Al)	Pearson symbol	Space group
Ti ₃ Al	14-26	<i>hP8</i>	<i>P6₃/mmc</i>
TiAl	34-56.2	<i>tP4</i>	<i>P4/mmm</i>
Ti ₃ Al ₅ (a)	44-49	<i>tP32</i>	<i>I4/mbm</i>
TiAl ₂	51-54	<i>tI24</i>	<i>I4₁/amd</i>
αTiAl ₂ (b)		<i>oC12</i>	<i>Cmmm</i>
TiAl ₃	63	<i>tI8</i>	<i>I4/mmm</i>
αTiAl ₂	63		

Table 6.10 Indexing of SAD pattern from Al-Ti layer in Fig. 6.9(b)

Experimental d (nm)	TiAl ₃ ^[70]		
	d (nm)	h k l	Intensity
0.3775	0.3860	1 0 1	10
0.3664	0.3670	1 0 3	10
0.2682	0.2742	1 1 0	20
0.2237	0.2301	1 1 8	100
0.2003	0.1939	2 0 0	80
0.1726	0.1713	2 1 3	10
0.1469	0.1430	2 0 16	60
0.1230	0.1225	1 1 24	60
0.1200	0.1178	3 1 8	60

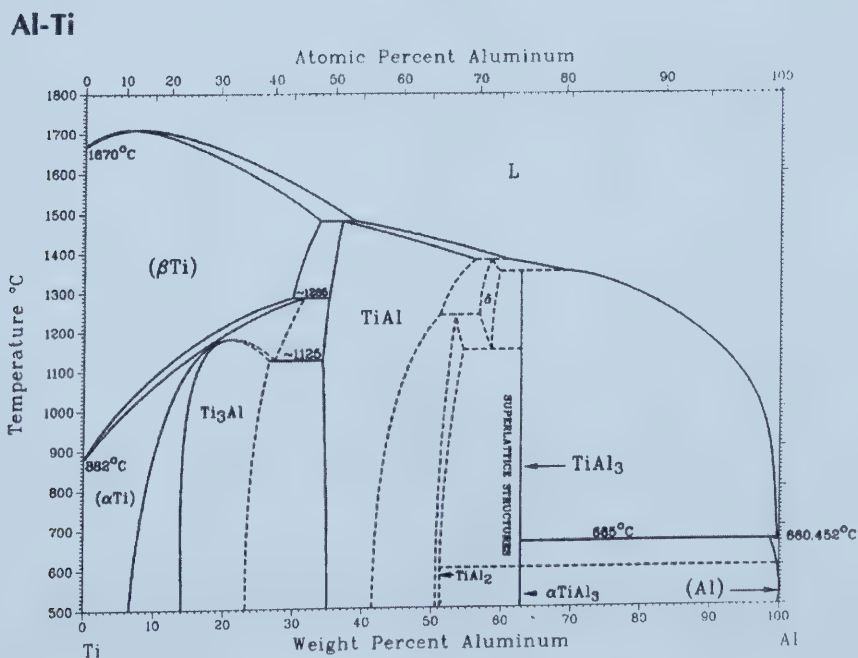


Figure 6.15 Al-Ti binary phase diagram.^[65]

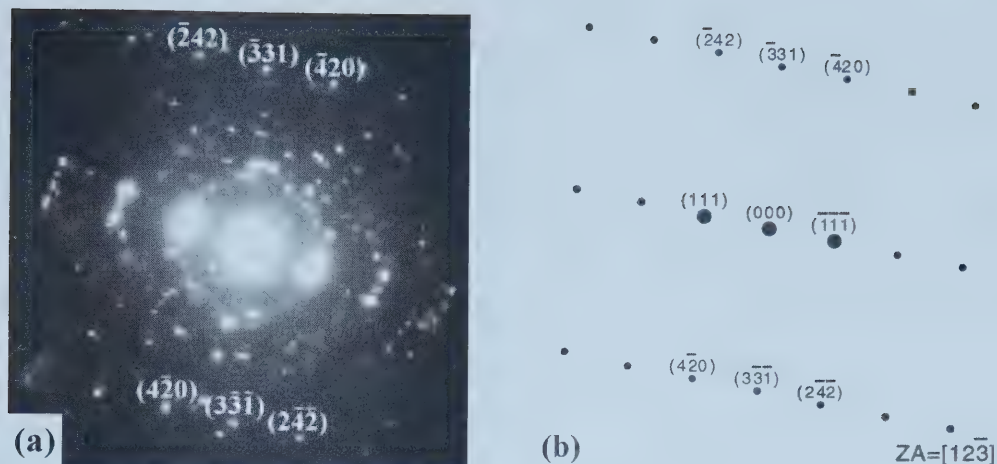


Figure 6.16 SAD pattern (a) from the Al-Ti layer in Fig. 6.9 and computer-simulated diffraction pattern of Al at $[12\bar{3}]$ zone axis.

The SAD ring pattern also shows a row of strongly diffracted spots (Fig. 6.16). These spots matched Al near a $[12\bar{3}]$ zone axis. This indicates that Al has not been completely consumed at 600°C.

Therefore, the following reaction is proposed for annealing at 600°C:

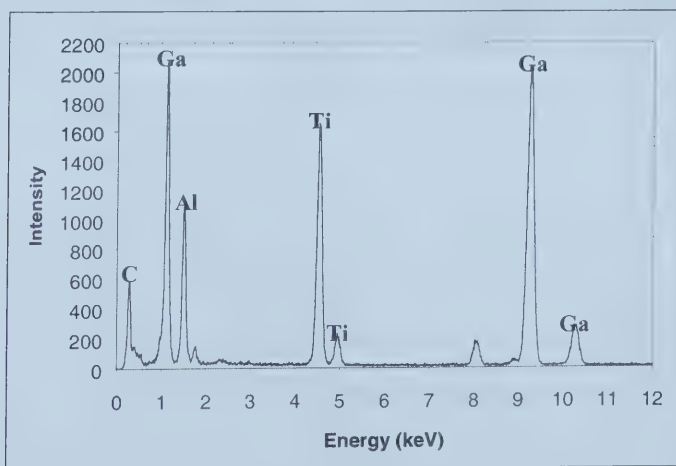
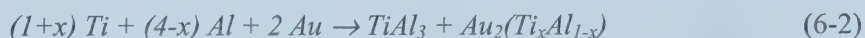


Figure 6.17 EDX spectrum obtained from the contact/AlGaN interface in Fig. 6.9.

Although much of the inner Ti layer has reacted to form TiAl_3 , several patches of Ti remain at the contact/AlGaIn interface. Fig. 6.17 shows an EDX spectrum obtained from the contact/AlGaIn interface. It shows gallium, aluminum and titanium peaks. It is believed that the Ti peaks come from unreacted inner Ti layer, Ga and Al peaks come from the AlGaIn as well as the GaN. The Ti/AlGaIn interfacial region could not be conclusively analyzed, because of its thin nature (<10 nm) and the limited spatial resolution of the TEM employed.

6.2.5 700°C annealing

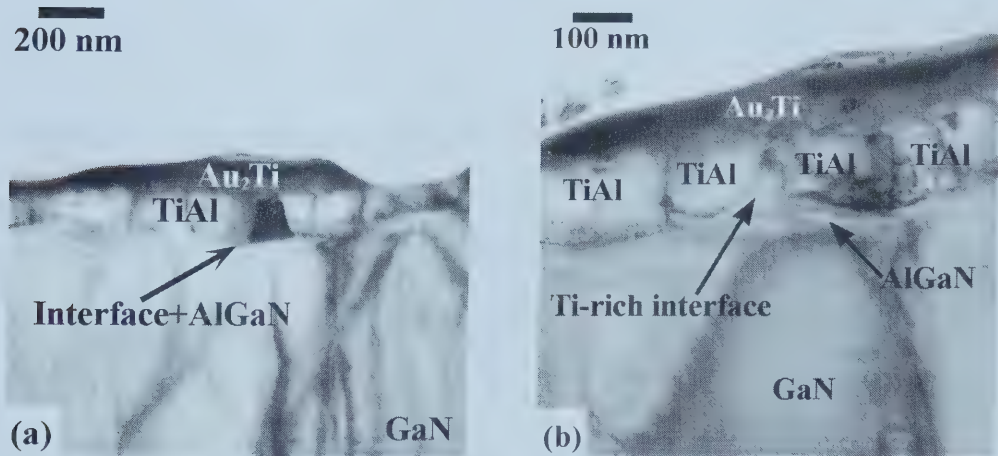


Figure 6.18 TEM bright field images at low (a) and high (b) magnification of sample annealed at 700°C for 30s.

After annealing at 700°C for 30s, the contact attained the lowest specific contact resistance of $6.33 \times 10^{-6} \Omega \text{ cm}^2$. Annealing below or above this temperature resulted in higher contact resistances. Two bright field TEM images of samples annealed at 700°C for 30s are shown in Fig. 6.18 at low and high magnification. These were obtained from FIB prepared samples. The metallization at this point is made up of two prominent layers rather than the three layers present in samples annealed at 600°C.

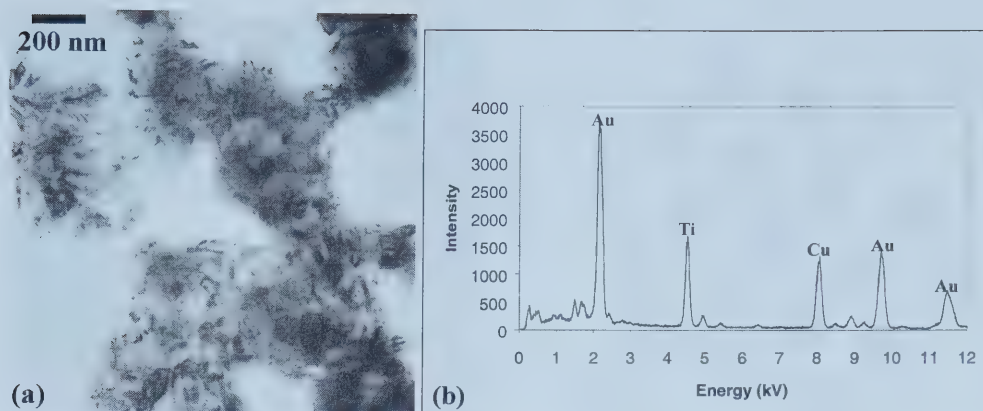


Figure 6.19 (a) TEM plan view image of outer Au-rich layer in Fig. 6.18, and (b) EDX spectrum obtained from (a).

Table 6.11 Results of semi-quantitative EDX analysis for the Au-Ti phase in the plan view specimen (Fig. 6.19)

Grain	Peak	Intensity	Concentration (wt. %)
1	Au	13772	80
	Ti	11386	20
2	Au	20127	81
	Ti	15631	19

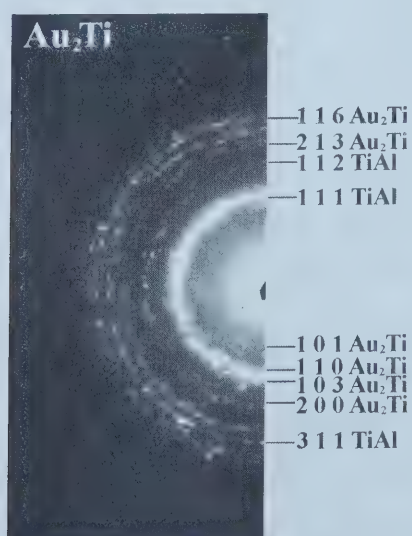


Figure 6.20 SAD ring pattern obtained from several grains in plan view specimen in Fig. 6.19(a). Indexing shows that the rings match Au_2Ti and TiAl phases.

Au₄Ti. An SAD pattern (Fig. 6.20) was obtained from several grains in the plan view specimen. The rings matched very well with both Au₂Ti and TiAl phases (Table 6.12). CBED patterns (e.g., Fig. 6.21) were also obtained from individual grains in the plan view specimen. Indexing of the patterns shows a good match with Au₂Ti phase. Therefore, the outermost Au-rich dark layer in Fig. 6.18 is Au₂Ti. The TiAl rings in SAD ring pattern were from the layer underneath the outermost layer, and will be explained later.

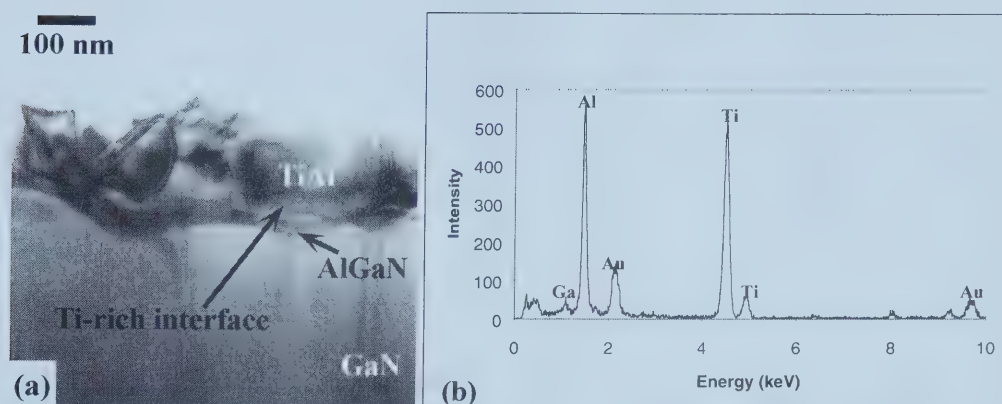


Figure 6.22 TEM bright field image (a) of a sample annealed at 700°C for 30s, which was prepared by wedge polishing method. (b) is the EDX spectrum obtained from the first layer in the image.

In order to perform further study of the samples annealed at 700°C for 30s, TEM cross-section specimens were also prepared by wedge polishing. Fig. 6.22 shows a bright field image obtained from a successful wedge polished cross-section specimen. The outermost Au₂Ti layer has been polished or sputtered away. However, several grains in the middle layer can be seen clearly. EDX spectra (e.g., Fig. 6.22(b)) obtained from several grains in this layer indicate that the middle layer is Ti-Al rich, similar to the second layer in the sample annealed at 500-600°C for 30s. However, the Al/Ti ratio is different. The aluminum concentration is lower than in the lower temperature annealed samples. Semi-quantitative EDX analysis of several grains gave an Al/Ti weight ratio 0.75-1.63 (Table 6.13). The Al-Ti binary phase diagram (see Fig. 6.15) shows that a TiAl phase is formed when the Al/Ti weight ratio ranges from 0.52-1.28.

Table 6.13 Results of semi-quantitative EDX analysis for the Al-Ti layer in samples annealed at 700°C for 30s

Grain	Peak	Intensity	Al/Ti weight ratio
1	Al	5649.5	0.85
	Ti	7023.5	
2	Al	5760	1.5
	Ti	4165	
3	Al	3431	0.85
	Ti	4330	
4	Al	3083.5	0.85
	Ti	3980.5	
5	Al	6097.5	1.33
	Ti	5006.5	
6	Al	5440	1.63
	Ti	3667	
7	Al	6420.5	0.92
	Ti	7400	
8	Al	4673.5	0.75
	Ti	6810	

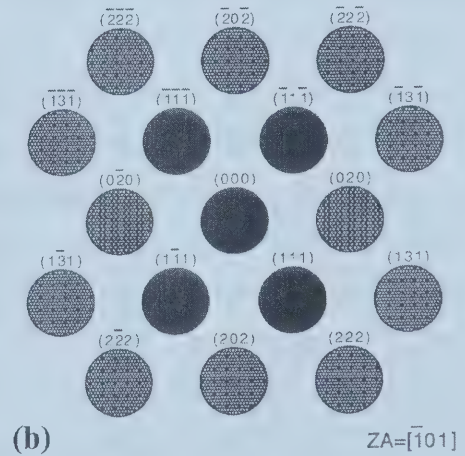
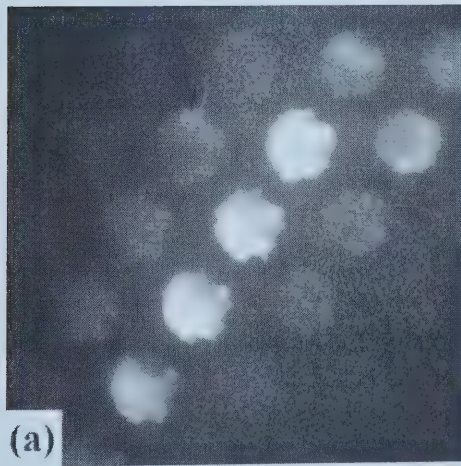


Figure 6.23 CBED pattern (a) from one grain in the Ti-Al rich layer in Fig. 6.22(a) and computer-simulated diffraction pattern of TiAl at $[\bar{1}01]$ zone axis.

The grains in this Al-Ti rich layer are of sufficient size (>100 nm in diameter) to obtain CBED patterns; one example is shown in Fig. 6.23(a). Indexing of CBED patterns indicates that they match the TiAl phase very well. This confirms the EDX results that TiAl (tetragonal, $a = 0.3976$ nm and $c = 0.4049$ nm) has formed replacing Al_3Ti .

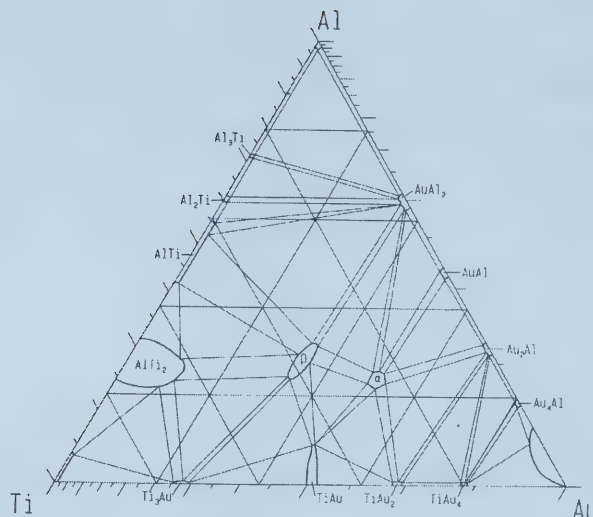
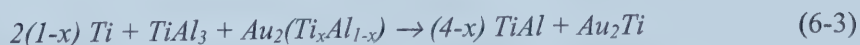


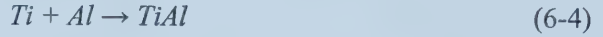
Figure 6.24 Al-Au-Ti ternary phase diagram at 500°C, it shows a solubility limit for Au in TiAl to be <2 at. %^[66].

The EDX spectra from TiAl also show that a significant amount of Au as well as a small amount of Ga are present in TiAl layer (Fig. 6.22(b)). These are apparently due to Ga outward diffusion towards the surface and Au inward diffusion towards the metallization/semiconductor interface. An isothermal section of Ti-Al-Au ternary system^[66] is shown in Fig. 6.24. According to the diagram, the solubility limit for Au in TiAl is <2 at %, much lower than the observed gold level. Moreover, the Ti-Al-Au ternary phase diagram also has two ternary phases, AlAuTi (hexagonal, $a = 0.4407$ nm and $c = 0.5829$ nm) and AlAu₂Ti (cubic, $a = 0.3198$ nm). The gold concentrations in AlAuTi and AlAu₂Ti are about 71-74 wt. % and 84.6-85 wt. %, respectively, much higher than the observed gold level. The CBED patterns did not match any of these two ternary phases. The presence of Au in the TiAl layer might be accounted for through substitution for Al in TiAl, as TiAl (tetragonal, P4/mmm) and α -TiAu (tetragonal, P4/nmm) have almost the same crystal structures.

It appears that on going from 600 to 700°C, the TiAl₃ and Au₂(Ti,Al) layers have reacted with most of the remaining Ti to form TiAl and Au₂Ti.



According to the above results, TiAl and Au₂Ti are the final products for the optimal contact. The net reactions between all four layers of metals can be simplified into two reactions:



and

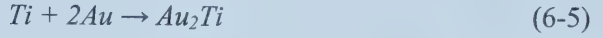


Table 6.14 Results of mass balance calculation

	Phase	Atomic weight	ρ (g/cm ³)	Thickness (nm)
Original	Au	196.9665	19.3	55
	Ti	47.90	4.5	150
	Al	26.98154	2.7	80
After annealing	Ti	47.90	4.5	36
	TiAl	74.88154	3.9	154
	Au ₂ Ti	441.833	14.6	81

Table 6.14 lists the results of mass balance calculations based on reactions 6-4 and 6-5. The mass balance calculations indicate that the above reactions would consume all the Au and Al, and ~114 nm (out of 150 nm) of the original deposited Ti. These calculations are only approximate as it was assumed that the TiAl and Au₂Ti are pure phases, which is clearly not the case. The calculations indicate that 154 nm of TiAl and 81 nm Au₂Ti were formed after annealing at 700°C for 30s; these are close to the measured thicknesses from the TEM images (130±10 nm of TiAl and 90±10 nm of Au₂Ti).

A thin layer (~10 nm thick) was also present at the metallization/AlGaN interface. Fig. 6.25 shows an EDX spectrum obtained from the interface region in the Fig. 6.22(a). EDX analysis was inconclusive because of the spatial resolution limitations of the microscope utilized. However, Ti, Al, Au, Ga and N were detected. Much of the Al, Ga and N detected may well have been from the underlying AlGaN, but the Au and Ti peaks were not artifacts. Other researchers have reported that Ti reacts with AlGaN to form TiN, α -AlN, β -AlN or AlTi₂N^{8,11}, which then leads to N depletion in AlGaN. Nitrogen vacancies can act as triple donors in the AlGaN layer, providing a tunneling route for ohmic

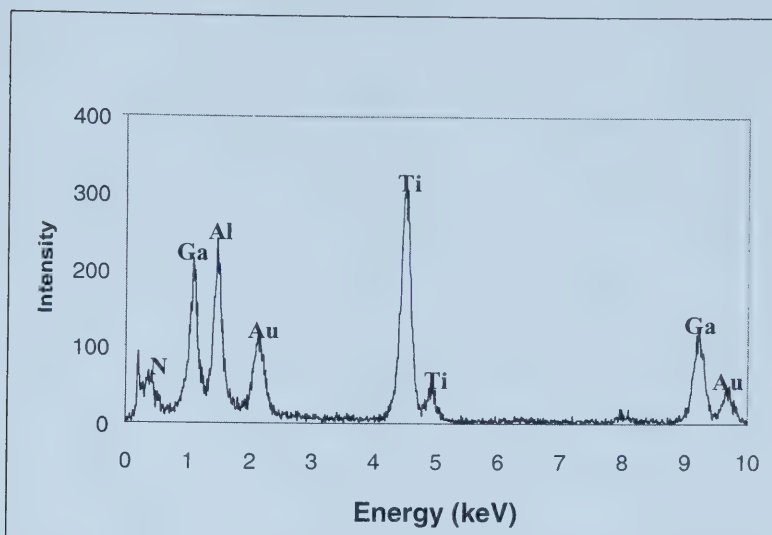


Figure 6.25 EDX spectrum obtained from the contact/AlGaIn interface in Fig. 6.22(a).

behavior. Although the EDX analysis was inconclusive, it is quite possible that TiN or AlTi_2N formed at the metallization/AlGaIn interface. The electron affinity of $\text{Al}_x\text{Ga}_{1-x}\text{N}$ decreases from 4.2 eV (χ_{GaN}) to 2.05 eV (χ_{AlN}) as x increases from 0 to 1, and the constraint for forming an ohmic contact to n-type AlGaIn, $\phi_m \leq \chi_{\text{Al}_x\text{Ga}_{1-x}\text{N}}$, thus demands the contact phase to have an increasingly lower electronic work function as the Al content increases. Apparently, Ti with a work function of 4.33 eV does not satisfy the requirement for forming ohmic contact to $\text{Al}_{0.2}\text{Ga}_{0.8}\text{N}$ (the electron affinity is 3.77 eV).

In contrast to contacts annealed at 600°C for 30s (Fig. 6.17), gold peaks were present in the interfacial region for contacts annealed at 700°C for 30s. In their study of a Au/Ni/Al/Ti metallization scheme to AlGaIn/GaN, Bright *et al.* also reported the presence of Au in the near-interface region but also reported that Au did not penetrate significantly into the AlGaIn. As the Au seems not to be part of an interfacial phase or not to penetrate significantly into the AlGaIn, they speculated that any beneficial effect would most likely be due to the presence of the Au-containing phase (which may have low Schottky barrier height) in contact with the interface, or to Au doping of the AlGaIn layer.

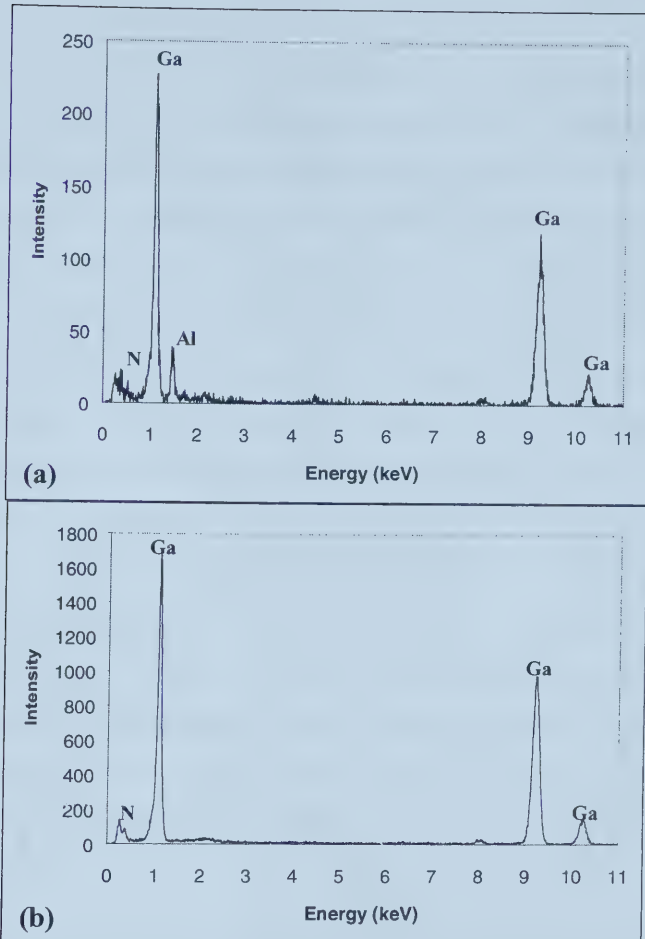


Figure 6.26 EDX spectra obtained from the AlGaIn layer (a) and GaN layer (b) in Fig. 6.22(a).

Fig. 6.26 shows EDX spectra obtained from the AlGaIn layer and GaN layer in Fig. 6.22(a). Because of the thin nature of AlGaIn layer (12 nm, originally) and the spatial resolution limitation of the TEM utilized, the EDX analysis was inconclusive. The AlGaIn spectrum may include x-rays emitted from the GaN layer. However, the spectrum does not include Ti and Au peaks; this eliminates the possibility of the interference from the contact layers. And in both Fig. 6.18(b) and Fig. 6.22(a), the boundary between the thin interfacial layer and the AlGaIn is clearly visible. The above spectrum shows that there is at least some AlGaIn remaining, i.e., AlGaIn had not been completely consumed after annealing at 700°C.

To summarize the above results, after annealing at 700°C for 30s, significant reactions between contact metals as well as between the contact metals and the semiconductor have occurred. The reactions between the contact metals produced two intermetallic phases, Au₂Ti and TiAl, with TiAl closer to the semiconductor. Several authors have reported the effect of varying the Al/Ti ratio in contacts to GaN^[67, 68] or AlGaIn/GaN^[69]. Several products, such as TiAl₃, Ti₃Al and TiAl, have been reported to form based on the Al/Ti ratio. An Al/Ti atomic ratio <3 is claimed to be preferable both morphologically as well as electrically. However, it is clear from the present experiments that the presence of other elements (such as Au, Ni and Ag) which react with the Al and /or Ti may have an effect on this ratio. The optimum Al/Ti ratio is thus likely to be affected by the other elements present. For the Al/Ti-based metallization scheme, it is important that all of Al is consumed after annealing, either reacted with Ti or other elements. Otherwise, hillocks will form on the surface of contacts. Hillocks result from differential thermal expansion and are common in Al metallizations because of the large thermal expansion coefficient of Al. Moreover, according to Al-Au-Ti ternary phase diagram (Fig. 6.24), pure gold would not be stable on top of the Ti/Al bilayer. There is no tie line between Au and any Ti/Al binary phase.

Table 6.15 Lattice parameters for possible interfacial phases

Phase	Symmetry	<i>d</i> spacing (nm)	<i>d</i> spacing (nm)	<i>d</i> spacing (nm)
TiN	Cubic Fm3m	0.245 (1 1 1)	0.212 (2 0 0)	0.150 (2 2 0) 0.128 (3 1 1)
β-AlN	Cubic Fm3m	0.238 (1 1 1)	0.206 (2 0 0)	0.146 (2 2 0) 0.124 (3 1 1)
AlTi ₃ N	Cubic Pm3m	0.237 (1 1 1)	0.205 (2 0 0)	0.410 (1 0 0)
TiAl	Tetragonal P4/mmm	0.231 (1 1 1)	0.204 (0 0 2) 0.199 (2 0 0)	0.407 (0 0 1)
AlTi ₂ N	Hexagonal P6 ₃ /mmc	0.259 (1 0 -1 0)	0.680 (0 0 0 2)	0.149 (1 1 -2 0)
α-AlN	Hexagonal P6 ₃ mc	0.268 (1 0 -1 0)	0.250 (0 0 0 2)	0.155 (1 1 -2 0)
α-GaN	Hexagonal P6 ₃ mc	0.276 (1 0 -1 0)	0.259 (0 0 0 2)	0.160 (1 1 -2 0)

There is considerable evidence that a nitrogen containing interfacial phase is crucial for the formation of ohmic contact. Nitrogen vacancies in the semiconductor layer, which result from the reaction between contact metals and semiconductor, will provide a tunneling route for ohmic behavior. Various interfacial phases, such as AlN, TiN, and AlTi₂N, have been reported. Due to the ultra thin nature of interface layer, high resolution electron microscopy (HREM) analysis is necessary. Also as TiN, AlTi₃N, β -AlN, Al and AlTi are all cubic with similar lattice parameters (Table 6.15), phase identification is difficult even when using HREM.

6.2.6 900°C annealing

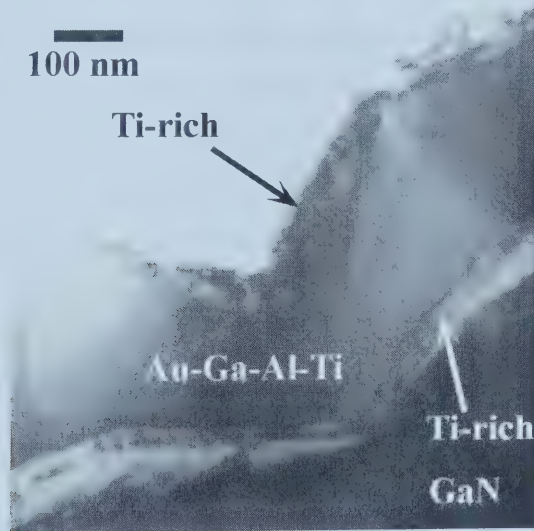


Figure 6.27 TEM bright field image of a sample annealed at 900°C for 30s.

Annealing at 900°C resulted in significant interdiffusion, most notably involving Au and Ga, along with a drastic increase in the contact resistance. Fig. 6.26 shows a TEM bright field image of a sample annealed at 900°C for 30s. Although the contact retained a 3-layer structure as with samples annealed at 700°C, the contact morphology changed. Two thin layers (around 30 nm) sandwiched one thick layer (around 200 nm).

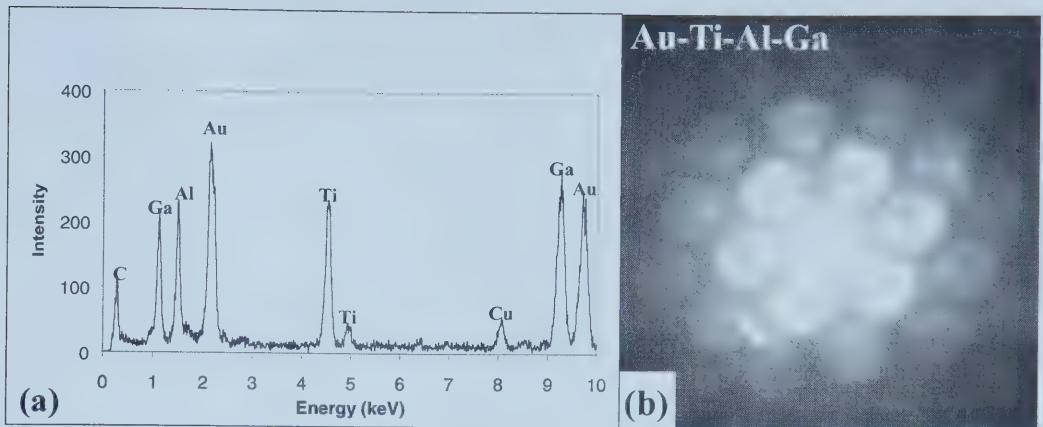


Figure 6.28 EDX spectrum (a) and CBED pattern (b) obtained from the middle layer in Fig. 6.26.

Fig. 6.27 shows an EDX spectrum and CBED pattern obtained from the thick middle layer. All three elements involved in the metallization, Au, Ti, and Al, as well as Ga from the semiconductor, are present in the spectrum. Diffraction patterns obtained from this layer could not be indexed to any known binary, ternary or even quaternary phases; however, the patterns resembled those expected from an fcc structure. Assuming an fcc structure, a lattice parameter of $a = 0.409$ nm was determined.

Fig. 6.28 includes the EDX spectra obtained from the outermost and innermost layers. The regions on either side of the quaternary layer were Ti-rich, but also contained the other system elements.

It is apparent that the binary phases present at 700°C (TiAl and Au_2Ti) have decomposed, as has the AlGaIn layer, forming three quaternary layers consisting of Au, Ti, Al and Ga. The innermost layer just adjacent to the GaN layer is no longer continuous; it has been replaced by intermittent patches. Other researchers have reported the presence of a thin surface oxide layer at similar annealing temperatures^[8, 11]. This was not the case here. Bright^[8] *et al.* did not find a change in AlGaIn layer after annealing at 900°C . They suggested the contact resistance in Ti/Al/Ni/Au contacts increases because of an increase

in metallization sheet resistance due to the formation of the surface oxide layer. However, in our case, the decomposition of Au_2Ti , TiAl and AlGaN appears to correlate with an increase in contact resistance.

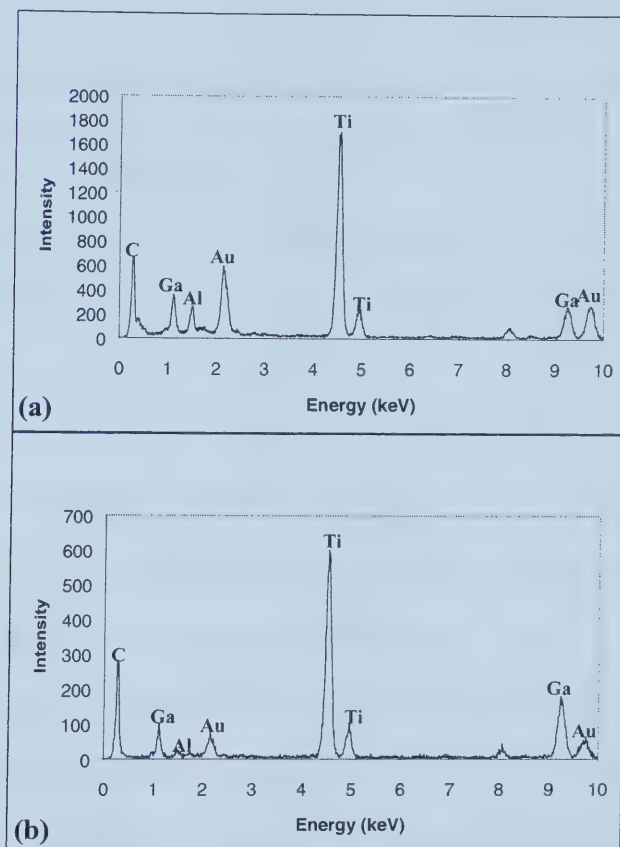


Figure 6.29 EDX spectra obtained from the outermost (a) and innermost layers.

7. CONCLUSIONS AND RECOMMENDATIONS FOR FUTURE WORK

7.1 Conclusions

Au/Ti/Al/Ti ohmic contacts to AlGaIn/GaN heterostructures have been investigated using TEM. The microstructural changes that occur during annealing, as well as the changes in the contact resistance are summarized below:

- After metal deposition, the specific contact resistance of the contact was quite high. The semiconductor surface was quite rough. The thickness of AlGaIn measured from the TEM images was close to the intended 12 nm. The four deposited metal layers, Ti, Al, Ti and Au, followed the morphology of the AlGaIn/GaN heterostructure. The thicknesses of metal layers were close to the target deposited values, of 30 nm, 80 nm, 120 nm, and 55 nm, respectively. There was no evidence of reaction between the metal layers, nor between the metal and semiconductor layers.
- Virtually no reaction occurred prior to annealing at 500°C; the metallization retained its 4-layer structure. Annealing at 400°C caused grain size growth within the metal layers. The relatively sharp interfaces indicated that no significant interdiffusion had occurred at the metallization/semiconductor interfacial region. However, some interdiffusion occurred at the interfaces between different metal layers, especially for the two Ti/Al interfaces.
- At 500°C, Al and portions of the Ti layer reacted to produce the first intermetallic phase, TiAl_3 . About 100 nm of the second Ti layer and portions of the first Ti layer remained unreacted. The outermost Au layer had not reacted with other metal layers

at this point and maintained its composition and morphology. The following reaction occurred at both Ti/Al interfaces: $Ti + 3Al = TiAl_3$.

- At about 600°C, Au started to react with both Ti and Al. With Al atoms substituting for Ti atoms in the Au_2Ti phase, a pseudobinary phase $Au_2(Ti_xAl_{1-x})$ formed. Visual inspection of the contact surface showed a color change from gold to gray. Full consumption of Au had not been occurred; isolated patches were still visible on the top surface. Additional $TiAl_3$ formed leaving patches of unreacted Ti at the metallization/semiconductor interface. The reactions at 600°C could be summarized as: $(1+x) Ti + (4-x) Al + 2 Au \rightarrow TiAl_3 + Au_2(Ti_xAl_{1-x})$.
- Annealing at 700°C resulted in the lowest specific contact resistance. $TiAl_3$ transformed to $TiAl$, and loss of Al in pseudobinary $Au_2(Ti_xAl_{1-x})$ left a binary phase Au_2Ti . Semi-quantitative EDX analysis indicated that about 30 nm of Ti would be left after formation of $TiAl$ and Au_2Ti phases. With respect to the minimum specific contact resistance, a thin Ti-rich layer (~10 nm) was present at the metallization/AlGaN interface. This thin Ti-rich interfacial layer was believed to be TiN or $AlTi_2N$ and deemed to be important to ohmic behavior. The second thicker Ti layer, which was utilized as the diffusion barrier layer, did not block Au inward diffusion towards the semiconductor effectively. Au diffused into the interfacial region and may have had beneficial effects for ohmic contact formation. The reactions are summarized as: $2(1-x) Ti + TiAl_3 + Au_2(Ti_xAl_{1-x}) \rightarrow (4-x) TiAl + Au_2Ti$.
- Annealing at higher temperatures led to significant interdiffusion and the formation of a quaternary Au-Al-Ti-Ga layer sandwiched between 2 Ti-rich regions. Microstructural analysis showed that two binary phases, $TiAl$ and Au_2Ti , as well as

AlGa_N semiconductor layer, decomposed, which resulted in the drastic increase in the contact resistance.

7.2 Recommendations for Future work

At the completion of this work, the author would like to propose some recommendations for future work in order to further understand and optimize ohmic contacts to AlGa_N/Ga_N heterostructures.

1. It is necessary to investigate the contacts using a high resolution electron microscope (HREM). Generally, the thickness of the metallization/AlGa_N interface is under 10 nm; it is difficult to analyze such fine features with conventional TEM. However, this interfacial region plays a crucial role in ohmic contact formation. Therefore, all the speculations of TiN or AlTi₂N formation need to be verified with HREM.
2. To optimize the metallization scheme to AlGa_N/Ga_N heterostructures, it is necessary to simplify the complexity of reactions, which occur during annealing. The work achieved by Luther's group^[48] has inspired future improvements in ohmic contacts to Ga_N-based semiconductors. A new metallization scheme is proposed to achieve ohmic behavior. This scheme has three layers. The results from other groups' work show that a nitrogen depleted interfacial layer is crucial in ohmic contact formation; and titanium is the appropriate candidate to react with AlGa_N or Ga_N semiconductor. Therefore, 20-40 nm Ti is deposited on the AlGa_N surface initially. Secondly, a 20-100 nm TiN layer is deposited on the top of the first Ti layer as a diffusion barrier between Ti and the outermost Au layer. TiN has very a low electronic work function of 2.92 eV^[53] and can satisfy the Schottky-Mott requirement to form ohmic contact on AlGa_N/Ga_N semiconductor. Finally, a 10-50 nm Au layer is deposited in order to decrease the sheet resistance of the contact. After metal deposition, the system needs to be annealed at 500-700°C for 30s in order to activate the reaction between Ti and AlGa_N. Further laboratory work is necessary to prove the feasibility of this design, as well as to find the optimal thickness of each metal layer and annealing parameters.

8. REFERENCES

- [1] T.L. Tansley and C.P. Foley, *Journal of Applied Physics*, **59**, 3241 (1986).
- [2] W.M. Yim, E.J. Stofko, P.J. Zanzucchi, J.I. Pankove, M. Ettenburg, and S.L. Gilbert, *Journal of Applied Physics*, **44**, 292 (1973).
- [3] M.A. Khan, J.N. Kuznia, A.R. Bhattarai and D.T. Olson, *Applied Physics Letter*, **62**, 1786 (1993).
- [4] X.H. Yang, T.J. Schmidt, W. Shan and J.J. Song, *Applied Physics Letters*, **66**, 1 (1995).
- [5] M.A. Khan, A.R. Bhattarai, J.N. Kuznia and D.T. Olson, *Applied Physics Letter*, **63**, 1214 (1993).
- [6] M.A. Khan, J.N. Kuznia, D.T. Olson, J.M. Van Hove, M. Blasingame and L.F. Reitz, *Applied Physics Letter*, **63**, 1 (1993)
- [7] S. Nakamura, T. Mukai and M. Senoh, *Applied Physics Letters*, **64**, 28 (1994).
- [8] A.N. Bright, P.J. Thomas, M. Weyland, D.M. Tricker, C.J. Humphreys, and R. Davies, *Applied Physics Letters*, **89**, 3143 (2001).
- [9] D. Qiao, Z.F. Guan, J. Carlton, S.S. Lau, and G.J. Sullivan, *Applied Physics Letters*, **74** (9), 2652 (1999).
- [10] D. Qiao, L.S. Yu, S.S. Lau, G. J. Sullivan, S. Ruvimov, and Z. Liliental-Weber, *MRS Internet Journal of Nitride Semiconductor Research*, **4S1**, G1.5 (1999).

- [11] S. Ruvimov, Z. Liliental-Weber, J. Washburn, D. Qiao, S.S. Lau, and P.K. Chu, *Applied Physics Letters*, **73**, 2582 (1998).
- [12] D. Qiao, L. Jia, L.S. Yu, P.M. Asbeck, S.S. Lau, S.H. Lim, Z. Liliental-Weber, T.E. Haynes, and J.B. Barner, *Journal of Applied Physics*, **89** (10), 5543 (2001).
- [13] K.K. Chu, M.J. Murphy, J. Burm, W.J. Schaff, and L.F. Eastman, *IEEE Proceedings, IEEE/Cornell Conference on Advanced Concepts in High Speed Semiconductor Devices and Circuits*, 399 (1997).
- [14] W.D. Callister, Jr, *Materials Science and Engineering an Introduction*, 5th edition, John Wiley & Sons, Inc., (2000)
- [15] J.W. Mayer and S.S. Lau, *Electronic Materials Science: For Integrated Circuits in Si and GaAs*, Macmillan, (1990).
- [16] V.W.L. Chin, T.L. Tansley, and T. Osotchen, *Journal of Applied Physics*, **75**, 7365 (1994).
- [17] H. Morkoç, *Nitride Semiconductors and Devices*, Springer, (1999).
- [18] H.P. Maruska and J.J. Tietjen, *Applied Physics Letters*, **15**, 327 (1969).
- [19] S.N. Mohammad and H. Morkoç, *Progress in Quantum Electronics*, **20**, 361 (1996).
- [20] M.S. Shur and M.A. Khan, *Materials Research Bulletin*, **22** (2), 44 (1997).
- [21] U.V. Bhapkar and M.S. Shur, *Journal of Applied Physics*, **82** (4), 1649 (1997).
- [22] S.K. O'Leary, B.E. Foutz, M.S. Shur, U.V. Bhapkar, and L.F. Eastman, *Solid State Communications*, **105**, 621 (1998).

- [23] S.K. O'Leary, B.E. Foutz, M.S. Shur, U.V. Bhapkar, and L.F. Eastman, *Journal of Applied Physics*, **83**, 826 (1998).
- [24] W.R.L. Lambrecht, B. Segall, *Band Structure of the Group-III Nitrides, in Gallium Nitride*, ed. By J.I. Pankove, T.D. Moustakas, Semiconductors and Semimetals, **50**, 369 (Academic, San Diego, CA 1998).
- [25] G.J. Sullivan, M.Y. Chen, J.A. Higgins, J.W. Yang, Q. Chen, R.L. Pierson, and B.T. McDermott, *IEEE Electron Device Letters*, **19**, 198 (1998).
- [26] R. Li, S.J. Cai, L. Wong, Y. Chen, K.L. Wang, R.P. Smith, S.C. Martin, K.S. Boutros, and J. M. Redwing, *IEEE Electron Device Letters*, **20**, 323 (1999).
- [27] I. Daumiller, C. Kirchner, M. Kamp, K.J. Ebeling, and E. Kohn, *IEEE Electron Device Letters*, **20**, 448 (1999).
- [28] S.T. Sheppard, K. Doverspike, W.L. Pribble, S.T. Allen, J.W. Palmour, L.T. Kehias, and T.J. Jenkins, *IEEE Electron Device Letters*, **20**, 161 (1999).
- [29] C.H. Chen, S. Keller, G. Parish, R. Vetury, P. Kozodoy, E.L. Hu, S.P. Denbaars, U.K. Mishra, and Y. Wu, *Applied Physics Letters*, **73**, 3147 (1998).
- [30] E.H. Rhoderick and R.H. Williams, *Metal-Semiconductor Contacts*, 2nd Edition, Oxford Science Publications, (1988).
- [31] S.M. Sze, *Physics of Semiconductor Devices*, Wiley, New York, (1981).
- [32] F.A. Padovani and R. Stratton, *Solid-State Electron*, **9**, 695 (1966).
- [33] D.G. Ivey, *Platinum Metals Review*, **43**, (1), 2 (1999).

- [34] C.W. Wilmsen, *Physics and Chemistry of III-V Compound Semiconductor Interfaces*, Plenum Press, New York and London, (1985).
- [35] H.K. Henisch, *Semiconductor Contacts*, Clarendon, Oxford, (1984).
- [36] J.S. Foresi and T.D. Moustakas, *Applied Physics Letters*, **83** (22), 2859 (1993)
- [37] M.E. Lin, Z. Ma, F.Y. Huang, Z.F. Zhan, L.H. Allen, and H. Morkoc, *Applied Physics Letters*, **64** (8), 1003 (1994).
- [38] Z.F. Fan, S. N. Mohammad, W. Kim, O. Aktas, A.E. Botchkarev, and H. Morkoc, *Applied Physics Letters*, **68** (12), 1672 (1996).
- [39] J. Burm, K. Chu, W.A. Davis, W.J. Schaff, L.F. Eastman, and T.J. Eustis, *Applied Physics Letters*, **70** (4), 464 (1997).
- [40] B.P. Luther, J.M. DeLucca, S.E. Mohnney, and R.F. Karliceck, Jr., *Applied Physics Letters*, **71** (26), 3859 (1997).
- [41] B.P. Luther, S.E. Mohnney, T.N. Jackson, M.A. Khan, Q. Chen, and J.W. Yang, *Applied Physics Letters*, **70** (1), 57 (1997).
- [42] J.D. Guo, C.I. Lin, M.S. Feng, F.M. Pan, G.C. Chi, and C.T. Lee, *Applied Physics Letters*, **68** (2), 235 (1996).
- [43] B.P. Luther, S.E. Mohnney, J.M. DeLucca, and R.F. Karliceck, Jr., *Journal of Electronic Materials*, **27** (4), 196 (1998).
- [44] A.T. Ping, M.A. Khan, and I. Adesida, *Journal of Electronic Materials*, **25** (5), 819 (1996).

- [45] D.B. Ingerly, Y.A. Chang, N.R. Perkins, and T.F. Kuech, *Applied Physics Letters*, **70** (1), 108 (1997).
- [46] M.W. Cole, D.W. Eckart, W.Y. Han, R.L. Pfeffer, T. Monahan, F. Ren, C. Yuan, R.A. Stall, S.J. Pearton, Y. Li, and Y. Lu, *Journal of Applied Physics*, **80** (1), 278 (1996).
- [47] L.L. Smith, R.F. Davis, R.J. Liu, M.J. Kim, and R.W. Carpenter, *Journal of Materials Research*, **14** (3), 1032 (1999).
- [48] B.P. Luther, S.E. Mohney, and T.N. Jackson, *Semiconductor Science and Technology*, **13**, 1322 (1998).
- [49] D.F. Wang, S.W. Feng, C. Lu, A. Motayed, M. Jah, S.N. Mohammad, K.A. Jones, and L. Salamanca-Riba, *Journal of Applied Physics*, **89** (11), 6214 (2001)
- [50] H.J. Lee, S.J. Yu, H. Asahi, S. Gonda, Y.H. Kim, J.K. Rhee, and S.J. Noh, *Journal of Electronic Materials*, **27** (7), 829 (1998).
- [51] Z.M. Zhao, R.L. Jiang, P. Chen, D.J. Xi, H.Q. Yu, B. Shen, R. Zhang, Y. Shi, S.L. Gu, and Y.D. Zheng, *Applied Physics Letters*, **79** (2), 218 (2001).
- [52] S. Kurtin, T.C. McGill, and C.A. Mead, *Physics Review Letters*, **22**, 1433 (1969).
- [53] K.O. Schweitz and S.E. Moheny, *Journal of Electronic Materials*, **30** (3), 175 (2001).
- [54] D. Mistele, J. Aderhold, H. Klausling, T. Rotter, O. Semchinova, J. Stemmer, D. Uffmann, J. Graul, F. Eberhard, M. Mayer, M. Schauler, M. Kamp, and C. Ahrens, *Semiconductor Science and Technology*, **14**, 637 (1999).

- [55] S. Ruvimov, Z. Liliental-Weber, J. Washburn, K.J. Duxstad, E.E. Haller, Z.F. Fan, S.N. Mohammad, W. Kim, A.E. Botchkarev, and H. Morkoc, *Applied Physics Letters*, **69** (11), 1556 (1996).
- [56] Q. Z. Liu, L. S. Yu, F. Deng, S. S. Lau, Q. Chen, J. W. Yang, and M. A. Khan, *Applied Physics Letters*, **71** (12), 1658 (1997).
- [57] T G G Maffei, M C Simmonds, S A Clark, F Peiro, P Haines, and P J Parbrook, *Journal of Physics D: Applied physics*, **33**, L115 (2000).
- [58] C.T. Lee, M.Y. Yeh, C.D. Tsai, and Y.T. Lyu, *Journal of Electronic Materials*, **26** (3), 262 (1997).
- [59] C.H. Chen, S. Keller, G. Parish, R. Vetury, P. Kozodoy, E.L. Hu, S.P. Denbaars, U.K. Mishra, and Y. Wu, *Applied Physics Letters*, **73** (21), 3147 (1998).
- [60] D.B. Ingerly, Y. Chen, R.S. William, T. Takeuchi, and Y.A. Chang, *Applied Physics Letters*, **77** (3), 382 (2000).
- [61] H. Tang, J.B. Webb, J.A. Bardwell, and T. MacElwee, *Journal of Vacuum Science and Technology A*, **18** (2), 652 (2000).
- [62] J. Chen and D. Ivey, *Micron*, in press.
- [63] D.B. Williams and C.B. Carter, *Transmission Electron Microscopy*, Plenum, (1996).
- [64] J.J. Hren, J.I. Goldstein, and D.C. Joy, *Introduction to Analytical Electron Microscopy*, Plenum Press, New York, (1979).
- [65] H. Baker, H. Okamoto, *ASM Handbook, Volume 3 Alloy Phase Diagrams*, ASM International, (1992).

- [66] G. Petzow and G. Effenbuerg, *Ternary Alloys, A Comprehensive Compendium*, Volume 3, VHC, New York, (1998).
- [67] J.S. Kwak, S.E. Mohny, J.-Y. Lin, and R.S. Kern, *Semiconductor Science and Technology*, **15**, 756 (2000).
- [68] S.M. Gasser, E. Kolawa, and M.A. Nicolet, *Journal of Electronic Materials*, **28**, 949 (1999).
- [69] V. Tilak, R. Dimitrov, M. Murphy, B. Green, J. Smart, W.J. Schaff, J.R. Schealy, and L.F. Eastman, *Materials Research Society Symposium Proceedings*, **622**, T7.4.1 (2000).
- [70] Rieck van Loo, *Acta Metallurgica*, 21 61 (1973).

University of Alberta Library



0 1620 1538 7135

B45615